

**Nanomaterials, Devices and Interface Circuits: Applications for Optoelectronic and  
Energy Harvesting**

BY

MOHSEN PURAHMAD

B.S., K.N Toosi University of Technology, Tehran, Iran, 2006

M.S., K.N Toosi University of Technology, Tehran, Iran, 2009

THESIS

Submitted as partial fulfillment of the requirements  
for the degree of Doctor of Philosophy in Electrical and Computer Engineering  
in the Graduate College of the  
University of Illinois at Chicago, 2013

Chicago, Illinois

Defense Committee:

Mitra Dutta, Chair and Advisor  
Siddhartha Ghosh  
Michael A. Stroscio  
Zheng Yang  
George Crabtree, Physics

**This thesis is dedicated to my parents, my brother and my wife.**

## **ACKNOWLEDGEMENTS**

First and foremost I would like to acknowledge my advisor, Prof. Mitra Dutta, vice chancellor for research at University of Illinois at Chicago, who is my academic mother, for her valuable guidance, great support, and consistent encouragement I received during the research work. She patiently provided the vision, encouraging and constructive feedback necessary for me to proceed through the doctoral program and complete my dissertation. I am also grateful for the excellent example she has provided as a researcher, mentor, instructor, and role model. It was a great opportunity for me to do my doctoral program under her supervision and to learn from her research expertise.

Dr. Michael Strosio is one of the most brilliant scientists that I have ever met. I would like to thank Dr. Michael Strosio for his amazing classes in quantum physics and for being such a great mentor during this whole process. He took his time and patience to help me understand the materials. I feel so happy and blessed for the opportunity to take classes with you. Thank you for all the learning experiences and invaluable guidance you gave me during my PhD program at UIC. I also would like to express appreciation to you for all the helpful feedback, and guidance you gave me as one of my thesis committee members.

## **ACKNOWLEDGEMENTS (continued)**

I would like to thank my other thesis committee members, Dr. George Crabtree, Dr. Zheng Yang, and Dr. Siddhartha Ghosh, for all of their guidance through this process; your discussion, suggestions, and feedback have been absolutely invaluable and I could not complete my work without your friendly assistance. It is no easy task, reviewing a thesis in detail, and I appreciate each of you for taking your time to go over my thesis.

I would like to express my deep gratitude to Prof. Heinz Busta, with whom I have collaborated so much. I have had the pleasure and honor to discuss research ideas with him and he provided helpful insights and I have learned a lot from his expertise in the design and fabrication of some novel micro-electro-mechanical structures (MEMS) devices.

I benefited from the guidance of senior PhD students, who have played an important role in the completion of this dissertation. In particular I would like to acknowledge Dr. Banani Sen, who helped me at a very beginning stage of the research and I gained a lot from her, through her suggestions at various points of my PhD program.

I would also like to thank, Dr. Ayan Kar, my colleague and my friend, who played an incredibly valuable role in my research program. I would like to send well deserved thank you to my former lab mate, Dr. Vahid Ghafarinia. More than anything, he is an amazing friend with boundless generosity. Thank you for your support, patience, invaluable guidance.

## **ACKNOWLEDGEMENTS (continued)**

I would also like to thank Dr. Kebin Low at the Research Resource Center at UIC for training me to use the TEM data analysis and sharing his precious knowledge on XPS system. My time at UIC was enriched by the amazing friends and groups that became part of my life. I would like to thank my supportive friends, who I have met over the years, for giving advice, sharing ideas and enjoying life. Special thanks go to Rade Kuljic for providing support and friendship that I needed.

Finally, I would like to thank my family for unconditional love and care. Their love provided my motivation and if not for my parents, I would not complete this road. My family has always supported and encouraged me to seek challenges. In particular, I am grateful to my brother, who was always encouraging me to follow the opportunities. Despite the distance, our relationship has grown stronger and much deeper. My special appreciation and thanks go to my lovely wife, Mojgan, who unwaveringly supported and shared with me all the difficult times throughout this academic journey with great love and sacrifices.

**MP**

## TABLE OF CONTENTS

<u>CHAPTER</u>	<u>PAGE</u>
1. INTRODUCTION.....	1
1.1 Introduction to semiconductor nanowires .....	1
1.2 Background on nanostructure ZnO material .....	2
1.3 Optoelectronic applications of ZnO nanowires.....	5
1.4 Piezoelectric materials and piezoelectric energy harvesting .....	6
2. PHOTOLUMINESCENCE CHARACTERIZATION OF ZNO NANOWIRES DECORATED WITH SPUTTERED METALLIC NANOPARTICLES .....	8
2.1 Growth of ZnO nanowires.....	9
2.2 Experimental details .....	10
2.3 Results and discussion .....	16
3. INFLUENCE OF SUBSTRATE ON THE FLUORENSCENCE ON THE EMISSION OF ZINC OXIDE NANOWIRES AND CORE-SHELL CADMIUM SELENIDE/ZINC SULFIDE QUANTUM DOTS.....	28
3.1 Experimental .....	28
3.2 Results and discussion.....	29
3.2.1 Heterojunction effects.....	32
3.2.2 Scattering effects.....	34
4. MODELING THE EFFECT OF PIEZOELECTRIC CHARGES ON THE SURFACE DEPLETION REGION AND SURFACE POTENTIAL OF ZINC OXIDE NANOWIRES.....	38
4.1 Relevant properties of piezoelectricity .....	39
4.2 Mechanical analysis .....	41
4.3 Depletion region in a 1D structure .....	45
4.4 Results and discussion.....	49
5. INVESTIGATION OF EFFECT OF APPLIED STRESS FREQUENCY ON THE ELECTRICAL RESPONSE OF PVDF-TrFE NANO-FIBERS.....	55
5.1 Piezoelectricity in PVDF polymers .....	55
5.2 Experimental .....	57
5.3 Effect of vibration frequency on generated pulse width .....	59
5.4 Estimation of maximum output power .....	61
5.5 Mechanical creep and relaxation of PVDF .....	62

## TABLE OF CONTENTS (continued)

6. LOW POWER INTERFACE CIRCUITS FOR PIEZOELECTRIC MICRO-SCALE ENERGY HARVESTING SYSTEMS .....	65
6.1 Introduction to low power interface circuits for energy harvesting applications .....	65
6.2 Block component diagram of a micro-scale piezoelectric energy harvesting system .....	66
6.2.1 Piezoelectric energy harvester .....	67
6.2.2 Power converter .....	69
6.2.3 Control unit .....	78
6.3 Power transfer loss model .....	82
6.4 Optimal power transistor size .....	83
6.5 Component value considerations .....	84
7. CONCLUSIONS AND FUTURE WORK .....	86
CITED LITERATURE .....	91
VITA .....	99

## LIST OF TABLES

<u>TABLE</u>	<u>PAGE</u>
I. BAND GAP AND ELECTRON AFFINITIES OF DIFFERENT MATERIAL .....	35
II. CONSTANTS USED IN THE NUMERICAL ANALYSIS.....	50



## LIST OF FIGURES

<u>FIGURE</u>	<u>PAGE</u>
1. The wurtzite structure model of ZnO.....	4
2. Schematic diagram of piezo-potential in Wurtzite structure.....	4
3. SEM image of the as grown ZnO NWs (a) under an inappropriate growth condition and (b) under an appropriate growth condition.....	12
4. SEM image of the as grown ZnO NWs from different views (a) side view (b) top view and (C) with a tilt angle 30 degree. ....	13
5. (a) SEM image of the as grown ZnO NWs, (b) XPS spectra of the as grown ZnO NWs (red), Ni coated ZnO NWs (blue) and Al coated ZnO NWs (black). (c) TEM images of the as grown ZnO NW and (d) the Al coated ZnO NW.....	14
6. The schematic diagram of RF magnetron system.....	15
7. The schematic diagram of experimental PL setup. ....	15
8. (a) Room temperature PL spectra of as grown ZnO NWs (red) and the PL spectra of ZnO NWs coated with Al nanoparticles for 120 seconds (black), (b) Room temperature PL spectra of as grown ZnO NWs (red) and the PL spectra of ZnO NWs coated with Ni nanoparticles for 120 seconds (black). ....	17
9. (a) Room temperature PL spectra of as grown ZnO NWs and Al sputtered (90 seconds) ZnO NWs (b) PL spectra of as grown ZnO NWs and Al sputtered NWs at 8.5 K (c) Temperature dependent Photoluminescence spectra (near UV region) of as grown ZnO NWs (d) Al sputtered ZnO NWs and the insets show the peak energy versus temperature (e) integrated intensity of the neutral donor-bound exciton of ZnO nanowires as a function of temperature with theoretical fitting curve. ....	21
10. The room temperature PL spectra of as grown ZnO NWs (red) and ZnO NWs coated with Al nanoparticles by e-beam evaporation (black) under different evaporation times (a) 60 seconds and (b) 120 seconds.....	23
11. (a) Schematic diagram of the band bending of ZnO NWs and (b) the corresponding phenomenological model of the trapping pathways.....	24

## LIST OF FIGURES (Continued)

<u>FIGURE</u>	<u>PAGE</u>
12. Photoluminescence spectra of CdSe/ZnS quantum dots on different substrates. ....	29
13. Photoluminescence spectra of ZnO nanowires on different substrates.....	30
14. Photoluminescence spectra of CdSe/ZS on different substrates under exposure of different incident light power intensity. ....	30
15. (a) Energy band diagram of ZnO-GaAs heterojunction, (b) Energy band diagram of ZnO-Si heterojunction where $\phi_{s1}$ and $\chi_{s1}$ be the work function and electron affinity of substrates and $\phi_{s2}$ and $\chi_{s2}$ be the work function and electron affinity of ZnO, respectively, (c) Energy band diagram of ZnO-ITO contact, where $\chi_s$ is the electron affinity of ZnO; $\phi_s$ be the work function of ZnO and $\phi_m$ -work function of ITO ,(d) Energy band diagram of ZnO-glass heterojunction, where $\phi_s$ and $\chi_s$ be the work function and electron affinity of ZnO respectively, (e) Energy band diagram of CdSe/ZnS-GaAs heterojunction (ZnS is too narrow and has not been put in the heterojunction because of the very small effect), (f) Energy band diagram of CdSe/ZnS-Si heterojunction, (g) Energy band diagram of CdSe/ZnS -ITO contact, (h) Energy band diagram of CdSe/ZnS -glass heterojunction. ....	32
16. The schematic diagram of structure used in simulation and the incident plane wave where the red arrow represents the electric field component and the blue arrow represents the magnetic field component. ....	34
17. The Poynting vector of scattered filed versus the X position. ....	35
18. The schematic representation of the nanowire (a) and its band bending (b). ....	46
19. The surface depletion width of ZnO NWs with different radii. ....	50
20. The surface depletion width of ZnO NWs with different radii in the presence of piezoelectric charges. ....	51
21. The potential electric distribution in a ZnO NW with radius 80 nm in presence of different piezoelectric charge densities. ....	52
22. The surface potential of a ZnO NWs with different radii as a function of piezoelectric charges. ....	52

## LIST OF FIGURES (Continued)

<u>FIGURE</u>	<u>PAGE</u>
23. The surface depletion region of ZnO NWs with different radius and the surface potential of ZnO NWs with two different radii (60 nm and 100 nm) at presence of different piezoelectric charge densities. ....	53
24. Schematic of the electrospinning setup and poling process.....	58
25. The optical image of the as-electrospun nanofibers.....	58
26. The schematic diagram of the energy harvester based on PVDF nanofibers .....	59
27. (a) A typical electrical response of PVDF nanofibers and electrical response of PVDF nanofibers at different vibration frequencies, (b) at frequency = 2.6Hz, (c) at frequency = 3.7Hz and (d) at frequency = 6.5Hz.....	60
28. Fast Fourier Transform (FFT) for one cycle output voltage and the insert picture is corresponding sin waves of odd frequency. ....	61
29. The mechanical relaxation function of PVDF in the directions of $n = 1$ (a) and $n = 2$ (b) .....	63
30. The block diagram of a micro-scale energy harvesting system. ....	67
31. The schematic diagram of a cantilever based piezoelectric energy harvester and its equivalent circuit [82]. ....	69
32. The schematic diagram of conventional SC voltage converter.....	71
33. Power dissipation in PEH. ....	72
34. The block diagram of the proposed interface circuit. ....	74
35. The prototype diagram of proposed interface circuit and control and timing signals generated by control block and the theoretical currents of proposed interface circuits. ....	75
36. The switch states in positive and negative half-period (a) in the proposed circuit topology and (b) in the Piezoelectric Energy Harvester-Charger IC proposed in Ref [80] and the equivalent circuits in charging and discharging modes of proposed circuit topology. ....	77

## LIST OF FIGURES (Continued)

<u>FIGURE</u>	<u>PAGE</u>
37. The transistor level schematic of the designed continuous time comparator circuit operating in sub-threshold region ( $v_{dd} = 1$ and $v_{ss} = -1$ ) and the designed time delay circuit. ....	80
38. The schematic diagram of an active rectifier. ....	82
39. Power loss of a power transistor versus the power transistor size. ....	84

## LIST OF ABBREVIATIONS

ZnO	Zinc Oxide
NWs	Nanowires
ZB	Zinc Blende
WZ	Wurtzite
NBE	Near-Band-Edge
PL	Photoluminescence
NPs	Nano-Particles
GaAs	Gallium Arsenide
ITO	Indium Tin Oxide
PVDF	Polyvinylidene Fluoride
VLS	Vapor–Liquid–Solid
CVD	Chemical Vapor Deposition
MOCVD	Metalorganic Chemical Vapor Deposition
CBE	Chemical Beam Epitaxy
MBE	Molecular Beam Epitaxy
1D	One-Dimensional
UV	Ultraviolet
GaN	Gallium Nitride
LEDs	Light-Emitting Diodes
PDs	Photo Detectors
FP	Fabry–Perot

## **LIST OF ABBREVIATIONS (Continued)**

VLSE	Vapor–Liquid– Solid Epitaxy
SEM	Scanning Electron Microscope
XPS	X-ray Photoelectron Spectroscopy
Al	Aluminum
Ni	Nickel
RF	Radio Frequency
TEM	Transmission Electron Microscope
FX	Free Exciton
SX	Surface Excitonic
DX	Donar Excitonic
CdSe	Cadmium Selenide
ZnS	Zinc Sulfide
QDs	Quantum Dots
MEMS	Micro-Electro-Mechanical Structure
PZT	Lead Zirconate Titanate
NFES	Near-Field Electrospinning
DMF	N-dimethylformamide
FFT	Fast Fourier Transform
PEH	Piezoelectric Energy Harvesters

## **LIST OF ABBREVIATIONS (Continued)**

SC	Switched Capacitor
CCR	CMOS-Controlled Rectifiers

## SUMMARY

Metal oxide semiconductor nanowires (NWs) have received a lot of research attention because of their unique and wide-ranged optical, electronic, and piezoelectric properties. Among the metal oxide semiconductor NWs zinc oxide (ZnO) NWs have been the focus of much research due to their unique optical, electrical and piezoelectric properties. ZnO is a compound semiconductor with a wide direct band gap (3.37 eV) and a large exciton binding energy (60 meV) which makes this material a promising candidate for optoelectronic applications such as short-wavelength semiconductor lasers and light-emitting diodes. ZnO NWs have additional functionality arising from their size which allows for further flexibility in band gap engineering.

In addition to the novel optical properties of ZnO NWs, utilization of ZnO NWs as nano-scale energy harvester devices has made them a very exciting topic of research. ZnO can possess two crystal structures, cubic zinc blende (ZB) and hexagonal wurtzite (WZ) in which each atom is tetrahedrally coordinated by atoms of the opposite species. In the crystal structure of ZnO,  $\text{Zn}^{2+}$  cations and  $\text{O}^{2-}$  anions are tetrahedrally coordinated in crystal structure of ZnO, and the centers of the positive and negative ions overlap. Therefore, if a stress is applied at an apex of the tetrahedron, the centers of the cations and anions are relatively displaced, resulting in a dipole moment and consequently, polarization from all of the units result in a macroscopic potential drop along the straining direction in the crystal.



## **SUMMARY (continued)**

Due to the large surface-to-volume ratio of semiconductor NWs the surface effects such as geometric properties, surface states, surface roughness, and surface passivation can strongly modify the optical and electrical properties of nano-structure materials such as ZnO NWs. Hence, understanding the surface effects, on the transport behavior of ZnO nanostructures is crucial for reliable device fabrication.

In the first part of this dissertation, the effect of surface passivation on the near-band-edge emission (NBE) of as grown ZnO nanowires has been studied. It was shown that decorating the ZnO nanowires with sputtered metallic nano-particles can strongly enhance the NBE of as grown ZnO nanowires. Since the ZnO NWs have a weak NBE, numerous studies have been done to enhance the NBE and photoluminescence (PL) efficiency of ZnO NWs. Different methods such as polymer coating of ZnO NWs and hydrogen plasma treatment are seen to boost the NBE and photoluminescence efficiency of ZnO NWs. Recently, among the different passivation methods the effect of metallic nanoparticles (NPs) on PL properties of ZnO NWs have been the focus of much research. In most studies an enhancement of NBE was observed and the results were interpreted in terms of surface plasmons, unintentional hydrogen incorporation and the nature of the contact formed between the metal and ZnO NWs. Our study demonstrates that decorating the ZnO NWs with metal NPs in the presence of high energy Ar atoms cleans the surface of ZnO NWs from near surface traps and surface adsorbed species, thus it leads to a strong enhancement of NBE emission and a relative reduction of visible peak.

## SUMMARY (continued)

Furthermore, we have investigated the effect on the intensity of PL spectra of deposited nanostructure materials such as ZnO NWs when deposited on different substrates (gallium arsenide, silicon, glass and indium tin oxide-coated glass). The experimental results show that the PL intensity is the highest for the gallium arsenide (GaAs) and the least from the indium tin oxide-coated glass (ITO-coated glass) substrate for both the quantum dots and the ZnO NWs. These experimental results were simulated by taking into account the scattered field from different substrates and were seen to be in agreement to the experimental results. We found that the PL intensity is a function of scattered light from the surface of substrate rather than the type of heterojunction formed between the deposited material and substrate.

As discussed in addition to novel optoelectronic applications of ZnO nanowires, utilization of ZnO nanowires as nano-scale piezoelectric energy harvesters have made them a hot topic of research. In the second part of this thesis, the piezoelectric properties of ZnO nanowires have been the focus of the study. Since demonstration of the first nano-scale energy harvester device based on one single ZnO NWs a comprehensive model which can explain the generation of strain induced piezoelectric field in the presence of free carriers has not been proposed. The piezoelectric constitutive equations, which are used to calculate the strain induced piezoelectric potential, can be applied in a medium with zero or negligible free carriers.

## SUMMARY (continued)

Therefore, in case of piezoelectric metal oxide semiconductor materials such as ZnO NWs with a free carrier density about  $10^{18} \text{ cm}^{-3}$  the constitutive equations cannot be applied directly. Here, we have developed a model which strongly conciliates some strongly divergent opinions behind operation of the semiconductor piezoelectric nano-generators. In order to develop such a physics-based model, first the electrostatic potential and depletion width in piezoelectric semiconductor NWs are derived by considering a non-depleted region and a surface depleted region and solving the Poisson equation. By determining the piezoelectric induced charge density, in terms of equivalent density of charges, the effect of piezoelectric charges on the surface depletion region and the distributed electric potential in NW have been investigated. The numerical results demonstrate that the ZnO NWs with smaller radii have a larger surface depletion region which results in a stronger surface potential and depletion region perturbation by induced piezoelectric charges.

Furthermore, we have also studied another type of piezoelectric materials which have a negligible free carrier concentration and constitutive equations can be applied directly. In this domain, we have investigated the effect of applied stress on the generated electrical pulse of Polyvinylidene fluoride (PVDF). PVDF is a piezoelectric polymer that has been the focus of much research in many piezoelectric applications due to its high piezoelectric coefficient.

## **SUMMARY (continued)**

The electromechanical properties of PVDF can be defined by the constitutive equations. In this study, the effect of applied stress frequency on the electrical response of PVDF-TrFE has been investigated. The experimental results demonstrate that increasing the frequency of applied stress results in increasing of pulse width of the electrical response. A model based on the mechanical creep and relaxation of PVDF has been proposed, which agrees well with the observed experimental results.

In the last part of our study on piezoelectric energy harvesters the low power interface circuits which are one of the fundamental building blocks of any self-powered devices has been studied. Utilization of piezoelectric energy harvesters to power electronic devices has attracted significant attention recently. However, the power generated by a piezoelectric energy harvester is too small to power an electronic device directly. Hence, a low power, efficient interface circuit between the energy harvester and a storage unit is essential in any piezoelectric energy harvesting system. Here, a new interface circuit topology for piezoelectric energy harvesting applications is proposed and various design factors for circuit-level optimization are discussed. In the proposed interface circuit a peak detector circuit operating in the sub-threshold region with power dissipation around 160 nW together with a delay circuit form the control block, which is one of the more important units of the piezoelectric energy harvesting systems.

# 1. INTRODUCTION

## 1.1 Introduction to semiconductor nanowires

Ongoing device scaling is the most important factor for economic survival of the current integrated circuit industry. However, further decreases in device dimensions are now starting to reach the regime that classical physics becomes invalid and the function of the device cannot be guaranteed [1]. The above concerns necessitate development of new technological concepts and materials. From this point of view, a “bottom-up” approach is thought to be a potential alternative. The bottom-up approach is a common technique to synthesize the nanowire structures. In this technique using a metal catalyst has enabled the routine fabrication of sophisticated one-dimensional devices that is otherwise not possible with conventional top-down approaches. This growth method is most frequently described through the vapor–liquid–solid (VLS) mechanism which is introduced by Wagner and Ellis with silicon whiskers growth. Other techniques used for nanowire growth including chemical vapor deposition (CVD), laser ablation, supercritical fluid solution phase, metallorganic chemical vapor deposition (MOCVD), chemical beam epitaxy (CBE) and molecular beam epitaxy (MBE) [2]. However, among the different growth techniques the VLS mechanism has proven to be extremely flexible and allows for the controlled growth of complex nanostructures. For instance, heterojunctions can be formed axially along the nanowire simply by changing the material precursors present in the reaction environment [2].

As a result of the rapid progress of modern microelectronics, semiconductor NWs and their related heterostructures are intensively being investigated due to their unique

growth mechanisms and novel properties. Semiconductor NWs have a broad application range including diodes, field effect transistors, optoelectronic devices, sensors, thermoelectrical devices, photocatalysis, and piezoelectronics. NW structures exhibit unique and superior properties compared to their bulk counterparts, properties in which their one-dimensional (1D) confined transport of electrons or photons, large surface to volume ratio, quantum confinement, and excellent mechanical properties play major roles [3]. Among the semiconductor nanowires the wide variety of electronic and chemical properties of metal oxide semiconductor nanowires makes them exciting materials for basic research and for technological applications alike. Oxides span a wide range of electrical properties from wide band-gap insulators to metallic and superconducting. One of the metal oxide semiconductor nanowires which has been the focus of much research is ZnO NWs. ZnO NWs provide enormous advantages such as high aspect ratio, good field electron emission property and excellent molecular absorption and desorption characteristics in catalyst applications.

## **1.2 Background on nanostructure ZnO material**

Since the 1960s, synthesis of ZnO thin films has been an active field due to their applications as sensors, transducers and catalysts. Nanostructured ZnO materials have attracted broad attention due to their remarkable performance in electronics, optics and photonics. ZnO is a key technological material with unique optical and piezoelectric properties. The lack of a center of symmetry in ZnO crystal structure, combined with large electromechanical coupling, results in strong piezoelectric and pyroelectric properties which makes ZnO a great candidate material to be used in mechanical actuators,

piezoelectric sensors and piezoelectric energy harvesters. Furthermore, ZnO is a wide direct band-gap (3.37 eV) compound semiconductor that makes it a suitable candidate for short wavelength optoelectronic applications. ZnO has a high exciton binding energy (60 meV) which can ensure efficient excitonic emission at room temperature and room temperature ultraviolet (UV) luminescence applications. ZnO is a versatile functional material that has a diverse group of growth morphologies including nanocombs, nanorings, nanosprings, nanobelts and nanowires. Crystal structure of ZnO can be cubic zinc blende (ZB) or hexagonal wurtzite (WZ) in which each atom is tetrahedrally coordinated by atoms of the opposite species. The stability of WZ as compared to ZB is closely related to the deviation of the lattice-parameter ratio from the ideal value. The structure of ZnO can be explained as a number of alternating planes composed of tetrahedrally coordinated  $O^{2-}$  and  $Zn^{2+}$  ions, stacked alternately along the c-axis as shown in figure 1. The non-centro-symmetric structure and consequently piezoelectricity and pyroelectricity result from the tetrahedral coordination in ZnO [4]. The schematic diagram of piezo-potential in wurtzite structure is shown in figure 2.

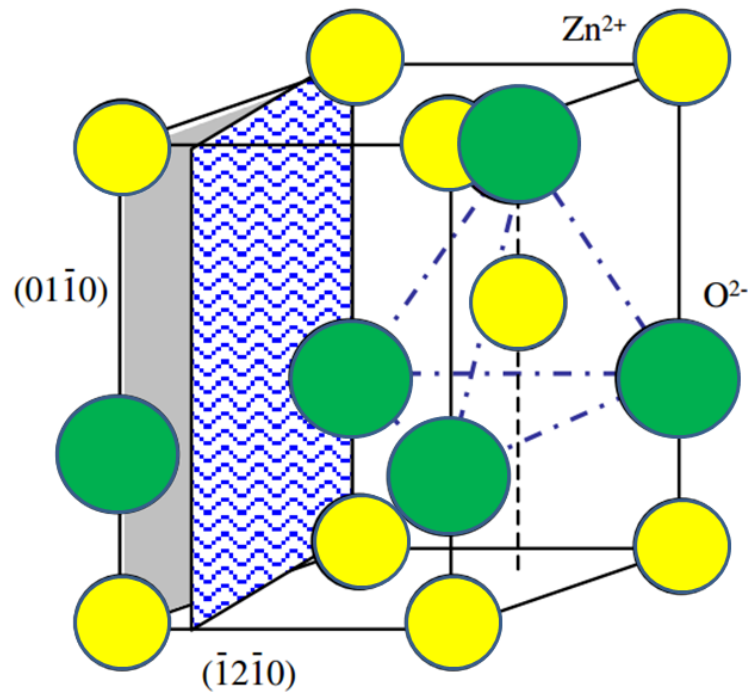


**Figure 1:** The wurtzite structure model of ZnO.

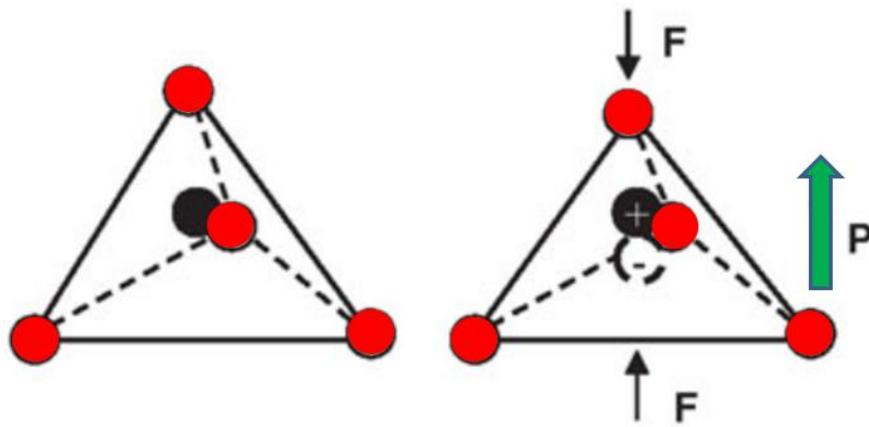


**Figure 2:** Schematic diagram of piezo-potential in Wurtzite structure.



### **1.3 Optoelectronic applications of ZnO Nanowires**

From many points of view, ZnO is considered to be an alternative material to GaN for device applications owing to its relatively low production cost and superior optical properties due to its high exciton binding energy (60 meV) [5]. ZnO is a multifunctional compound semiconductor material which has been the focus of much research for short-wavelength optoelectronic applications, such as light-emitting diodes (LEDs), laser diode, photodetectors (PDs) and ultraviolet lasers. ZnO NWs have additional functionality arising from their size which allow for further flexibility in band gap engineering. One of the most advanced optoelectronic devices based on ZnO NWs is the ultraviolet semiconductor laser which is widely used for applications in photonics, information storage, biology and medical therapeutics. Single-crystalline semiconductor NWs are considered as an excellent means by which to realize small and cost effective Fabry–Perot (FP) type lasers, because of the optical feedbacks provided by the naturally formed flat facets in the ends of NWs [6]. Although the performance of gallium nitride ultraviolet lasers has improved significantly over the past decade, demand for lower costs, higher powers and shorter wavelengths has motivated interest in ZnO, which has a wide direct band-gap and a large exciton binding energy. However, due to the large surface-to-volume of nanostructure materials such as NWs the optical and electrical properties of these material structures can be strongly modified by surface effects. Hence, understanding the surface effects such as geometric properties, surface states, surface roughness, and surface passivation, on the transport behavior of ZnO nanostructures is crucial for reliable device fabrication [7].

#### **1.4 Piezoelectric materials and piezoelectric energy harvesting**

As described in **Section 1.1** piezoelectric effect is the ability of certain materials which have no center of symmetry in their crystal structure to generate an electric charge in response to applied mechanical stress. The word Piezoelectric is derived from the Greek piezein, which means to squeeze or press, and piezo, which is Greek for "push" [8]. The piezoelectric effect is a reversible effect. It means that materials exhibiting the direct piezoelectric effect (the generation of electricity when stress is applied) also exhibit the converse piezoelectric effect (the generation of stress when an electric field is applied). Piezoelectric materials can be divided into two main groups, insulator piezoelectric materials such as Lead zirconium titanate (PZT) and Polyvinylidene fluoride (PVDF) as well as piezoelectric semiconductor materials such as ZnO and GaN.

Insulator piezoelectric materials have been long used in piezoelectric energy harvester and sensor devices. However, the large unit size, large triggering force and specific high resonance frequency of the traditional cantilever-based energy harvester limit their applicability and adaptability in nanoscale devices and systems. In this domain, one dimensional (1D) nanostructures have attracted much attention in the fabrication of nano-generators. Recently, it has been demonstrated that nano-generators (NGs) based on piezoelectric NWs have the potential to harvest mechanical energy. The first nano-scale energy harvester based on ZnO NWs was introduced by Wang *et al* [9]. Among the piezoelectric nanostructures such as lead zirconate titanate (PZT) NWs and PVDF nano-fibers, the piezoelectric semiconductor NWs such as ZnO NWs and GaN NWs have been the focus of considerable research. Because piezoelectric semiconductors can be used to

convert mechanical energy to electrical energy and also since they are semiconductors, they can be used as a junction device for performing diode and transistor-type functions. These properties make them strong candidates for use in electromechanically coupled sensors and transducers. However, due to the presence of free carriers in semiconductor piezoelectric materials the physics behind the semiconductor nanogenerators such as ZnO NWs is not well known. Hence, the application of piezoelectric semiconductor NWs requires a good understanding of their electrical and piezoelectric properties. As described in **Section 1.1**  $\text{Zn}^{2+}$  cations and  $\text{O}^{2-}$  anions are tetrahedrally coordinated in crystal structure of ZnO, and the centers of the positive and negative ions overlap. Therefore, if a stress is applied at an apex of the tetrahedron, the centers of the cations and anions are relatively displaced, resulting in a dipole moment as shown in figure 1. Consequently, polarization from all of the units results in a macroscopic potential drop along the straining direction in the crystal.

## **2. PHOTOLUMINESCENCE CHARACTERIZATION OF ZNO NANOWIRES DECORATED WITH SPUTTERED METALLIC NANOPARTICLES**

ZnO is a promising candidate for optoelectronic applications such as short-wavelength semiconductor lasers and light-emitting diodes [10-12]. ZnO NWs have additional functionality arising from their size which allow for further flexibility in band gap engineering. Since the ZnO NWs have a weak NBE, numerous studies have been done to enhance the NBE and PL efficiency of ZnO NWs. Different methods such as polymer coating of ZnO NWs [13, 14] and hydrogen plasma treatment [15] are seen to boost the NBE and photoluminescence efficiency of ZnO NWs. Recently, the effect of metallic nanoparticles (NPs) on the PL properties of ZnO NWs have been the focus of much research [12, 16]. In most studies an enhancement of NBE was observed and the results were interpreted in terms of surface plasmons [17], unintentional hydrogen incorporation [18], and the nature of the contact formed between the metal and ZnO NWs [16].

Here we investigate the effect of the presence of Ar plasma during the metallic NP deposition on the PL intensity of ZnO NWs. A strong enhancement of the NBE and a relative reduction of visible emission from the gap are seen for those ZnO NWs on which metallic NPs have been sputtered. By considering the nature of the contact formed between ZnO NWs and metallic NPs, the concentration of ambient hydrogen during metal sputtering, and comparison of the PL intensities from the NP sputtered ZnO NWs and those NWs with NPs deposited by e-beam evaporation, a model is proposed that satisfies the observed strong enhancement of NBE and related reduction of the visible peak.

## **2.1 Growth of ZnO nanowires**

The VLS nanowire growth mechanism is based on a process which starts with the dissolution of gaseous reactants in nano-sized liquid droplets of the catalyst metal and it is followed by nucleation and growth of single-crystalline wires or rods. It is reported that the size of the alloy droplet, which is dependent to the size of the starting metal seed, is determined the diameter of a NW and using mono-dispersed metal nano-clusters as catalyst results in synthesis of NWs with a narrow diameter distribution [19].

However it does not necessarily imply that the diameter of NWs is constant along its axis. It has been recently reported that the dynamic reshaping of the catalyst particles during the NW growth determines the length and shape of the NWs [20]. In order to achieve more vertically oriented nanowires the conventional epitaxial crystal growth techniques can be applied to this VLS process. For instance the techniques such as vapor–liquid–solid epitaxy (VLSE) is particularly powerful in the controlled synthesis of nanowire arrays. ZnO prefers to grow along the [001] direction and readily forms a highly oriented array when grown epitaxially on a sapphire (110) substrate [19].

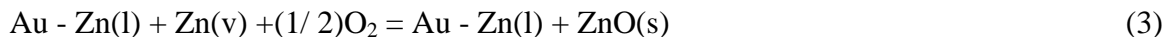
At the growth temperature, carbothermal reduction of the ZnO powder yields Zn vapor based on the following reactions:



Catalyst alloy formation:



The NW formation can be explained by the following reaction:



The oxidation process of the Zn which leads to the formation of ZnO and contributing to the NW growth is a critical step. In the present situation, it is likely that ZnO NWs originate from the oxidation of the Zn atoms within the Au-Zn alloy particle due to the increase of the activity of metals upon alloying [20].

## **2.2 Experimental details**

The ZnO nanowires were grown by the VLS in a horizontal quartz tube at atmospheric pressure on n-type, 100 plane silicon wafer as substrate. Prior to the growth substrates were cleaned by acetone and dried in a stream of nitrogen, then coated with a layer of 3 nm gold thin film using e-beam evaporation. Zinc oxide powder (99.99%, Aldrich Company) mixed with graphite (powder < 20  $\mu\text{m}$ , Aldrich Company) in a weight ratio of 1:1 was used to carry out the carbothermal reaction process. The coated substrates and ceramic boat with the ZnO and graphite powders were placed in the middle of a 2 inches quartz tube. The system was heated to 900-910°C with a constant flow (350 sccm) of Ar for 30-50 min and then cooled down to room temperature. The grown ZnO nanowires were characterized with a variable-pressure Hitachi S-3000N scanning electron microscope (SEM) and an x-ray photoelectron spectroscopy (XPS).

In figure 3 is shown the SEM images of as grown ZnO NWs under an inappropriate and an appropriate growth condition. Figure 4 shows the as grown ZnO NWs from different view angles. The grown ZnO NWs have an average length about 20  $\mu\text{m}$  and a diameter in range of 50 to 200 nm. Aluminum (Al) and nickel (Ni) metal nano-particles were deposited on the ZnO NWs by a radio-frequency (RF) magnetron system with the

corresponding metal target at room temperature. Before starting the plasma and metal deposition, the experimental chamber was pumped down to a high vacuum ( $\sim 10^{-6}$  Torr) and sputtering process was carried out under a constant flow of ultra-pure Ar (45 sccm) at a power of 100 watt. The XPS spectra of as grown ZnO nanowires and coated ZnO NWs measured by a Kratos AXIS-165 spectrometer are shown in figure 5(b). The transmission electron microscope (TEM) images of as grown ZnO NWs and coated ZnO NWs with Al nanoparticles are shown in figure 5(c) and figure 5(d). As seen in figure 5(d) the metallic NPs have an island-like morphology which consists of a network of sputtered metallic NPs on the surface of ZnO NW. The room temperature PL was excited by a 325 nm HeCd laser and the PL emission was collected by an Acton 2500i spectrometer. The low temperature PL measurement was performed in a closed cycle helium cryostat at 8.5 K. The schematic diagram of RF magnetron system and used for decorating the ZnO NWs is shown in figure 6. Figure 7 is also showing the schematic diagram of the experimental PL setup used for PL measurements.

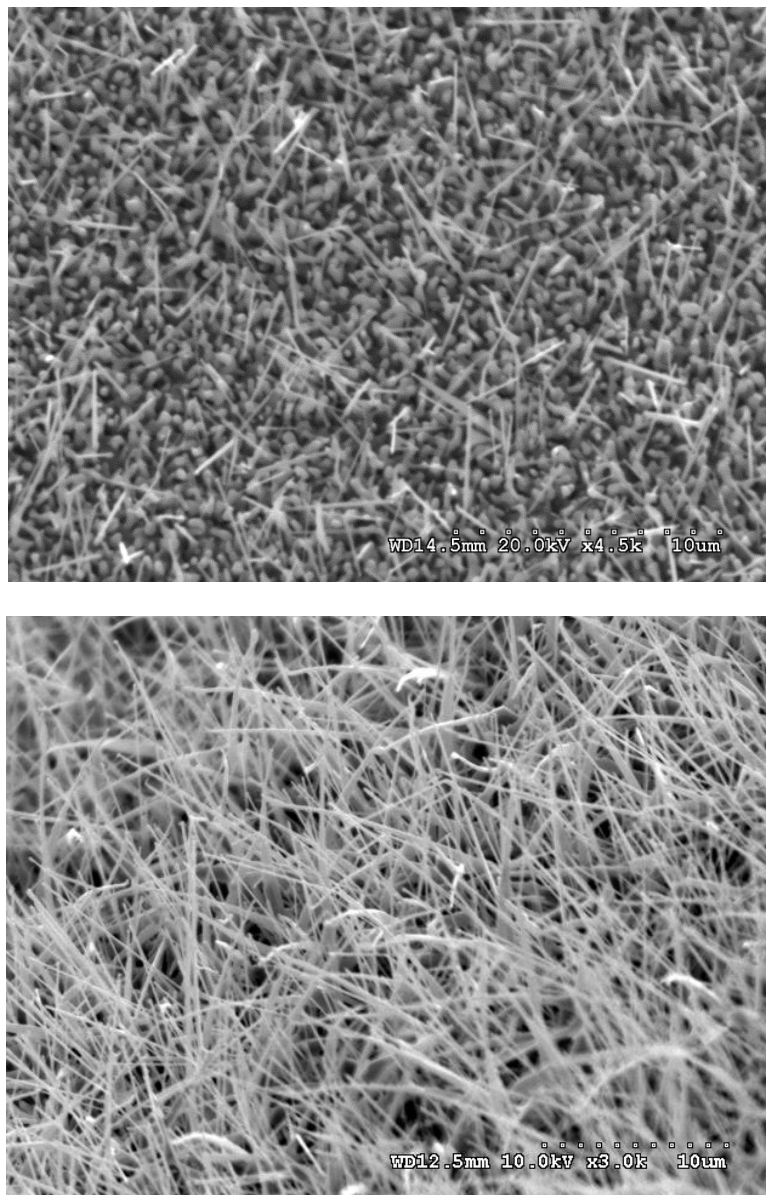


**Figure 3:** SEM image of the as grown ZnO NWs (a) under an inappropriate growth condition and (b) under an appropriate growth condition



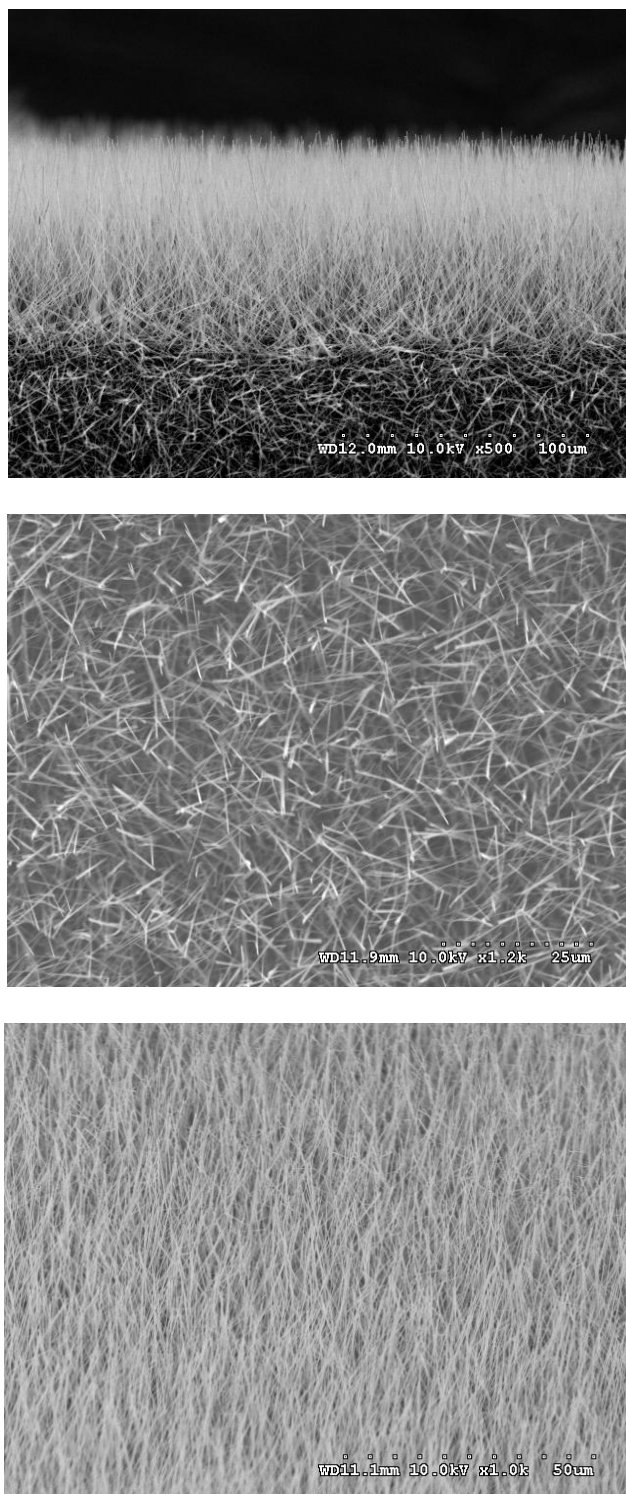


**Figure 4:** SEM image of the as grown ZnO NWs from different views (a) side view (b) top view and (C) with a tilt angle 30 degree.

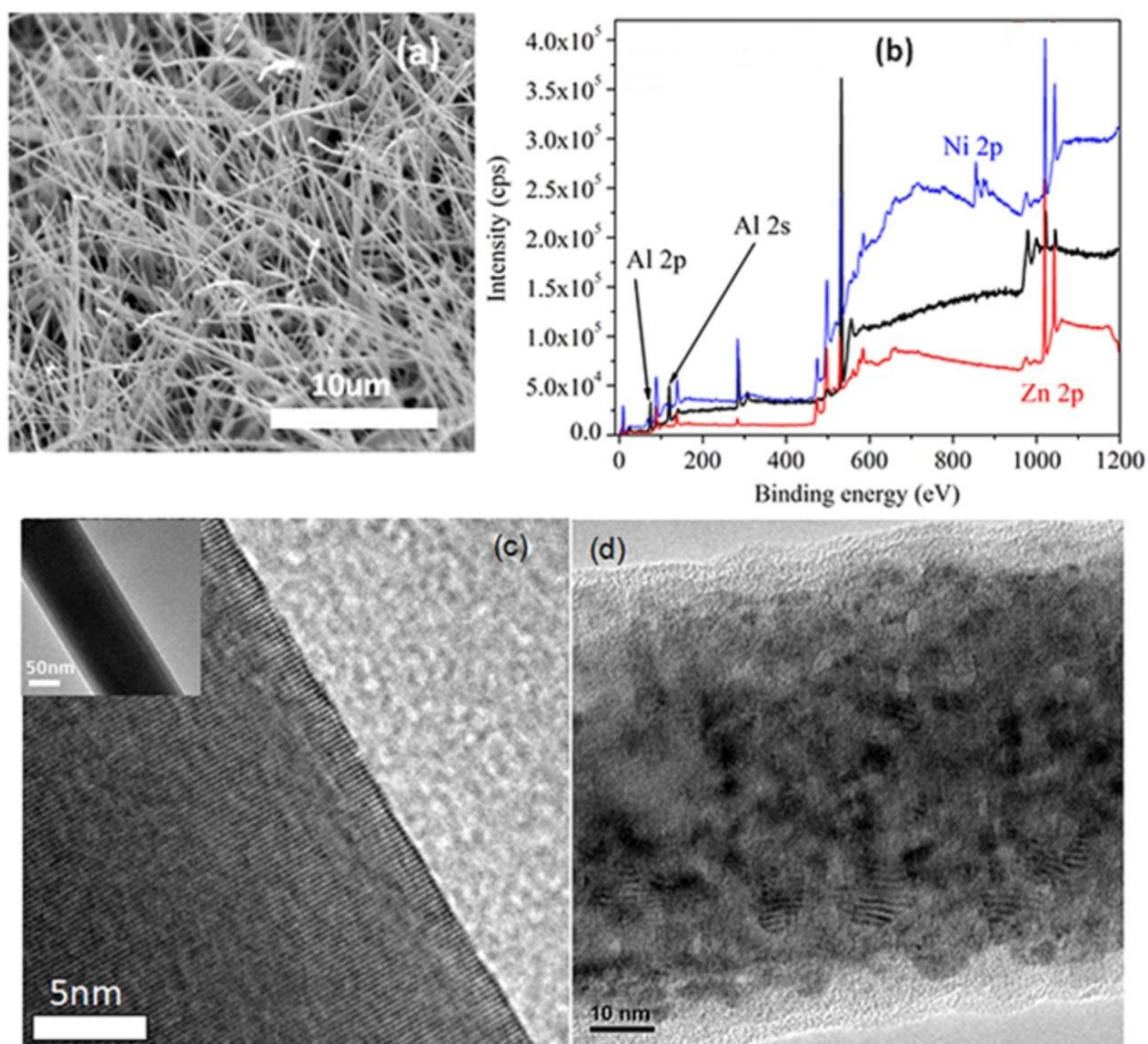


**Figure 5:** (a) SEM image of the as grown ZnO NWs, (b) XPS spectra of the as grown ZnO NWs (red), Ni coated ZnO NWs (blue) and Al coated ZnO NWs (black), (c) TEM images of the as grown ZnO NW and (d) the Al coated ZnO NW.

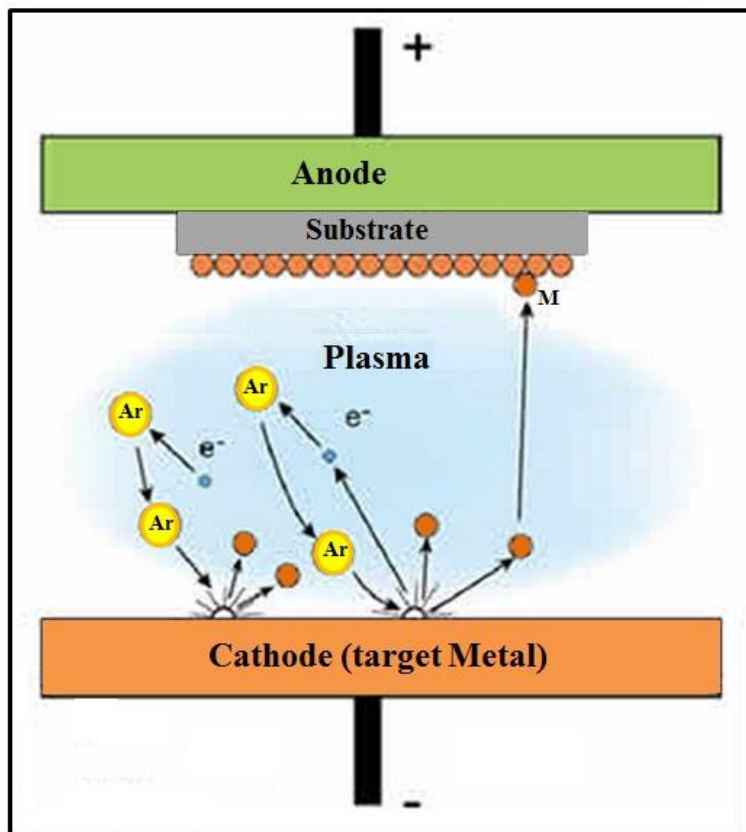


**Figure 6:** The schematic diagram of RF magnetron system.

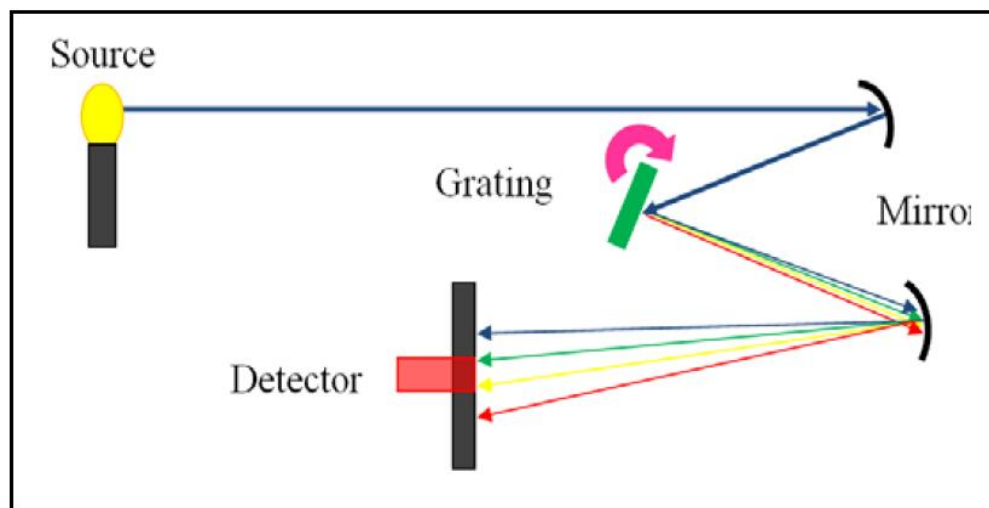


**Figure 7:** The schematic diagram of experimental PL setup.

### **2.3 Results and discussion**

The room-temperature PL spectra of the as grown ZnO NWs and those coated with RF magnetron sputtered *Al* and *Ni* nanoparticles are compared in figure 8(a) and 8(b). A strong enhancement of NBE is seen for both ZnO NWs decorated with *Al* and *Ni* nanoparticles. Since the junction between ZnO NW and *Al* is an ohmic contact and the the junction between the *Ni* and ZnO NW is a Schottky contact [16], the experimental results shown in figure 8(a) and 8(b) demonstrate that this strong enhancement of NBE is not mainly due to the nature of the contact formed between the metallic NPs and ZnO NWs. However, the type of contact formed between the ZnO and metallic NPs may have a small effect as a higher enhancement ratio of NBE is seen in case of ZnO NWs decorated with *Al* nano-particles. In addition to the increase in intensity of the NBE peak we also see the related reduction of the visible peak as shown in figure 8(a) and figure 8(b).

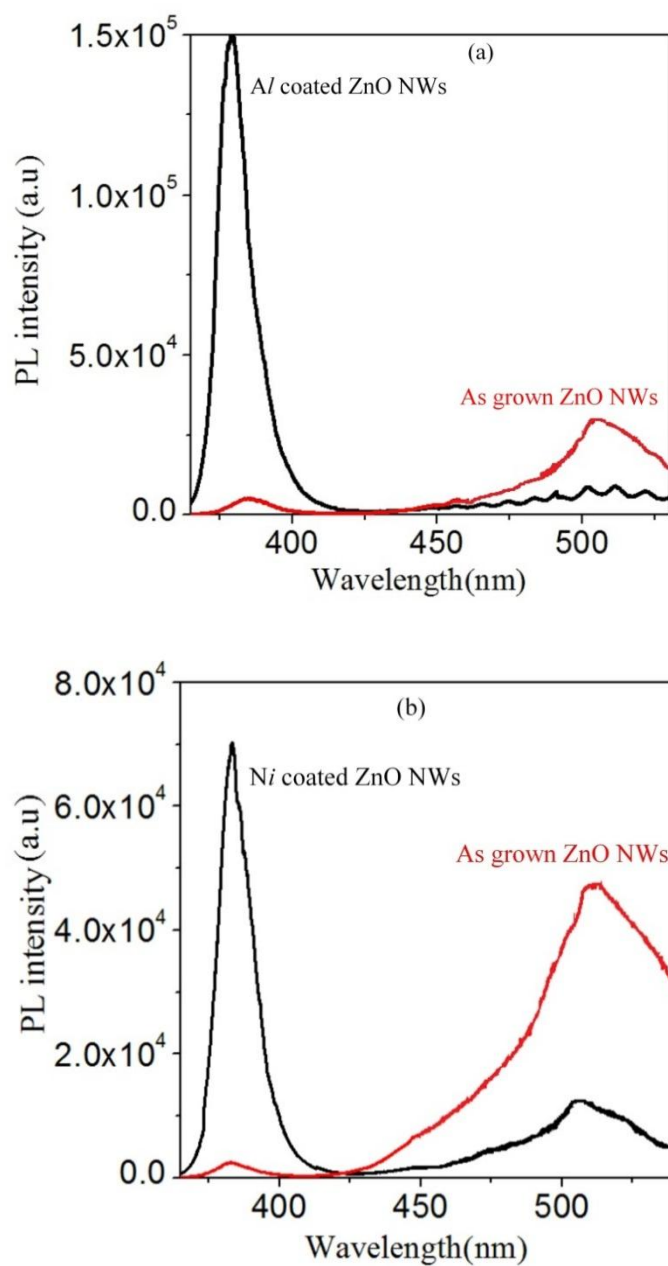


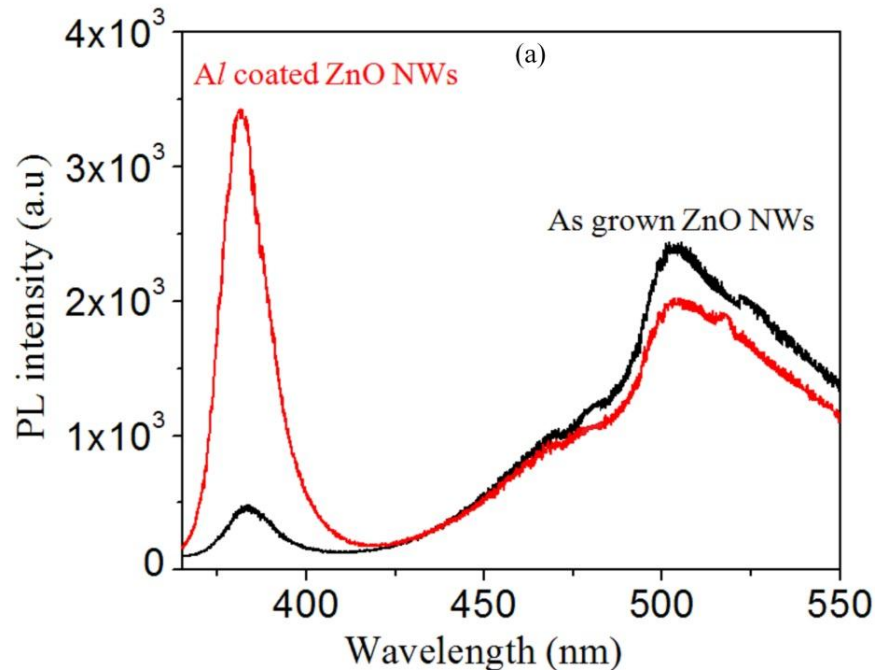
**Figure 8:** (a) Room temperature PL spectra of as grown ZnO NWs (red) and the PL spectra of ZnO NWs coated with Al nanoparticles for 120 seconds (black), (b) Room temperature PL spectra of as grown ZnO NWs (red) and the PL spectra of ZnO NWs coated with Ni nanoparticles for 120 seconds (black).

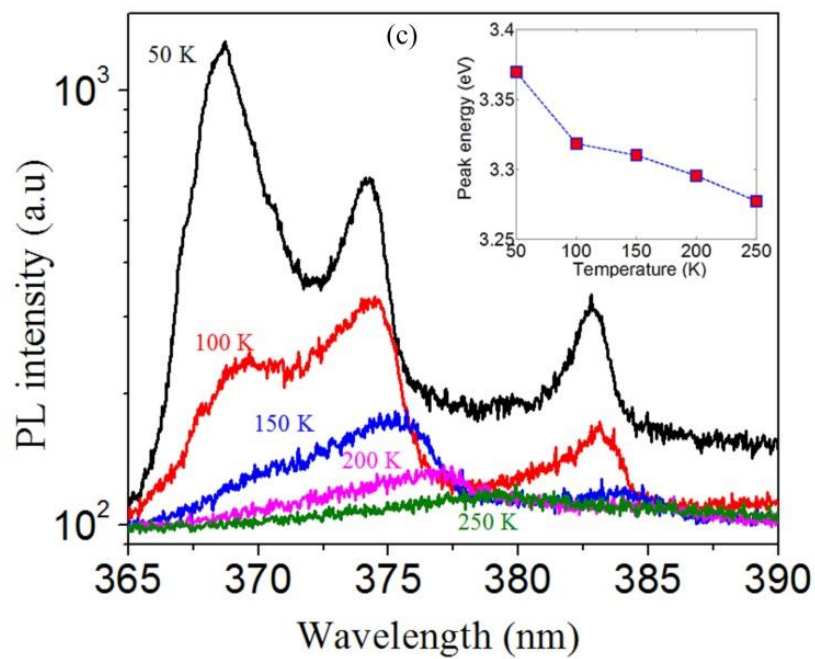
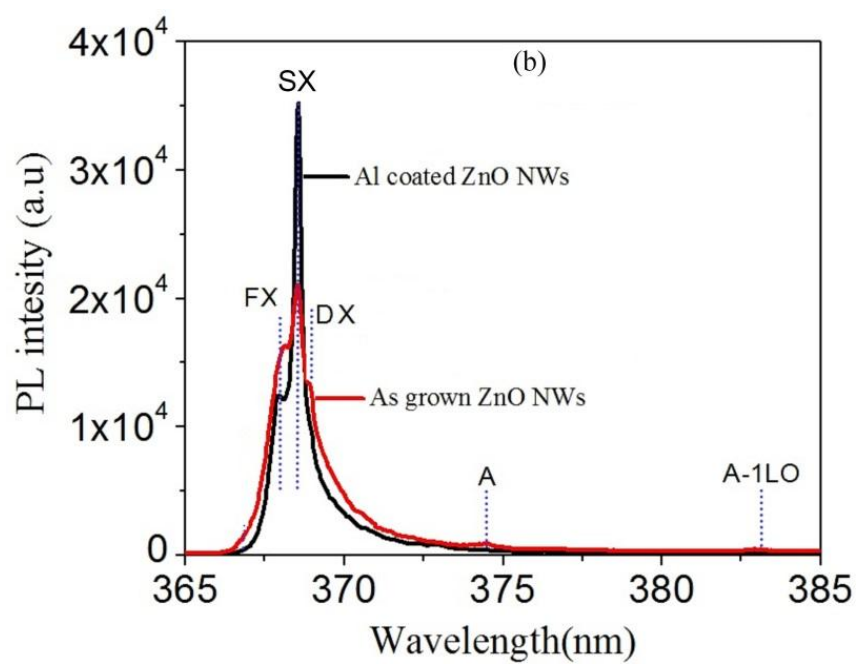
The room temperature and low temperature (8.5 K) PL spectra of as grown ZnO and those sputtered with Al nanoparticles with a shorter sputtering time (90 seconds) is presented in figure 9(a) and figure 9(b) where the first emission peak in figure 9(b) can be assigned to the free exciton (FX) at 367.6 nm (3.372 eV) [13, 21] and the second peak at 368.5 nm (3.364 eV) is due to the surface-excitonic emission band (SX) [21]. On the low-energy side, contributions from the recombination of excitons bound to neutral donors (DX) are observed at 3.69 nm (3.359 eV) [21] and defects located in the nanowires (A-line) gives rise to a PL peak at 373.5 nm (3.319 eV). Finally the PL peak located at 382.45 nm (3.242 eV) comes from the first-order longitudinal phonon replica of A- line [16, 22]. As is presented in the figure 9(b) the strong enhancement of NBE mostly is related to the enhancement of SX peak. Temperature dependent photoluminescence spectra of the as grown ZnO NWs and Al sputtered NWs are shown in figure 9(c) and figure 9(d) and the inset figure shows the peak energy versus temperature. The PL transitions are dominated by excitons bound to neutral donors at low temperatures with a very small free exciton peak visible. As the temperature increases, the free exciton thermalizes and cannot be seen at higher temperature. It can be observed that all peaks systematically shift to lower energy with increasing temperature. The temperature dependence of the PL intensity can be expressed by the Arrhenius expression [23]:

$$I(T) = \frac{I_0}{1 + A \exp\left(\frac{-\Delta E}{K_B T}\right)} \quad (4)$$

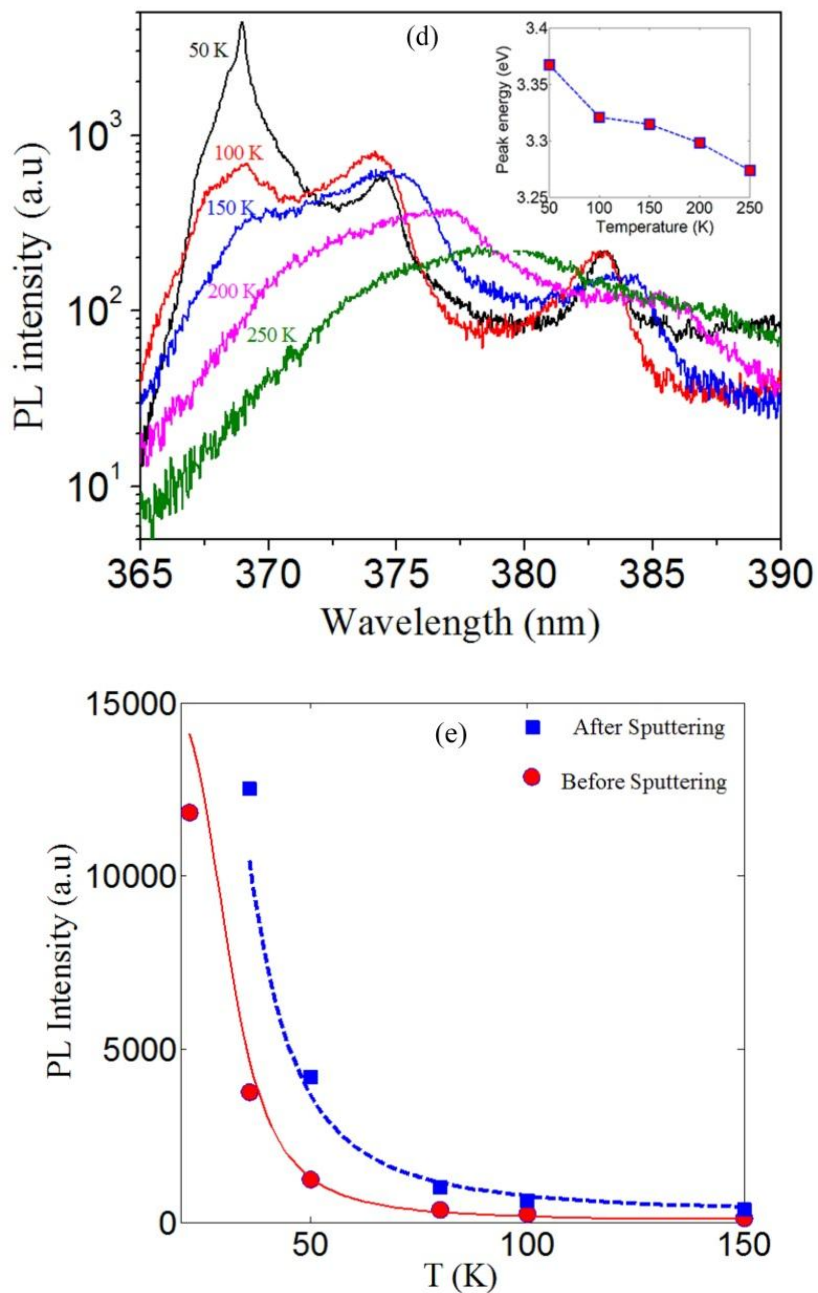
where  $\Delta E$  is the activation energy of the thermal quenching process,  $K_B$  is the Boltzmann constant,  $I_0$  is the emission intensity at 0 K,  $T$  is the thermodynamic temperature, and  $A$  is

a constant. The dependence of the integrated PL intensity of the ultra-violet (UV) band on temperature is shown in figure 9(e). By fitting the PL spectra with the Arrhenius expression the activation energy of SX was obtained which are 17.32 meV for as grown ZnO NWs and 14.47 meV for those ZnO nanowires decorated with sputtered metallic NPs which are in reasonable agreement with reported values [21, 24].



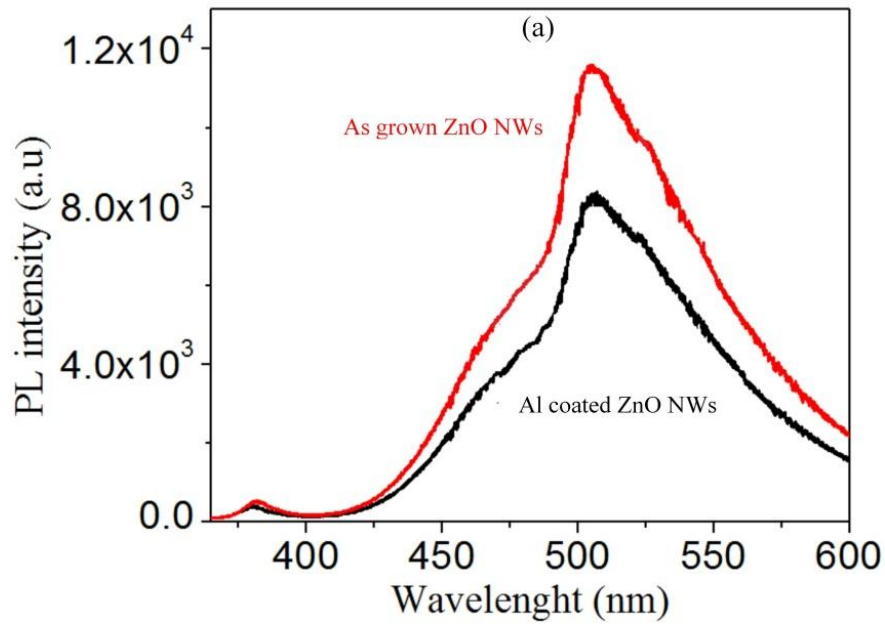






**Figure 9:** (a) Room temperature PL spectra of as grown ZnO NWs and Al sputtered (90 seconds) ZnO NWs, (b) PL spectra of as grown ZnO NWs and Al sputtered NWs at 8.5 K, (c) Temperature dependent Photoluminescence spectra (near UV region) of as grown ZnO NWs, (d) Al sputtered ZnO NWs and the insets show the peak energy versus temperature and, (e) integrated intensity of the neutral donor-bound exciton of ZnO nanowires as a function of temperature with theoretical fitting curve.

To investigate the effect of metallic NPs unexposed to Ar plasma, the PL from ZnO NWs coated with e-beam evaporated Al NPs were studied. The PL spectra of ZnO NWs before and after the e-beam Al evaporation under different deposition times are illustrated in figure 10. Here is seen a quenching of the NBE which may be due to the formation of metal induced gap states on the surface layer of NW [25].



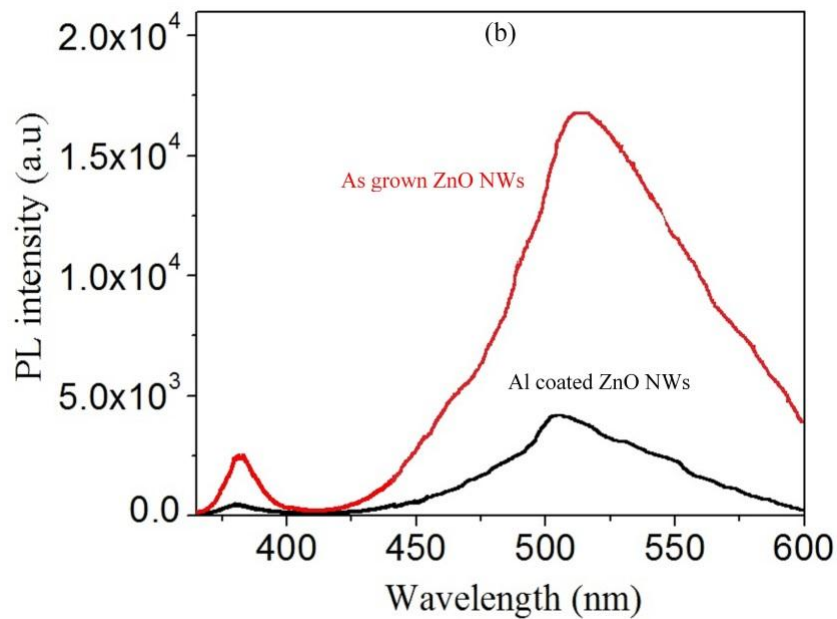


**Figure 10:** The room temperature PL spectra of as grown ZnO NWs (red) and ZnO NWs coated with Al nanoparticles by e-beam evaporation (black) under different evaporation times (a) 60 seconds and (b) 120 seconds.

It has been reported that when ZnO NWs are coated with a thin layer of metal, a large number of additional states within the band gap will be introduced [25]. These additional defects in the surface region will result in a higher trapping rate of electrons and therefore reducing the rate of excitonic recombination in the surface layer. As seen in the figure 10, e-beam evaporated thin film of Al on ZnO NWs is resulted in a relative quenching of NBE peak [25]. In the case of one-dimensional systems such as ZnO NWs where the ratio of surface to volume area is high, the surface defects, near surface traps and surface adsorbed species such as  $O_2$  molecules and  $OH^-$  offer alternative pathways for the de-excitation of photo-excited carriers and plays a significant role in the carrier relaxation dynamics [26, 27]. Typically, the  $O_2$  molecule, one of the most common adsorbates on the

surface of ZnO NW, undergo the chemisorption on the surface of NW by capturing a free electron from the n-type ZnO in a oxidizing ambient as shown in equation (2) [26-29].

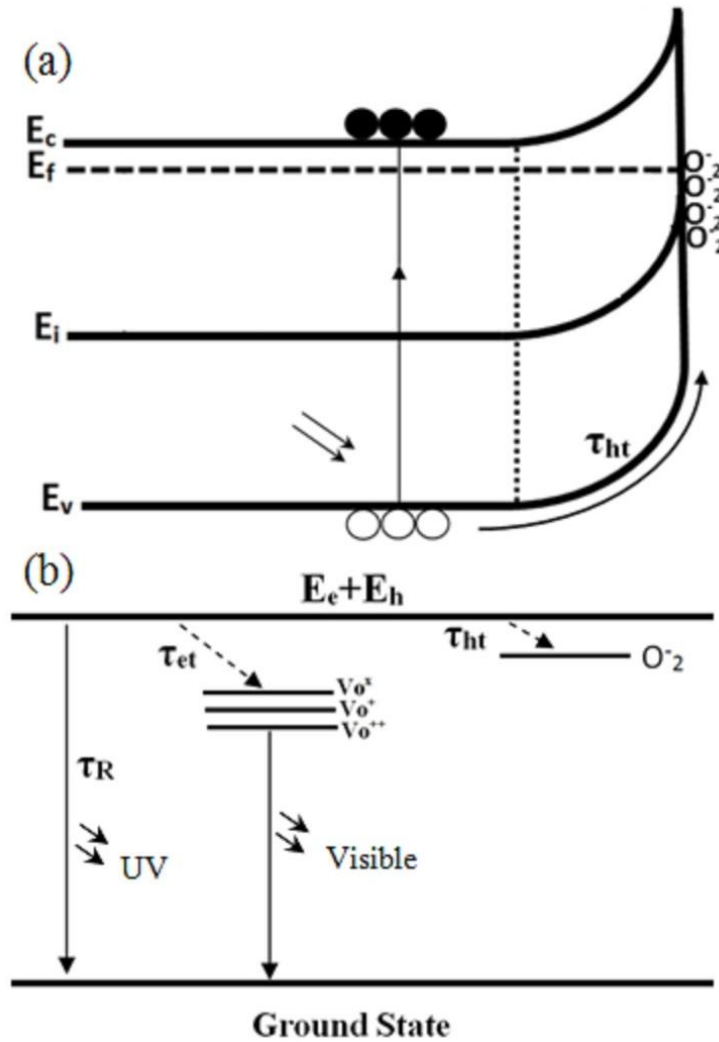


**Figure 11:** (a) Schematic diagram of the band bending of ZnO NWs and (b) the corresponding phenomenological model of the trapping pathways.



It is well known that intrinsic defects such as oxygen vacancies of as-grown ZnO NWs can be reduced by O<sub>2</sub> or Ar annealing and it results in a relative quenching of visible emission peak while the NBE peak is not changed in O<sub>2</sub> or Ar annealed ZnO NWs [30, 31]. However, the focus of this study is the reduction of surface defects and traps, not intrinsic defects. At the growth temperature of 900 °C in atmospheric pressure, a major part of the adsorbed species on the surface of ZnO NWs will be O<sub>2</sub><sup>-</sup> which acts as a surface trap. Upon the illumination, some photo-excited carriers will migrate to these surface traps. As shown in figure 11 a part of photo-excited holes are trapped by the adsorbed oxygen species on the surface of NW [26] and other photo-excited carriers are trapped by point defects such as oxygen vacancies and are believed to be the origin of visible emission peak in the PL spectra of ZnO NWs [24]. It is well known that the PL emission band at about 3.367 eV has its origin in the surface region of ZnO nanowires [14, 21] and with decreasing wire diameter its relative contribution to the NBE increases continuously [21]. Hence, fewer screened surface trapping sites lead to a smaller density of separated electrons and holes in the surface region which results in a higher density of excitons near the nanowires surface. So, surface cleaning of ZnO NWs from the trapping cites results in an increase of the SX band intensity [14]. The relative reduction of visible emission seen in ZnO NWS decorated with sputtered metallic NPs can also be attributed to the trapping cites at the surface of NW. Oxygen vacancies are believed to be the origin of visible emission peak in the PL spectra of ZnO NWs [24] and the mechanism of the visible emission peak with a maximum at 2.45 eV originates from single positively charged oxygen vacancies (Vo<sup>+</sup>) located within the ZnO nanowire. Three different types of oxygen

vacancies can occur in ZnO NWs: the doubly ionized oxygen vacancies  $V_{O^{++}}$ , the singly ionized oxygen vacancies  $V_{O^+}$  and the neutral oxygen vacancies  $V_{O^x}$  are shown in figure 11(b) [24]. These vacancies need to be activated by a hole. So, the activation process requires photo-excited holes which are trapped at surface. Then, the holes may tunnel into the deep-level defects to create the optically active oxygen vacancies [14]. This model is based on the assumption that the surface related processes are dominating for ZnO nanowires [14]. The trapping sites like  $O^{2-}$ ,  $O^-$  or  $OH^-$  are located at the surface of NW lead to a separation of electron and hole pairs in this region. Then the holes will be captured at the surface traps. By cleaning the surface of ZnO NWs from the trapping sites, fewer holes are able to be captured at the surface traps which quench the visible emission peak [14].

The experimental results demonstrate that decorating the ZnO NWs with metal NPs in presence of high energy Ar atoms cleans the surface of ZnO NWs from near surface traps and surface adsorbed species, thus it leads to a strong enhancement of NBE emission and a relative reduction of visible peak. Comparison of the room temperature PL spectra shown in the figure 8(a) and figure 9(a) is also showing that the increasing of sputtering time can lead to a better surface cleaning and therefore a stronger enhancement of NBE.

Although it is reported that hydrogen atoms can act as shallow donors and occupy interstitial sites in addition to the oxygen vacancies and it can results in the enhancement of the near band edge emission and quenching of the visible emission peak [15, 32]. However, since the metal deposition is performed in a high vacuum ( $10^{-6}$  Torr) before starting the plasma, and ultra-pure Ar was used, it is expected that the presence of

hydrogen is negligible during sputtering process and the strong enhancement of the NBE and quenching of visible peak cannot be because of hydrogen incorporation.

### **3. INFLUENCE OF SUBSTRATE ON THE FLUORESCENCE ON THE EMISSION OF ZINC OXIDE NANOWIRES AND CORE-SHELL CADMIUM SELENIDE/ZINC SULFIDE QUANTUM DOTS**

In this chapter we have investigated the effect on the intensity of photoluminescence (PL) spectra of cadmium selenide/zinc sulfide (CdSe/ZnS) core-shell quantum dots (QDs) and as grown ZnO NWs when deposited on different substrates (gallium arsenide, silicon, glass and indium tin oxide-coated glass). The experimental results show that the PL intensity is the highest for the gallium arsenide (GaAs) and the least from the indium tin oxide-coated glass (ITO-coated glass) substrate for both the quantum dots and the ZnO NWs. These experimental results were simulated by taking into account the scattered field from different substrates and were seen to be in agreement with the experimental results. We found that the PL intensity is a function of scattered light from the surface of substrate rather than type of heterojunction formed between the deposited material and substrate.

#### **3.1 Experimental**

The CdSe/ZnS core-shell quantum dots were home-grown with an average diameter size around 10 nm and ZnO NWs were grown as described in **Section 2.2**. Four substrates were used for our experimental work and were n-type GaAs (100), n-type silicon (100), Glass and ITO-coated glass substrates from Aldrich Company. Each substrate was cut into equal sizes of 1 cm by 1 cm. To remove any surface impurities, the substrates were rinsed thoroughly using deionized water and isopropanol and dried with dry nitrogen gas before they were used. Equal amounts of the CdSe/ZnS QDs as well as the ZnO NWs were



dropcast on the four substrates and the samples were allowed to dry. The samples made with the QDs and ZnO NWs were characterized using PL set-up described in chapter 1.

### **3.2 Results and discussion**

The room temperature PL spectra of CdSe/ZnS quantum deposited on the GaAs, Silicon, Glass and ITO-coated glass are shown in figure 12. For all the samples, the PL spectra has a peak value at a wavelength of about 582 nm with different PL intensities. Quantum dots deposited on the GaAs have the highest PL intensity and quantum dots on the ITO-coated glass show the lowest PL intensity. The experiments were repeated by replacing the CdSe/ZnS quantum with the ZnO NWs. Figure 13 represents the PL spectra of ZnO NWs on the four different substrates that were used for the quantum dots. The results were again similar in that the PL intensity varies in similar manner to the PL intensity in the case of the CdSe/ZnS quantum dots on the different substrates. The physical gap between the deposited materials and substrates may results in presence of surface dangling bonds, which can act as trap states for charge carriers and thereby reduce the fluorescence. Hence, In order to investigate the effect of trap states the room temperature PL spectra of quantum dots deposited on the different substrates were measured under exposure of different light intestines. As seen in figure 14 the PL intensity varies in similar manner to PL spectra shown in figure 14.

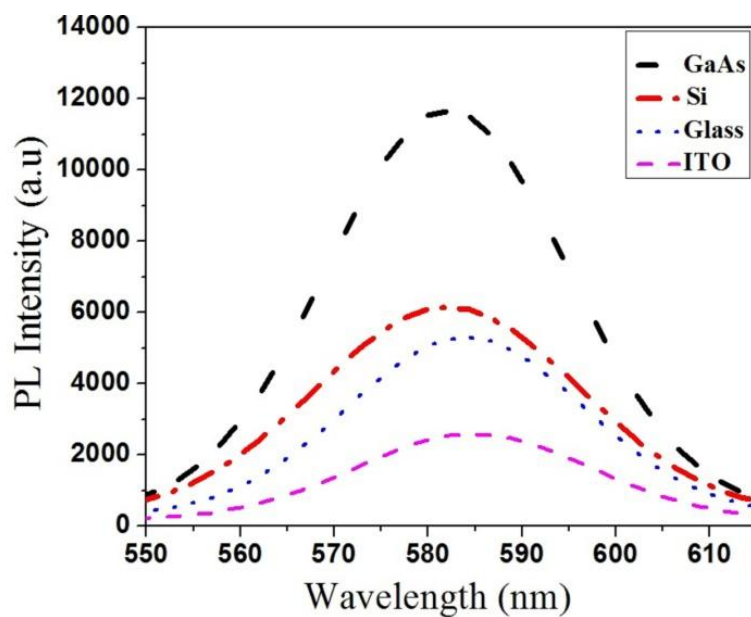


**Figure 12:** Photoluminescence spectra of CdSe/ZnS quantum dots on different substrates.

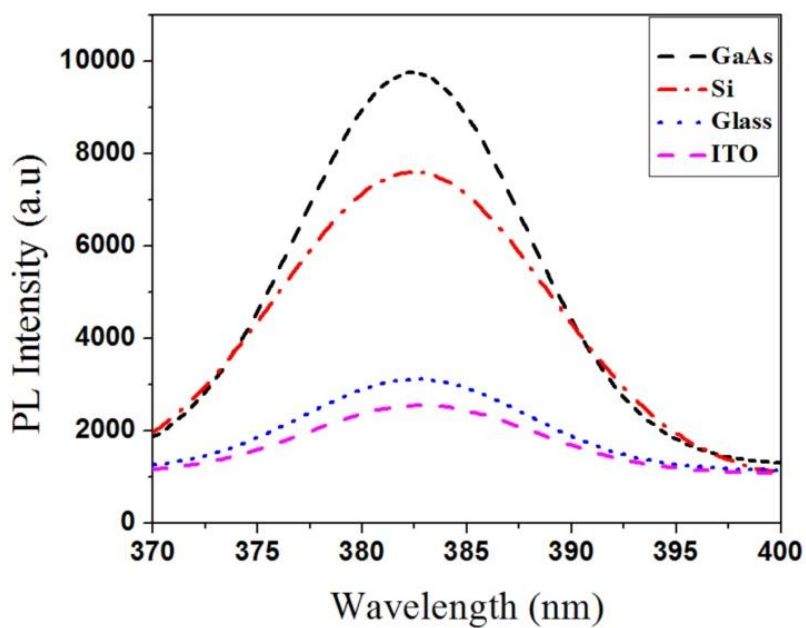


**Figure 13:** Photoluminescence spectra of ZnO nanowires on different substrates.

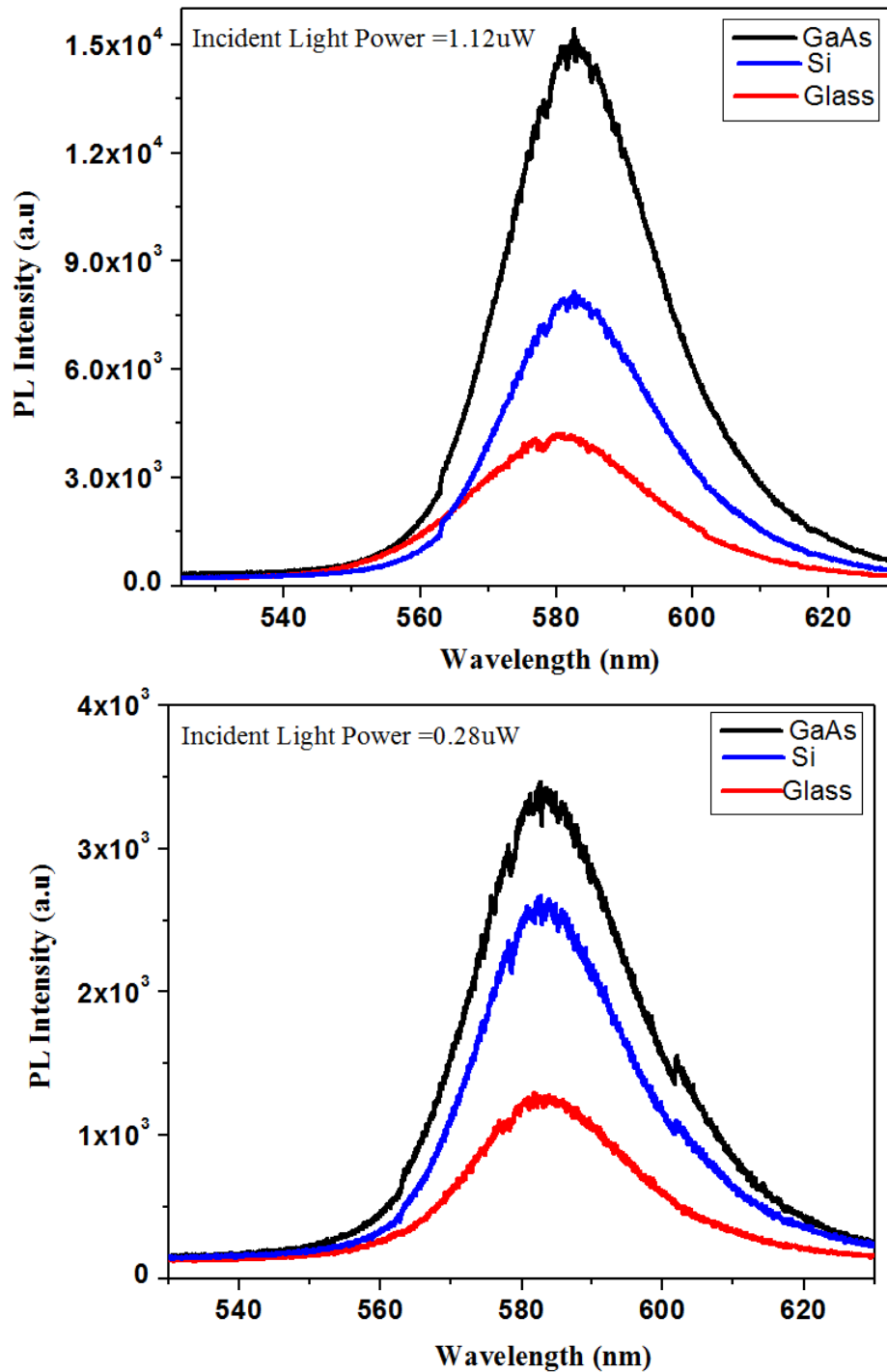


**Figure 14:** Photoluminescence spectra of CdSe/ZS on different substrates under exposure of different incident light power intensity.

### 3.2.1 Heterojunction effects

Since it has been reported that the energy barrier at the interface might affect the PL spectra of ZnO NWs [33] and the lower barrier at the interface might result in a stronger PL intensity, we investigated the PL intensity difference by characterization of the different types of junctions formed at the interface between the deposited materials and substrates. The energy band gap discontinuities for each substrate material, ZnO and QDs are considered as shown in figure 15, separately. GaAs with an electron affinity about 4.07 eV and silicon with an electron affinity about 4.05 eV form a heterojunction in contact with ZnO NWs. Substituting the values of the respective coefficients from table I, the energy band diagram of the heterojunction formed between the ZnO/GaAs and ZnO/Silicon are shown in figure 15(a) and figure 15(b), where  $\phi_s$  and  $\chi_s$  are the work function and electron affinity, respectively. The work function of ITO is reported to vary between 4.1eV to 4.7eV for the oxygen plasma treatment [34]. By choosing the value of 4.1eV and using the data from table I the estimated negative Schottky barrier height of ITO-ZnO contact is -0.11 eV which confirms that the ITO-ZnO interface behaves as ohmic contact as is reported experimentally [35, 36]. The energy band diagram of ITO-ZnO junction is shown at figure 15(c). The last type of heterojunction is the contact between a ZnO NWs serving as a semiconductor and glass as an insulator shown in figure 15(d). Using a value about 5.5eV as work function [37] and an electron affinity value about 4.95 eV for CdSe [38] the energy band diagram of CdSe/ZnS and different substrates are also calculated and illustrated in figure 15(e) to figure 15(h).

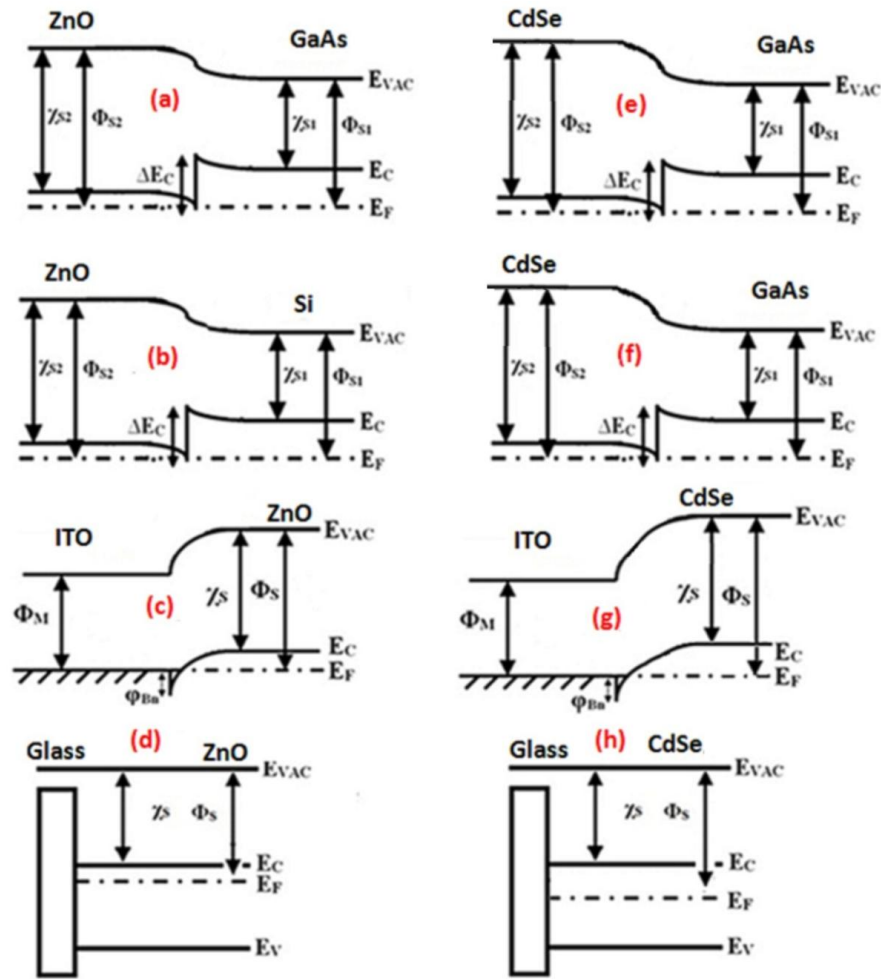


**Figure 15:** (a) Energy band diagram of ZnO-GaAs heterojunction, (b) Energy band diagram of ZnO-Si heterojunction where  $\phi_{s1}$  and  $\chi_{s1}$  be the work function and electron affinity of substrates and  $\phi_{s2}$  and  $\chi_{s2}$  be the work function and electron affinity of ZnO respectively (c) Energy band diagram of ZnO-ITO contact, where  $\chi_s$  is the electron affinity of ZnO;  $\phi_s$  be the work function of ZnO and  $\phi_m$ -work function of ITO (d) Energy band diagram of ZnO-glass heterojunction, where  $\phi_s$  and  $\chi_s$  be the work function and electron affinity of ZnO respectively, (e) Energy band diagram of CdSe/ZnS-GaAs heterojunction (ZnS is too narrow and has not been put in the heterojunction because of the very small effect), (f) Energy band diagram of CdSe/ZnS-Si heterojunction, (g) Energy band diagram of CdSe/ZnS-ITO contact, and (h) Energy band diagram of CdSe/ZnS-glass heterojunction.

Here the band bending due to defects at the interface has been ignored. The comparison of energy barriers at the interface shows that the energy barrier seen by electrons at the interface of ITO/ZnO and ITO/CdSe is minimum showing a negative energy barrier offset, while the energy barrier between glass and deposited materials is the highest. Thus the hypothesis that the substrates produce additional carriers that contribute to the observed PL intensities is contradictory to the experimental results.

### **3.2.2 Scattering effects**

To investigate the effects of scattering of the incident light from the substrates on the intensity of the PL spectra, we used FEKO, commercial Electromagnetic simulation software. Figure 5 shows the schematic diagram of the structure used for simulation. The substrates used in experiments are modeled by an infinite plane with a thickness, 40 times thicker than incident light wavelength and a normal vector parallel to the Z direction as shown in figure 16. The incident wave is a single frequency plane wave with a wavelength equal to 325 nm and the incident angle  $\theta = 30$ . The total Poynting vector value ( $P_x$ ,  $P_y$ , and  $P_z$ ) of the near-field is illustrated in figure 17. The Poynting vector represents the directional energy flux density from the substrate which can be described as the following:

$$\bar{P} = \bar{E} \times \bar{H} \quad (1)$$

where E is the electric field and H is the magnetic field. As shown in figure 16, the Poynting vector value of the near field which represents the intensity of incoming and scattered electromagnetic wave from the surface of GaAs, silicon and glass decreased for the different substrates as that for the PL intensity obtained from the experimental results. Since the intensity of incident plane wave and incident angle ( $\theta = 30$ ) wave were kept

constant the near field Poynting vector shown in figure 16 can be interpreted as the Poynting vector value of scattering wave.

**Table I: Band gap and electron affinities of different material**

Material Parameters	GaAs <sup>a</sup>	Si <sup>b</sup>	ZnO <sup>c</sup>
Band gap (eV)	1.43	1.12	3.37
Electron Affinity (eV)	4.07	4.05	4.5

<sup>a</sup>References 39 and 42

<sup>b</sup>References 40 and 43

<sup>c</sup>References 41 and 44

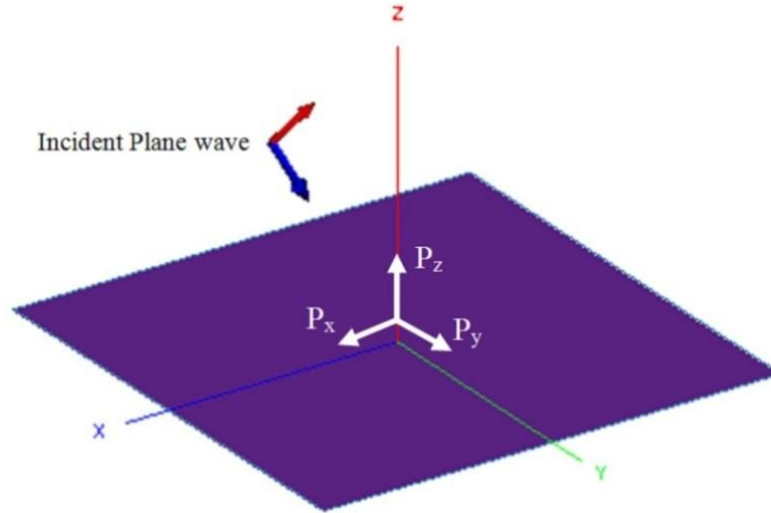


**Figure 16:** The schematic diagram of structure used in simulation and the incident plane wave where the red arrow represents the electric field component and the blue arrow represents the magnetic field component.

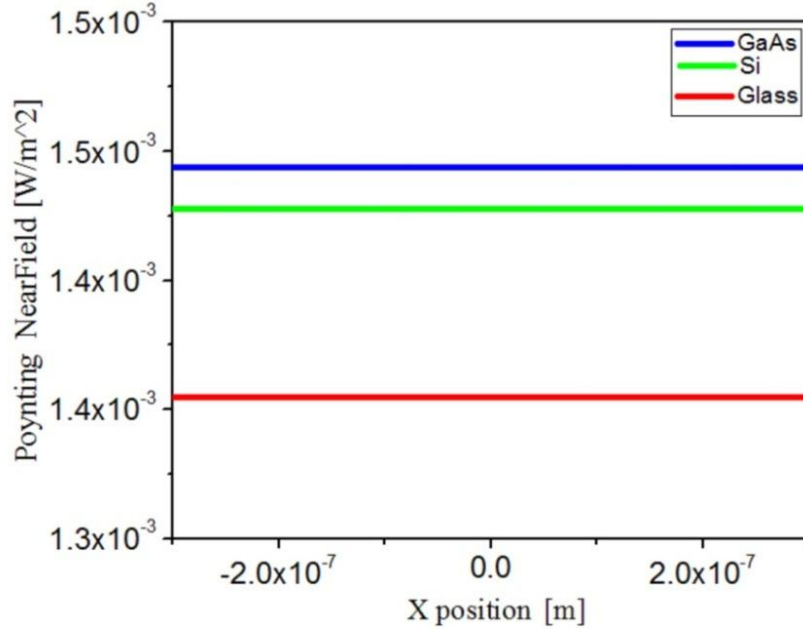


**Figure 17:** The Poynting vector of scattered field versus the X position.

The scattered wave can be thought as reflection from all angles from the surface of substrate while reflection coefficient of plane waves polarized normal and parallel to the substrate can be expressed as shown in equation 2 and equation 3.

$$\Gamma_{\perp} = \frac{\cos \theta_i - \sqrt{(\epsilon_{2r}/\epsilon_{1r}) - \sin^2 \theta_i}}{\cos \theta_i + \sqrt{(\epsilon_{2r}/\epsilon_{1r}) - \sin^2 \theta_i}} \quad (2)$$

$$\Gamma_{\parallel} = \frac{-\cos \theta_i + (\epsilon_{1r}/\epsilon_{2r})\sqrt{(\epsilon_{2r}/\epsilon_{1r}) - \sin^2 \theta_i}}{\cos \theta_i + (\epsilon_{1r}/\epsilon_{2r})\sqrt{(\epsilon_{2r}/\epsilon_{1r}) - \sin^2 \theta_i}} \quad (3)$$

where  $\theta_i$  is the incident angle and  $\epsilon$  is the relative permittivity of medium [45]. The simulation results indicate that it is the scattering field from the surface of the substrate that



influences the intensity of the PL for the quantum dots as well as the nanowires. This argument can be extended in case of ITO-coated glass as well. Metals cause absorption loss into the cavity causing a loss in the scattering [46]. Hence, the PL intensity of those quantum dot and ZnO NWs deposited on the ITO-coated glass is even lower than glass substrate. The comparisons of simulation and experimental results demonstrate that the intensity of scattered field at the surface is responsible for the different PL intensity from different substrates rather than the band-gap discontinuity between the deposited material and the substrate.

However the absorption of scattered light in colloidal systems of aggregated particles should be considered. The influence of aggregation is strongly depending on the size and shape of the aggregate for absorbing particles when the single sphere shows resonant extinction. In this case, the resonance of the single sphere splits into many new resonances for the aggregate, most of which are positioned at larger wavelengths than the single sphere resonance. However, in the case of non-absorbing particles the scattering spectra of aggregates scarcely differ from the scattering spectra of single spheres [47]. Hence, in case of CdSe/ZnS QDs and ZnO NWs which have absorbing properties between metals and non-absorbing materials the influence of aggregation on the scattering spectra should be considered. By considering the difference in scattering field from different substrates and different aggregation morphologies formed on the different substrates it can be concluded that the different PL intensities seen in experimental results can be a result of these two effects.

#### **4. MODELING THE EFFECT OF PIEZOELECTRIC CHARGES ON THE SURFACE DEPLETION REGION AND SURFACE POTENTIAL OF ZINC OXIDE NANOWIRES.**

1D nanostructures have attracted much attention recently in the fabrication of various nanoelectronic devices [48], nanogenerators [49] and sensors [50]. In particular, piezoelectric semiconductor materials such as ZnO and GaN have been the focus of much research. They can be used to convert mechanical energy to electrical energy and also since they are semiconductors, they can be used as a junction device for performing diode and transistor-type functions [51]. These properties make them strong candidates for use in electromechanically coupled sensors and transducers [52]. The application of piezoelectric semiconductor NWs, however, requires good understanding of the electrical properties which might be modified by its piezoelectric properties. For instance, since the demonstration of first nano-scale piezoelectric energy harvester device based on single ZnO nanowires there have been many conflicts ideas behind the operation of piezoelectric nano-generator devices mainly due to the large density of free carriers which exist in the crystal structure of piezoelectric semiconductor materials such as ZnO. The piezoelectric constitutive equations can be applied to estimate the generated piezoelectric potential inside the crystal structure of piezoelectric materials with a zero or negligible free carriers. But, the piezoelectric metal oxide semiconductors such as ZnO nanowires have a large density of free carriers up to  $10^{18} \text{ cm}^{-3}$ .

In this chapter, the effect of induced piezoelectric charges on the surface depletion region and the electrostatic surface potential of ZnO NWs have been studied and a new model is developed which strongly satisfied the observed experimental results reported in

the literature. In the developed model the presence of free carriers in the crystal structure is also considered. In order to develop our model first the electrostatic potential and depletion width in piezoelectric semiconductor nanowires are derived by considering a non-depleted region and a surface depleted region and solving the Poisson equation. By determining the piezoelectric induced charge density, in terms of equivalent density of charges, the effect of piezoelectric charges on the surface depletion region and the distributed electric potential in the nanowire have been investigated. The numerical results demonstrate that the ZnO NWs with a smaller radius have a larger surface depletion region which results in a stronger surface potential and depletion region perturbation by induced piezoelectric charges.

#### **4.1 Relevant properties of piezoelectricity**

Piezoelectricity is the result of two processes. One is the rearrangement of electronic states in the crystal and another one is displacement of charged constituents within the lattice [53]. Compound semiconductors usually belong to non-Centro symmetric crystal groups. They are thus piezoelectric materials and their crystals usually possess spontaneous polarization. The crystal symmetry of ZnO is responsible for the different components of the internal polarization, spontaneous polarization and piezoelectric polarization. The charge produced by the piezoelectric effect is a bound charge (polarization or dielectric displacement) and the piezoelectric strain equations can be expressed as the following [54, 55].

$$T = -e.E + c^E : S \quad (1)$$

$$D = \epsilon^S . E + e : S \quad (2)$$

where  $T$  is the stress,  $c$  is the elastic stiffness constant,  $e$  is the polarization constant,  $E$  is the electric field,  $D$  is the electric displacement,  $S$  is the strain and, and  $\epsilon$  is the electric permittivity. On application of an external strain to a piezoelectric crystal, a macroscopic polarization is produced as a result of the displacements of ions [56]. The above equations imply that in the case of an ideal insulator, in which the density of free carriers is zero or negligible, the generation of the piezoelectric charge might be considered equivalent to the generation of an electrical field or a potential [54]. However, in case of a piezoelectric semiconductor where the density of free carriers is not negligible, the piezoelectric constitutive equations cannot be applied. In the depletion region of semiconductor where the density of free carriers is negligible the piezoelectric charges may be added to the ionized impurities (donor or acceptor). In the non-depleted region where the density of free carriers is not negligible the free carriers migrate to the region where piezoelectric polarization appears to maintain the quasi-neutrality. The migration time of free carriers is on the order of the dielectric relaxation time which can be described as the following [55, 57]:

$$\tau_r = \frac{\epsilon}{\sigma} \quad (3)$$

where  $\epsilon$  is electric permittivity and  $\sigma$  is the conductivity of the material. In the case of ZnO NWs which have a density of free electrons around  $10^{18} \text{ cm}^{-3}$  [54, 58], the relaxation time is about one picosecond. Since the piezoelectric polarization will be canceled in the non-depleted region of a piezoelectric semiconductor, we investigate the effect of piezoelectric polarization in the depleted region of a single ZnO NW.

## 4.2 Mechanical analysis

The application of ZnO NWs as nano generators has been demonstrated [52] by applying a bending force to convert the mechanical energy to electrical energy. In detailed studies by Araneo *et al.* [59] and Romano *et al.* [60] the created piezoelectric potential created in a 1D structure subjected to a compressive/tensile force has been studied and the piezopotential drop between the tip and the base of the nanowire as a function of the force/pressure has been investigated. In our study, the stress components at the cross-sectional area of nanowire which result in a radial piezoelectric polarization are the focus of study. Considering a uniform plane wave propagating with an arbitrary angle in the XZ plane of a wurtzite crystal, the radial component of the piezoelectrically induced polarization tensor in cylindrical coordinate system can be given as shown in equation 4 [55, 56].

$$\begin{aligned}
 p_r = & \left( e'_{x1} \cos^3 \Phi + e'_{x2} \cos \Phi \sin^2 \Phi + e'_{y6} \sin \Phi \sin 2\Phi \right) \frac{\partial u_r}{\partial r} \\
 & + \left( e'_{x1} \cos \Phi \sin^2 \Phi + e'_{x2} \cos^3 \Phi - e'_{y6} \sin \Phi \sin 2\Phi \right) \\
 & \times \left( \frac{u_r}{r} + \frac{1}{r} \frac{\partial u_r}{\partial \Phi} \right) + e'_{x3} \cos \Phi \frac{\partial u_z}{\partial z} + \left( e'_{y4} \sin \Phi \cos \Phi - e'_{x5} \cos \Phi \sin \Phi \right) \left( \frac{\partial u_\Phi}{\partial z} + \frac{1}{r} \frac{\partial u_z}{\partial \Phi} \right) \\
 & + \left( e'_{y4} \sin^2 \Phi + e'_{x5} \cos^2 \Phi \right) \times \left( \frac{\partial u_r}{\partial z} + \frac{\partial u_z}{\partial r} \right) + \left( -e'_{x1} \cos \Phi \frac{\sin 2\Phi}{2} + e'_{x2} \cos \Phi \frac{\sin 2\Phi}{2} + e'_{y6} \sin \Phi \cos 2\Phi \right) \\
 & \times \left( \frac{1}{r} \frac{\partial u_r}{\partial \Phi} + \frac{\partial u_\Phi}{\partial r} - \frac{u_\Phi}{r} \right)
 \end{aligned} \tag{4}$$

In the cylindrical polar coordinate system, the piezoelectric stress tensor  $\bar{e}'$  for propagation at an angle  $\eta$  in the XZ plane of a wurtzite crystal transforms as [55, 56, and 61]

$$\bar{e}'' = [a'] [\bar{e}'] [\bar{M}'] \tag{5}$$

where the coordinate transformation matrix  $[a']$  is given by

$$[a'] = \begin{pmatrix} \cos \Phi & \sin \Phi & 0 \\ -\sin \Phi & \cos \Phi & 0 \\ 0 & 0 & 1 \end{pmatrix} \quad (6)$$

where the transformation matrix  $[M']$  can be derived from  $[a']$ , and the piezoelectric stress tensor  $\bar{e}'$  is given by [55, 56 and 61]

$$\bar{e}' = \begin{pmatrix} e'_{x1} & e'_{x2} & e'_{x3} & 0 & e'_{x5} & 0 \\ 0 & 0 & 0 & e'_{y4} & 0 & e'_{y6} \\ e'_{z1} & e'_{z2} & e'_{z3} & 0 & e'_{z5} & 0 \end{pmatrix} \quad (7)$$

With the following components [56]

$$\begin{aligned} e'_{x1} &= -e_{z1} \sin \eta \cos^2 \eta - e_{z3} \sin^3 \eta - e_{x5} \cos \eta \sin 2\eta, \\ e'_{x2} &= -e_{z1} \sin \eta, \\ e'_{x3} &= -e_{z1} \sin^3 \eta - e_{z3} \cos^2 \eta \sin \eta + e_{x5} \cos \eta \sin 2\eta, \\ e'_{x5} &= -e_{z1} \frac{\sin \eta \sin 2\eta}{2} + e_{z3} \frac{\sin \eta \sin 2\eta}{2} + e_{x5} \cos \eta \cos 2\eta, \\ e'_{y4} &= e_{x5} \cos \eta, \\ e'_{y6} &= -e_{x5} \sin \eta, \\ e'_{z1} &= e_{z1} \cos^3 \eta + e_{z3} \cos \eta \sin^2 \eta - e_{x5} \sin \eta \sin 2\eta, \\ e'_{z2} &= e_{z1} \cos \eta, \\ e'_{z3} &= e_{z1} \cos \eta \sin^2 \eta + e_{z3} \cos^3 \eta + e_{x5} \sin \eta \sin 2\eta, \\ e'_{z5} &= e_{z1} \frac{\cos \eta \sin 2\eta}{2} - e_{z3} \frac{\cos \eta \sin 2\eta}{2} + e_{x5} \sin \eta \cos 2\eta \end{aligned}$$

Hence, in cylindrical coordinates the piezoelectric stress tensors can be expressed as [56]

$$\bar{e}'' = \begin{pmatrix} e''_{x1} & e''_{x2} & e''_{x3} & e''_{x4} & e''_{x5} & e''_{x6} \\ e''_{y1} & e''_{y2} & e''_{y3} & e''_{y4} & e''_{y5} & e''_{y6} \\ e''_{z1} & e''_{z2} & e''_{z3} & e''_{z4} & e''_{z5} & e''_{z6} \end{pmatrix} \quad (8)$$

Thus the piezoelectrically induced electric polarization  $\bar{p}$  which is a three component vector is expressed by the matrix equation of the piezoelectric tensor  $\bar{e}''$  and the acoustic strain vector  $\bar{s}$  a six-component strain vector

$$\bar{p} = \bar{e}'' \cdot \bar{s} \quad (9)$$

$$\bar{p} = \begin{pmatrix} p_r \\ p_\Phi \\ p_z \end{pmatrix}$$

$$\bar{s} = \begin{pmatrix} s_{rr} \\ s_{\Phi\Phi} \\ s_{zz} \\ 2s_{z\Phi} \\ 2s_{rz} \\ 2s_{r\Phi} \end{pmatrix}$$

Therefore, the components of the piezoelectrically induced polarization tensor can be given as [56]

$$\begin{aligned} p_r = & \left( e'_{x1} \cos^3 \Phi + e'_{x2} \cos \Phi \sin^2 \Phi + e'_{y6} \sin \Phi \sin 2\Phi \right) \frac{\partial u_r}{\partial r} \\ & + \left( e'_{x1} \cos \Phi \sin^2 \Phi + e'_{x2} \cos^3 \Phi - e'_{y6} \sin \Phi \sin 2\Phi \right) \\ & \times \left( \frac{u_r}{r} + \frac{1}{r} \frac{\partial u_r}{\partial \Phi} \right) + e'_{x3} \cos \Phi \frac{\partial u_z}{\partial z} + \left( e'_{y4} \sin \Phi \cos \Phi - e'_{x5} \cos \Phi \sin \Phi \right) \left( \frac{\partial u_\Phi}{\partial z} + \frac{1}{r} \frac{\partial u_z}{\partial \Phi} \right) \\ & + \left( e'_{y4} \sin^2 \Phi + e'_{x5} \cos^2 \Phi \right) \times \left( \frac{\partial u_r}{\partial z} + \frac{\partial u_z}{\partial r} \right) + \left( -e'_{x1} \cos \Phi \frac{\sin 2\Phi}{2} + e'_{x2} \cos \Phi \frac{\sin 2\Phi}{2} + e'_{y6} \sin \Phi \cos 2\Phi \right) \\ & \times \left( \frac{1}{r} \frac{\partial u_r}{\partial \Phi} + \frac{\partial u_\Phi}{\partial r} - \frac{u_\Phi}{r} \right) \end{aligned} \quad (10)$$

$$\begin{aligned}
p_\Phi = & \left( e'_{x1} \sin \Phi \cos^2 \Phi - e'_{x2} \sin^3 \Phi + e'_{y6} \cos \Phi \sin 2\Phi \right) \frac{\partial u_r}{\partial r} - \left( e'_{x1} \sin^3 \Phi + e'_{x2} \sin \Phi \cos^2 \Phi + e'_{y6} \cos \Phi \sin 2\Phi \right) \\
& \times \left( \frac{u_r}{r} + \frac{1}{r} \frac{\partial u_\Phi}{\partial \Phi} \right) - e'_{x3} \sin \Phi \frac{\partial u_z}{\partial z} + \left( e'_{y4} \cos^2 \Phi + e'_{x5} \sin^2 \Phi \right) \left( \frac{\partial u_\Phi}{\partial z} + \frac{1}{r} \frac{\partial u_z}{\partial \Phi} \right) \\
& + \left( e'_{y4} \sin \Phi \cos \Phi - e'_{x5} \sin \Phi \cos \Phi \right) \left( \frac{\partial u_r}{\partial z} + \frac{\partial u_z}{\partial r} \right) + \left( e'_{x1} \sin \Phi \frac{\sin 2\Phi}{2} - e'_{x2} \sin \Phi \frac{\sin 2\Phi}{2} + e'_{y6} \cos \Phi \cos 2\Phi \right)
\end{aligned} \tag{11}$$

$$\begin{aligned}
& \times \left( \frac{1}{r} \frac{\partial u_r}{\partial \Phi} + \frac{\partial u_\Phi}{\partial r} - \frac{u_\Phi}{r} \right) \\
p_z = & \left( e'_{z1} \cos^2 \Phi + e'_{z2} \sin^2 \Phi \right) \frac{\partial u_r}{\partial r} + \left( e'_{z1} \sin^2 \Phi + e'_{z2} \cos^2 \Phi \right) \left( \frac{u_r}{r} + \frac{1}{r} \frac{\partial u_\Phi}{\partial \Phi} \right) + e'_{z3} \frac{\partial u_z}{\partial z} \\
& - e'_{z5} \sin \Phi \left( \frac{\partial u_\Phi}{\partial z} + \frac{1}{r} \frac{\partial u_z}{\partial \Phi} \right) + e'_{z5} \cos \Phi \left( \frac{\partial u_r}{\partial z} + \frac{\partial u_z}{\partial r} \right) + \left( -e'_{z1} \frac{\sin 2\Phi}{2} + e'_{z2} \frac{\sin 2\Phi}{2} \right) \\
& \times \left( \frac{1}{r} \frac{\partial u_r}{\partial \Phi} + \frac{\partial u_\Phi}{\partial r} - \frac{u_\Phi}{r} \right)
\end{aligned} \tag{12}$$

where  $u$  is the displacement and the piezoelectric stress tensor  $\bar{e}'$  is given by [56, 61]

$$\bar{e}' = \begin{pmatrix} e'_{x1} & e'_{x2} & e'_{x3} & 0 & e'_{x5} & 0 \\ 0 & 0 & 0 & e'_{y4} & 0 & e'_{y6} \\ e'_{z1} & e'_{z2} & e'_{z3} & 0 & e'_{z5} & 0 \end{pmatrix} \tag{13}$$

In following sections the effect of this piezoelectric polarization component in the surface depletion region of ZnO is modeled by considering an equivalent density of piezoelectric charges.



### 4.3 Depletion region in a 1D structure

It is well known that the surface depletion region is not negligible in 1D structures where the ratio of surface to volume area is high. In case of ZnO NWs, by capturing electrons, the adsorption of ambient oxygen on ZnO nanowire surface causes a space charge region and an upward band bending near the surface, which results in a surface depletion layer [62]. In figure 18, the schematic representation of a single nanowire and its band bending in the radial direction is depicted, the radius of non-depleted region is  $r_{elec}$  and the depletion region width is  $d$ . The depletion region in a 1D structure can be derived based on the theory proposed by Schmidt *et al.* [63]. The surface charges ( $N_s$ ) should be balanced by a negative depletion charge to satisfy charge neutrality. The surface charge density can be described as following [55, 63 and 64]:

$$N_s = e^2 D_{it} \Psi_s \quad (14)$$

where  $D_{it}$  is the interface state density,  $e$  is the electron charge and  $\psi_s$  is the surface potential. Defining the electrostatic potential  $\psi_r$  in a way that is illustrated in figure 18 and considering the fully ionized donors and acceptors the charge density in the depletion region can be written as [65].

$$\rho(r) = q[N_v \exp(\frac{-E_g}{2KT}) \exp(\frac{-q}{KT} \psi_r) - N_c \exp(\frac{-E_g}{2KT}) \exp(\frac{q}{KT} \psi_r) + N_D - N_A] \quad (15)$$

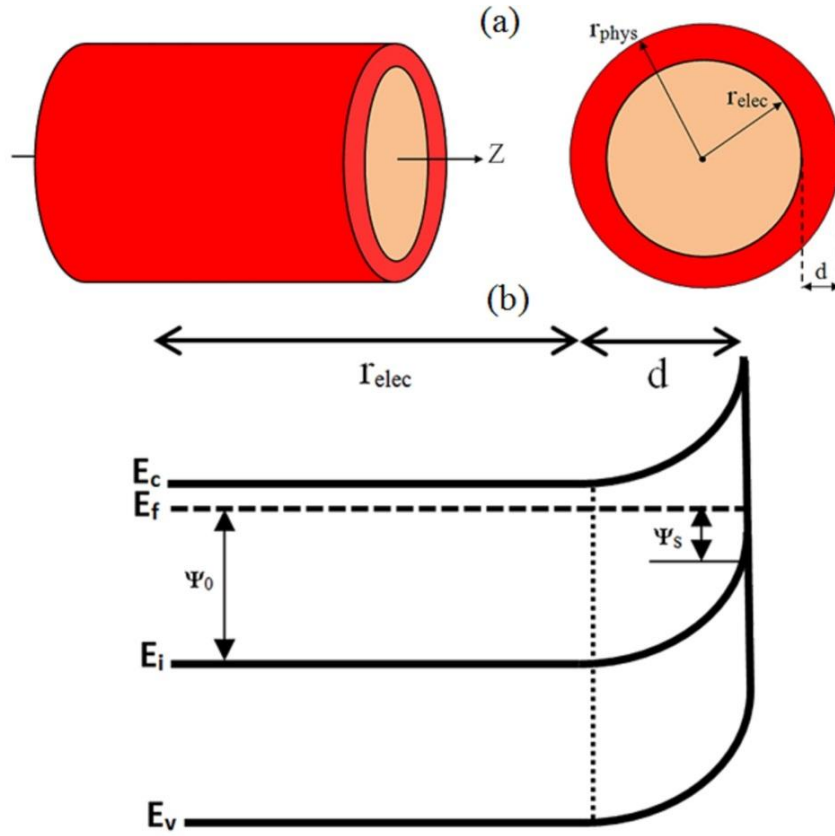


**Figure 18: The schematic representation of the nanowire (a) and its band bending (b).**

where  $N_v$  and  $N_c$  are the effective densities of states. Assuming an abrupt transition between the depletion layer and the non-depleted semiconductor and neglecting diffusion of charge carriers between the two regions, the charge density in the depletion region can be approximated as [55]:

$$\rho(r) \approx q(N_D - N_A) \quad (16)$$

By solving the Poisson equation in polar coordinates, the electrostatic potential  $\psi_r$  can be obtained.

$$\begin{aligned} \psi(r) &= \psi_o \\ \psi(r) &= \psi_o - \frac{eN_D}{4\epsilon} \left( r^2 - (r_{phys} - d)^2 \right) + \frac{eN_D}{2\epsilon} (r_{phys} - d)^2 \left( \ln \left( \frac{r}{r_{phys} - d} \right) \right) \end{aligned} \quad \begin{aligned} 0 \leq r \leq r_{elec} \\ r_{elec} \leq r \leq r_{phys} \end{aligned} \quad (17)$$

where the  $\psi_0$  is the potential at  $r = 0$  and the value of the potential  $\psi_0$  can be obtained by setting equation (17) to zero and solving for  $\psi_0 = \psi(0)$ . Starting with neutrality condition the surface depletion width ( $d$ ) in a 1D structure can be derived as the following [55, 63]:

$$\begin{aligned} \pi(r_{phys}^2 - r_{elec}^2)\rho + 2\pi r_{phys} N_s &= 0 \\ r_{elec} &= \sqrt{r_{phys}^2 - \frac{2r_{phys} q^2 D_{it} \psi_0}{\rho(1 + \frac{r_{phys} q^2 D_{it}}{2\epsilon_s})}} \\ d &= r_{phys} - r_{elec} \end{aligned} \quad (18)$$

The critical radius which NWs with a smaller radius than that will be completely depleted can be obtained as given below [55, 63]

$$r_{cri} \approx \frac{2}{\rho} (q^2 D_{it} \psi_0) \quad (19)$$

In case of  $r_{phys} < r_{cri}$  the electrostatic potential  $\psi_r$  can be describe as

$$\psi(r) = \psi_s + \frac{\rho}{4\epsilon_s} (r_{phys}^2 - r^2) \quad (20)$$

Where, the surface potential can be described as the following.

$$\psi_s = \frac{r_{phys} \rho}{2q^2 D_{it}} \quad (21)$$

As it described in case of NWs with a radius smaller than critical radius the surface potential has a linear relationship with static charges (ionized impurities and induced piezoelectric charges). In the case of  $r_{\text{phys}} > r_{\text{cri}}$ , by considering the piezoelectric induced charge density, in terms of equivalent density, the effect of piezoelectric charges on the surface potential and surface depletion region of ZnO NWs have been investigated. The equivalent density of piezoelectric charges in a general term can be expressed as [55, 57];

$$N_{PE} = -\frac{1}{q} \frac{\partial}{\partial x_i} (e_{ijk} \cdot \frac{\partial u_j}{\partial x_k}) \quad (22)$$

where,  $u_i$  is the vector displacement of ions in the crystal structure of the piezoelectric material and  $q$  is the electron charge. As shown in section 3.2 an external applied force propagating with arbitrary angle ( $\eta$ ) in the XZ plane of a wurtzite crystal can result in a radial piezoelectric polarization in the piezoelectric material. Noting that the internal electric field in the surface depletion region of NWs has a radial direction, the radial piezoelectric polarization component ( $P_r$ ) may increase or decrease the internal electric field strength in the surface depletion region. The effect of radial piezoelectric polarization component in the surface depletion region of ZnO NWs can be modeled by considering an equivalent density of piezoelectric charges as following [55]:

$$\begin{aligned} N_{PE} = & -\frac{1}{q} \left\{ \left( e'_{x1} \cos^3 \Phi + e'_{x2} \cos \Phi \sin^2 \Phi + e'_{y6} \sin \Phi \sin 2\Phi \right) \frac{\partial^2 u_r}{\partial r^2} \right. \\ & + \left( e'_{x1} \cos \Phi \sin^2 \Phi + e'_{x2} \cos^3 \Phi - e'_{y6} \sin \Phi \sin 2\Phi \right) \\ & \times \left( -\frac{u_r}{r^2} + \frac{\partial u_r}{\partial r} \frac{1}{r} - \frac{1}{r^2} \frac{\partial u_r}{\partial \Phi} + \frac{1}{r} \frac{\partial^2 u_r}{\partial \Phi \partial r} \right) + e'_{x3} \cos \Phi \frac{\partial^2 u_z}{\partial z \partial r} + \left( e'_{y4} \sin \Phi \cos \Phi - e'_{x5} \cos \Phi \sin \Phi \right) \left( \frac{\partial^2 u_\Phi}{\partial z \partial r} - \frac{1}{r^2} \frac{\partial u_z}{\partial \Phi} + \frac{1}{r} \frac{\partial^2 u_z}{\partial \Phi \partial r} \right) \\ & + \left( e'_{y4} \sin^2 \Phi + e'_{x5} \cos^2 \Phi \right) \times \left( \frac{\partial^2 u_r}{\partial z \partial r} + \frac{\partial^2 u_z}{\partial r^2} \right) + \left( -e'_{x1} \cos \Phi \frac{\sin 2\Phi}{2} + e'_{x2} \cos \Phi \frac{\sin 2\Phi}{2} + e'_{y6} \sin \Phi \cos 2\Phi \right) \\ & \times \left( -\frac{1}{r^2} \frac{\partial u_r}{\partial \Phi} + \frac{1}{r} \frac{\partial^2 u_r}{\partial \Phi \partial r} + \frac{\partial^2 u_\Phi}{\partial r^2} + \frac{u_\Phi}{r^2} - \frac{\partial u_\Phi}{\partial r} \frac{1}{r} \right) \left. \right\} \end{aligned} \quad (23)$$

In the depletion region of the semiconductor where the density of the free carriers is negligible, the piezoelectric charges may be added to the ionized impurities (donor or acceptor) [55, 57]. In other words, in presence of piezoelectric charges the charge density in depletion region  $\rho(r)$  will be modified. Therefore charge density in the depleted region will be modified as following:

$$\rho(r) \approx q(N_D - N_A + N_{PE}) \quad (24)$$

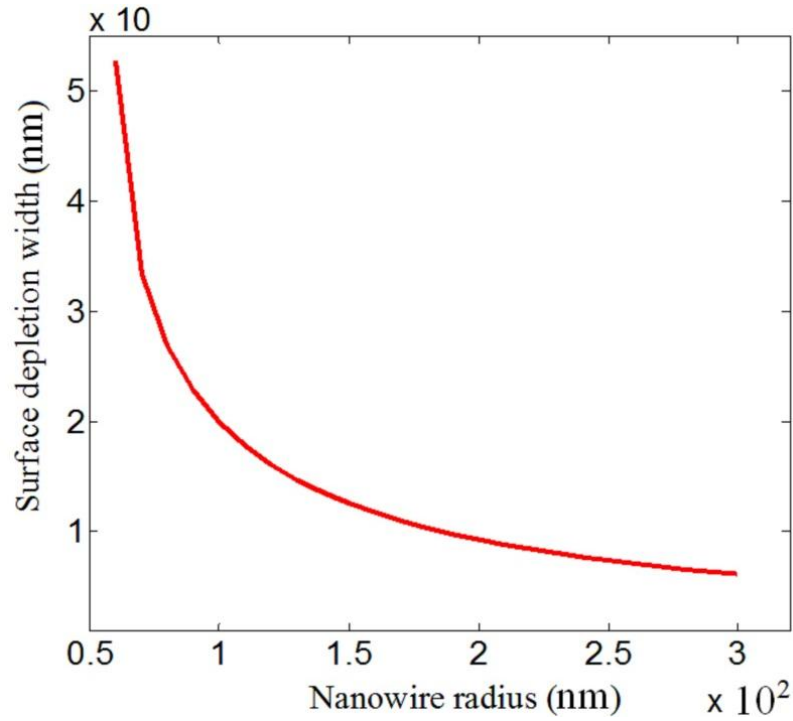
The sign of piezoelectric charge is a function of applied stress tensor and dependent on the direction of generated electric field may be considered as positive or negative piezoelectric charges. Using the equations derived in this section and substituting the values of the respective coefficients from table I the numerical simulation have been performed [55].

#### **4.4 Results and discussion**

Since the piezoelectric polarization will be cancelled in the non-depleted region of a ZnO NW, the nanowires with a larger surface depletion region will be affected more by the induced piezoelectric charges. The surface depletion thickness of ZnO NWs with the different radius is shown in figure 19. The NWs with smaller radius have a larger surface depletion width. In case of ZnO NWs, the critical radius at which the nanowires of smaller radius will be completely depleted is about 50 nm. Figure 20 presents the surface depletion perturbation caused by immobile piezoelectric charges for NWs with different radius and it is shown that the nanowires with the smaller radius are affected more by immobile piezoelectric charges [55].

**Table II:** CONSTANTS USED IN THE NUMERICAL ANALYSIS.

Material	$E_g$	$N_s$	$N_D$	$N_A$	$\epsilon_s$
ZnO	3.37eV [62]	$7 \times 10^{13} \text{cm}^{-2}$ [58]	$10^{18} \text{cm}^{-3}$ [54]	0	8.5 [54]

**Figure 19:** The surface depletion width of ZnO NWs with different radii.

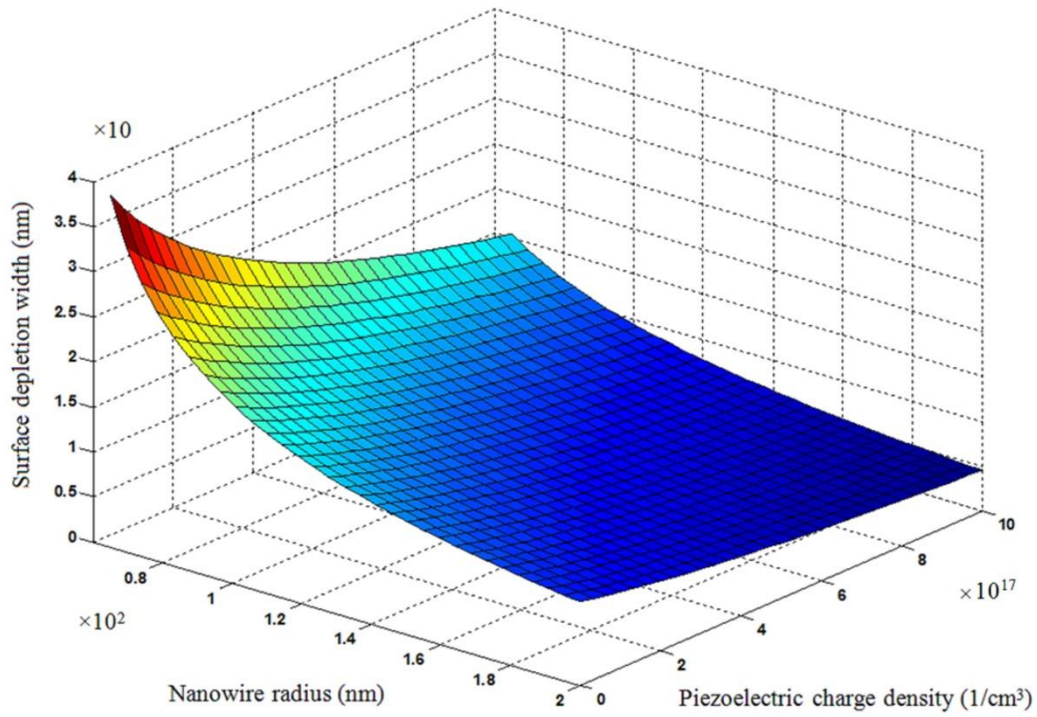


**Figure 20: The surface depletion width of ZnO NWs with different radii in the presence of piezoelectric charges.**

Figure 21 shows the electric potential distribution in a ZnO NW with a radius of 80 nm in the presence of different piezoelectric charge density in its depletion region. It is seen that besides the 10 nm depletion region modulation there is a surface potential change of around 250 mV [55].

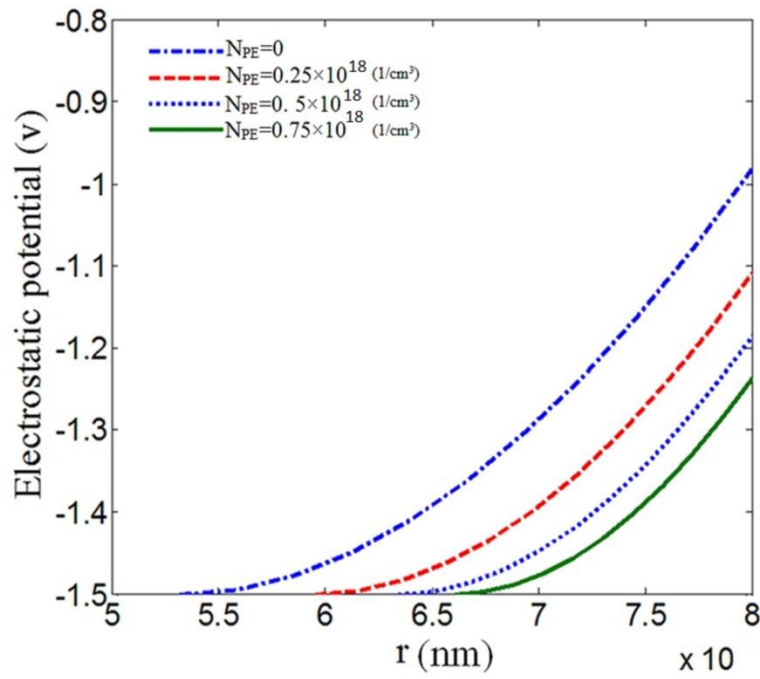


**Figure 21: The potential electric distribution in a ZnO NW with radius 80 nm in presence of different piezoelectric charge densities.**

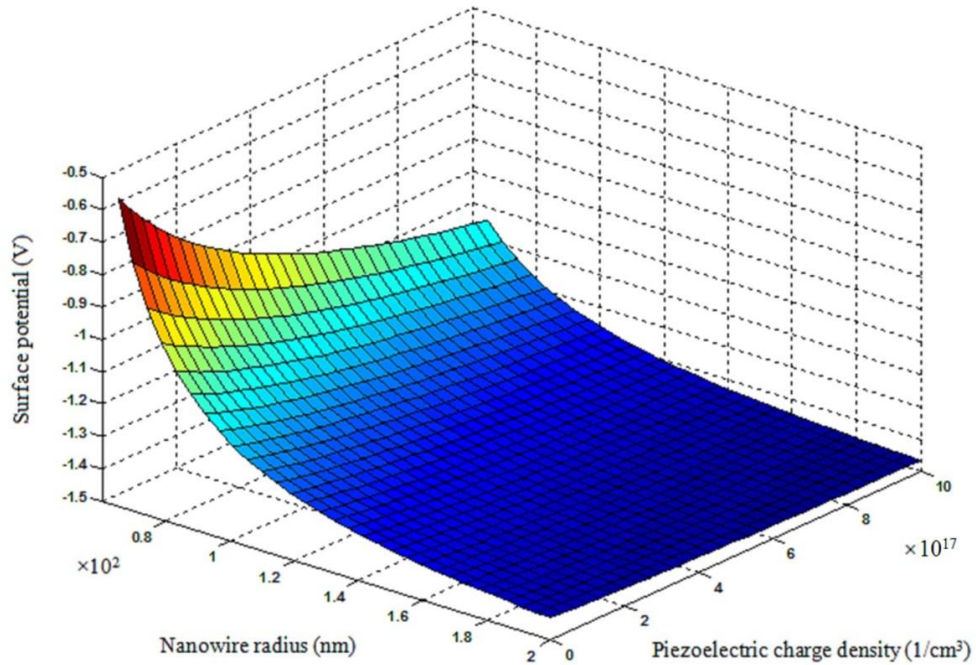


**Figure 22: The surface potential of a ZnO NWs with different radii as a function of piezoelectric charges.**



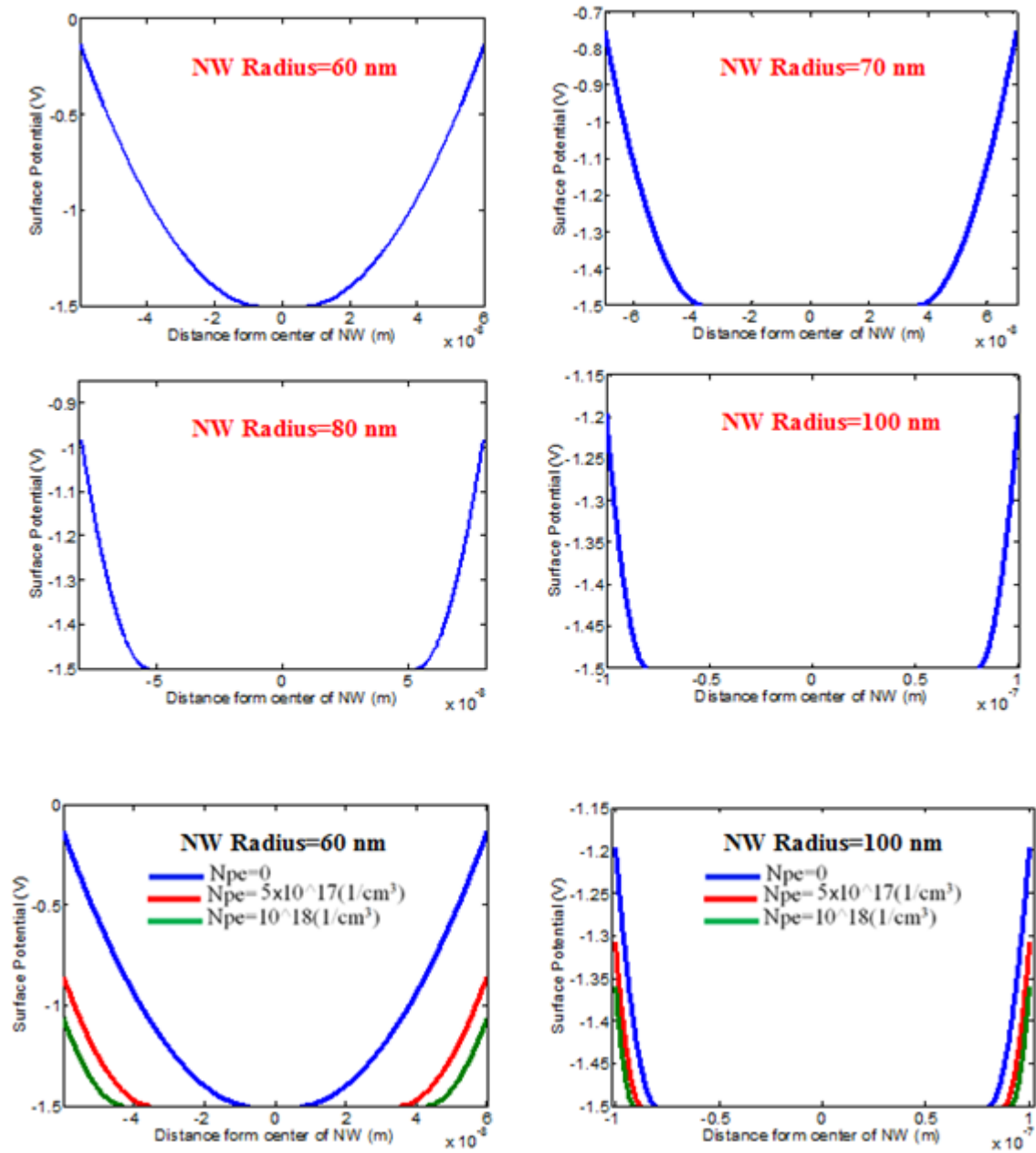


**Figure 23:** The surface depletion region of ZnO NWs with different radius and the surface potential of ZnO NWs with two different radiuses (60nm and 100nm) at presence of different piezoelectric charge densities.

The surface potential of ZnO NWs with different radii in presence of different piezoelectric charge has been illustrated in figure 22. As is shown, the surface potential of nanowires with the smaller radius are more affected by the induced piezoelectric charges. The surface potential of ZnO NWs with two different radii (60 nm and 100 nm) in the presence of different piezoelectric charge densities across the nanowire is shown in figure 23.

## **5. INVESTIGATION OF EFFECT OF APPLIED STRESS FREQUENCY ON THE ELECTRICAL RESPONSE OF PVDF-TrFE NANO-FIBERS**

Polyvinylidene fluoride (PVDF) is a piezoelectric polymer that has been the focus of much research in many piezoelectric applications due to its high piezoelectric coefficient. The electromechanical properties of PVDF can be defined by the constitutive equations. In this chapter, the effect of applied stress frequency on the electrical response of PVDF-TrFE has been investigated. We found that increasing the frequency of the applied stress results in increasing of pulse width of the electrical response. A model based on the mechanical creep and relaxation of PVDF has been proposed which agrees well with the observed experimental results.

### **5.1 Piezoelectricity in PVDF polymers**

The emergence of portable and light-weight mobile devices has led to a need for alternative power sources instead of conventional batteries. In many applications such as biomedical drug-delivery implants, implantable medical electronics devices and wireless micro-sensor remote locations batteries are not feasible. So harvesting energy from the environment is becoming essential for self-powered devices. One of the promising methods of energy harvesting is the use of piezoelectric materials to capitalize on the ambient vibrations [67-70]. The conversion of mechanical energy to electrical energy has been well demonstrated using piezoelectric cantilever-based MEMS devices [71]. However, the large unit size, large triggering force and specific high resonance frequency of the traditional cantilever based energy harvesters limit their applicability and adaptability in nanoscale device and systems. From this point of view, nano structure

materials such as nanowires and nanofibers have been the focus of much research as promising nanogenerators [72]. Among the piezoelectric materials PVDF and lead zirconate titanate (PZT) have been more extensively studied because of their high piezoelectric coefficients. Energy harvesters and generators made of PVDF or PZT can be fabricated by means of electrospinning processes such as conventional, modified or near-field electrospinning (NFES) [70]. Polymer based piezoelectric materials such as Polyvinylidene fluoride (PVDF-TrFE) gives us some advantages over the other piezoelectric materials. PVDF-TrFE is inexpensive, easy to process, light weight and more flexible compared to the other piezoelectric materials [73].

However the generated power by piezoelectric energy harvesters is too small to directly power an electronic device. Hence, much of the research into power harvesting has focused on methods of accumulating the generated energy until the charge stored is enough to power an electronic device. From this domain, characterization of generated pulses by piezoelectric energy harvesters is one of the key factors in designing nano-scale self-powered devices. In this study, the effect of applied stress frequency on the electrical response of randomly oriented PVDF-TrFE nanofibers has been investigated. A model based on the mechanical creep and relaxation of PVDF has been proposed which satisfies the observed experimental results. As described in chapter 3 the constitutive relations above equations imply that in the case of an ideal insulator such as PVDF-TrFE, in which the density of free carriers is negligible, the generation of the piezoelectric charge may be considered equivalent to the generation of an electrical field or a potential [74-76]. The piezoelectric properties of PVDF-TrFE come from the remnant polarization obtained by

orienting the crystalline phase in strong poling field. Piezoelectric behavior is seen when the material is below its curie temperature and the copolymer exhibits paraelectric behaviors above its curie temperature. The origin of piezoelectric behavior of PVDF-TrFE is the ferroelectric characteristics of the material, where the copolymer generates an electric field based on applied stress or change in shape. Since piezoelectric properties of this copolymer depend on the degree of crystallinity and thin PVDF-TrFE copolymers show higher phase separation under stronger electric fields, PVDF-TrFE is considered as one of the best candidates for energy harvesting applications [77].

## **5.2 Experimental**

The PVDF-TrFE nanofibres were grown by the electrospinning process. The basic experimental setup and the possible dipole orientation during the electrospinning process are shown in figure 24. The body of the polymer liquid droplet charges due to the application of the high electric field on the liquid droplet and the electrostatic repulsion counteracts the surface tension. As a result the droplet is stretched and due to molecular cohesion of the liquid, the stream does not break up. Under the condition that molecule cohesion is not tight enough, the droplets are electro-sprayed and a jet of charged liquid is formed. Due to the charge migration to the surface of the fiber the jet is elongated by a whipping process set up by the electrostatic repulsion initiated at the small bends in the fiber.

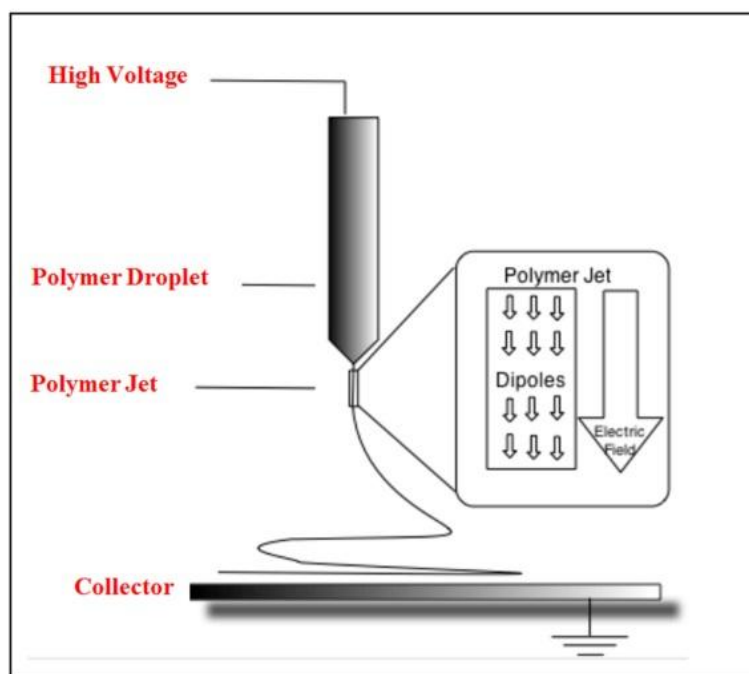


**Figure 24:** Schematic of the electrospinning setup and poling process.



**Figure 25:** The optical image of the as-electrospun nanofibers.

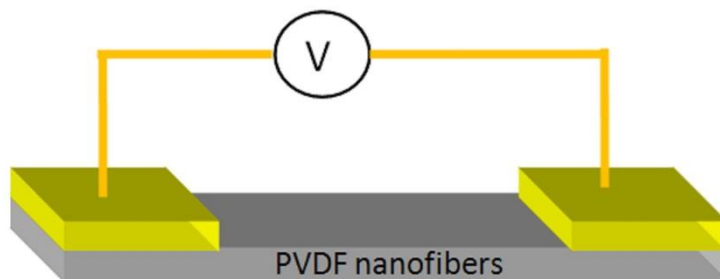


**Figure 26:** The schematic diagram of the energy harvester based on PVDF nanofibers.

This process is carried on until it is deposited on the grounded collector, which leads to the formation of uniform nanofibers. Prior to the electrospinning process a copolymer of PVDF-TrFE in the ratio of 70:30 was used. Then 1 g of PVDF-TrFE was mixed with 3 g of N-dimethylformamide (DMF) and 2 g of acetone and then the mixture was heated on a hotplate at 75 °C with vigorous stirring overnight until a clear solution resulted. During the electrospinning process the flow rate was kept equal to 0.25 ml/h under the application of electric field ~1-2 kV/cm. To produce the PVDF nanofibers, the ITO coated plastic was used as a conductive substrate which has enough flexibility for vibration purposes. An optical image of the as-electrospun nanofibers and the schematic diagram of fabricated device are shown in figure 25 and figure 26, separately.

### **5.3 Effect of vibration frequency on generated pulse width**

A typical electrical response of the PVDF-TrFE nanofibers is shown in figure 27 (a). As seen the typical amplitude of pulses are around 1 V with a duty cycle of about few ms. To study the effect of vibration frequency on the pulse width of electrical responses, the electrical response of PVDF-TrFE nanofibers at different frequencies are investigated.

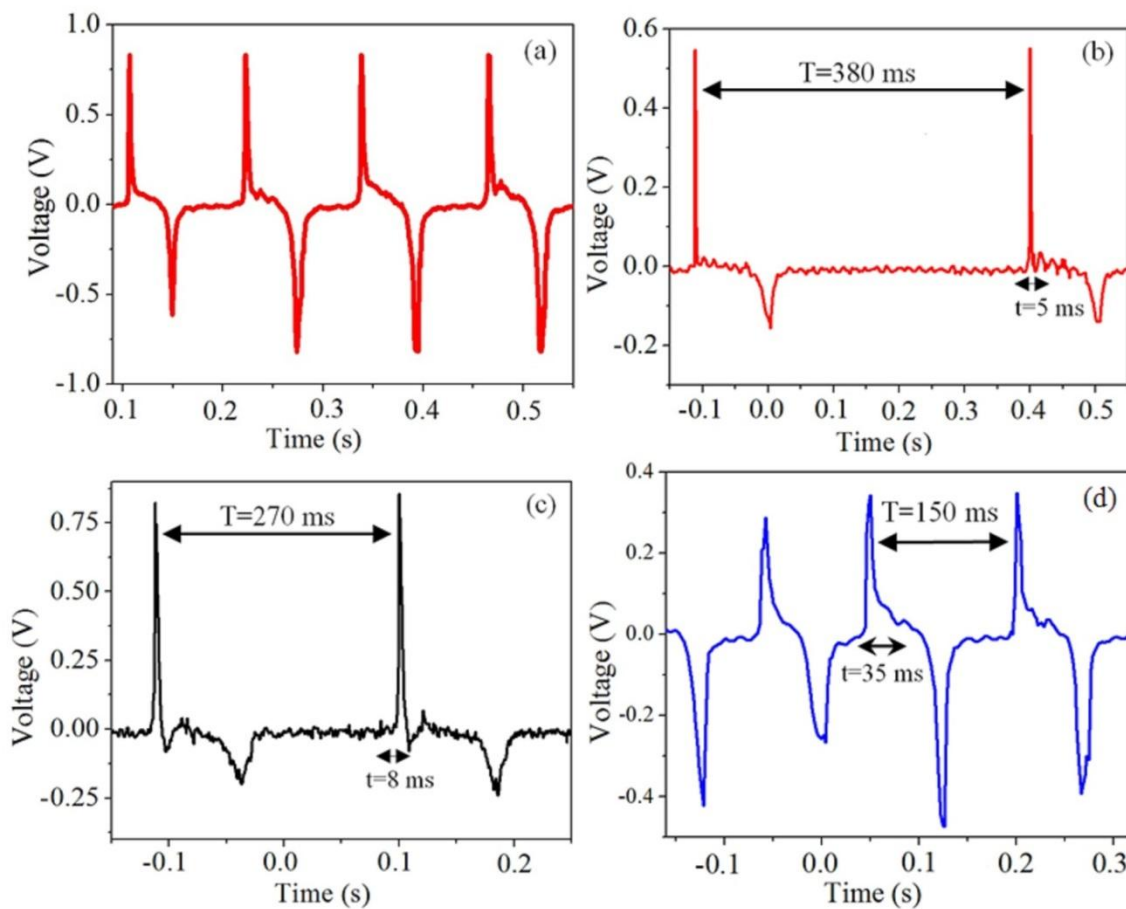


**Figure 27:** (a) A typical electrical response of PVDF nanofibers and electrical response of PVDF nanofibers at different vibration frequencies, (b) at frequency = 2.6Hz, (c) at frequency = 3.7Hz and (d) at frequency = 6.5Hz.

The electrical response shown in figure 27 demonstrates that by increasing the frequency, the pulse width of the electrical responses is increased and this increase is not a function of the amplitude of the electrical response. As shown increasing the vibration frequency from 2.7 Hz to 6.5 Hz is resulting in increasing of pulse width from 5 ms to 35 ms.



#### 5.4 Estimation of maximum output power

As discussed the generated power by piezoelectric energy harvesters is too small to directly power an electronic device. By using the fast Fourier transform (FFT) technique the maximum output power generated by PVDF nanofibers is estimated. By considering a single time period of the electrical response, the FFT data shown at figure 28 are obtained. Considering the main harmonic located at frequency 0.6 and ignoring other harmonics and by considering one external resistance load equal to the internal resistance of energy harvester, the power is calculated which is around 0.6 nW.

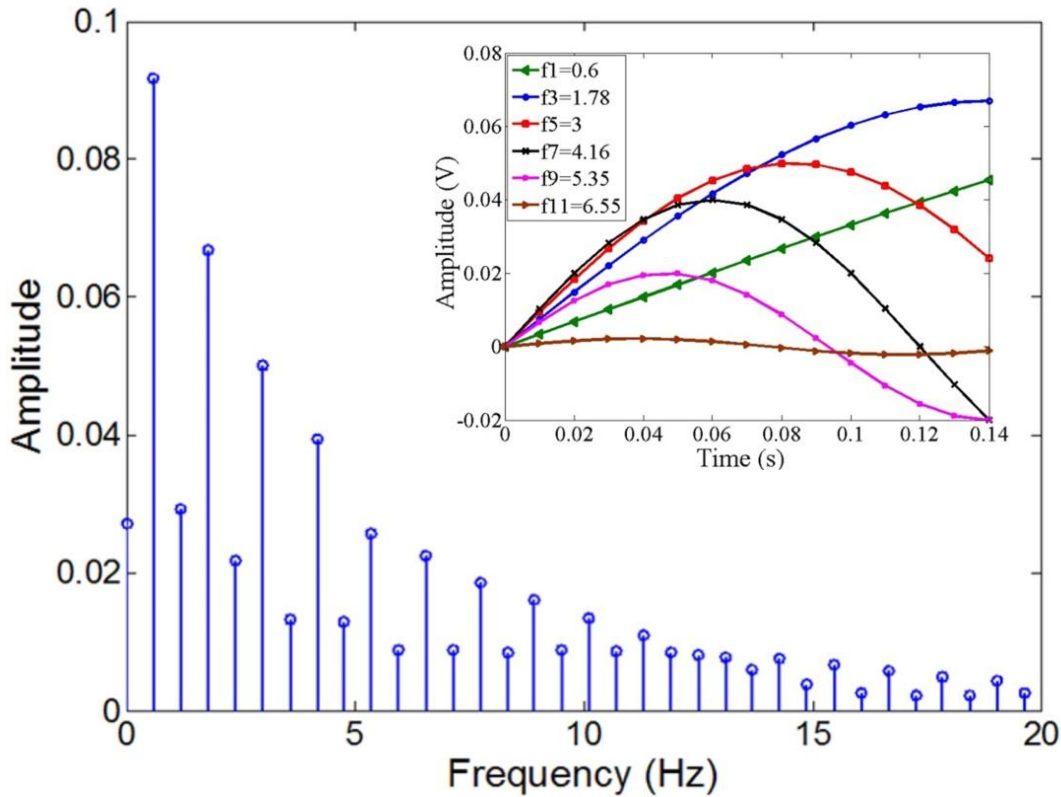


**Figure 28:** Fast Fourier Transform (FFT) for one cycle output voltage and the insert picture is corresponding sin waves of odd frequency.

### 5.5 Mechanical creep and relaxation of PVDF

In this section a model based on mechanical creep and relaxation of PVDF is proposed to explain the experimental results. Creep is a common phenomenon for engineering applications where products are subjected to an external stress and a simple way to obtain information concerning the viscoelastic properties of materials [78]. From a more practical point of view, the creep behavior of PVDF materials can be characterized by using the constitutive equations of linear viscoelasticity in the form [79]:

$$\varepsilon(t) = \sigma(0)c_n(t) + \int_0^t c_n(t-\tau) \frac{d\sigma}{d\tau} d\tau \quad (1)$$

where stress ( $\delta$ ) and strain ( $\varepsilon$ ) are functions of time, and  $C_n$  ( $n = 1,2$ ) represent the creep compliances in the respective material direction of PVDF. The direction 1 represents the direction aligned to the molecular chains ( $n = 1$ ) and in the direction 2 is normal to the orientation of the aligned molecular chains ( $n = 2$ ). The creep compliances  $C_n(t)$  of PVDF can be expressed analytically as shown below [79]:

$$c_n(t) = a_n + b_n(t\alpha_n), n = 1, 2 \quad (2)$$

Hence, the creep properties of PVDF can be defined in the form:

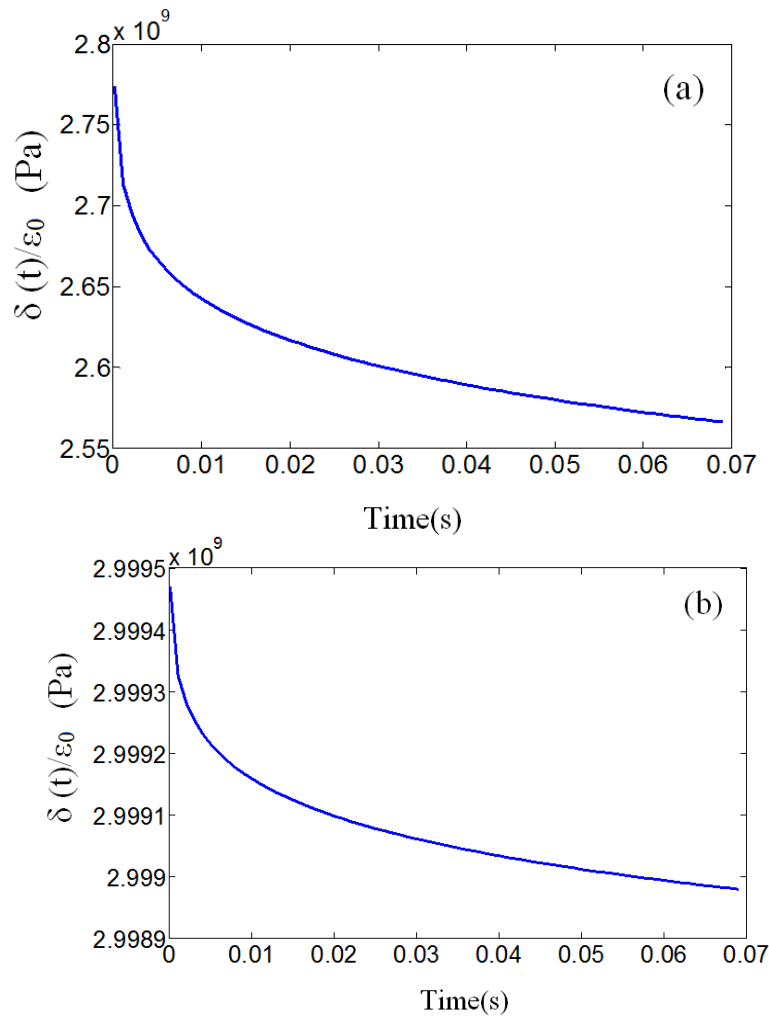


**Figure 29:** The mechanical relaxation function of PVDF in the directions of  $n = 1$ (a) and  $n = 2$  (b).

$$\varepsilon(t) = \alpha_n \sigma(t) + b_n c_n \int_0^t \left[ \sigma(\tau) / (t - \tau)^{1-\alpha_n} \right] d\tau, (n=1, 2) \quad (3)$$

The mechanical relaxation of PVDF in both material directions can be characterized by solving Eq. (4) in terms of  $\delta(t)$ . Therefore stress relaxation of the material for any given strain history can be represented as follows [13]:

$$\frac{\sigma(t)}{\varepsilon_0} = \frac{1}{a_n} \left[ 1 - \int_0^t \sum_{n=1}^{\infty} \frac{(b_n \alpha_n / a_n) \Gamma(\alpha_n) (t-\tau)^{\alpha_n}}{(t-\tau) \Gamma(n \alpha_n)} d\tau \right] \quad (5)$$

where  $\Gamma(\alpha_n)$  and  $\Gamma(n\alpha_n)$  are gamma functions. The mechanical relaxation function of PVDF in the directions of 1 and 2 are illustrated in figure 29. As shown in figure 6, the mechanical relaxation is a function of time. Considering a situation that piezoelectric material is subjected to a periodic external stress pulse, and noting that the material is not completely relaxed after each applied stress pulse, the material will be subjected to a value of stress equal to the summation of non-relaxed previous stress and new applied stress pulse. Hence, increasing the frequency of applied stress results in the increase of the pulse width of electrical response as observed.

## **6. LOW POWER INTERFACE CIRCUITS FOR PIEZOELECTRIC MICRO-SCALE ENERGY HARVESTING SYSTEMS**

Utilization of piezoelectric energy harvesters to power electronic devices has attracted significant attention recently. However, the power generated by a piezoelectric energy harvester is too small to power an electronic device directly. Hence, a low power efficient interface circuit between the energy harvester and a storage unit is essential in any piezoelectric energy harvesting system. In this chapter, a new interface circuit topology for piezoelectric energy harvesting applications is proposed and various design factors for circuit-level optimization are discussed. In the proposed interface circuit a peak detector circuit operating in the sub-threshold region with power dissipation around 160 nW together with a delay circuit form the control block, which is one of the more important units of the piezoelectric energy harvesting systems.

### **6.1 Introduction to low power interface circuits for energy harvesting applications**

Since the power generated by piezoelectric energy harvesters (PEH) is too small to directly power an electronic device. Therefore, much of the research into power harvesting has focused on methods of accumulating the generated energy until the charge stored is enough to power an electronic device. From this point of view, any PEH needs to be equipped with a very efficient interface circuit where the ultra-low power design characteristics of that circuit ensures maximum output power extracted from the piezoelectric devices. Full-bridge rectifiers and voltage doublers are one of the most commonly used rectifiers for converting the AC output of a PEH into a DC voltage. However, the voltage drop across the p-n junction rectifiers results in a low output power, which is the main disadvantage [80, 81]. Due to the low output voltage of PEH,

conventional approaches, where the incoming AC voltage is rectified with a diode and diode configured transistors, are not suitable. Although output power can be increased by increasing the damping force of the transducer, the incoming voltage still needs to surmount threshold minimum to extract energy. Hence an efficient low power interface circuit is a key component in micro-scale energy harvesting systems. Even though power converters have been extensively used in battery-powered embedded systems, the optimization objective in those systems is very different from micro-scale energy harvesting systems. In this study, we will discuss various design factors that help to optimize the circuit-level design of interface circuit for micro-scale energy harvesting systems. In addition to addressing circuit-level optimization for efficient power conversion, a new circuit topology will be proposed and considerations at the architecture level discussed.

## **6.2 Block component diagram of a micro-scale piezoelectric energy harvesting system**

The block diagram of a micro-scale energy harvesting system is shown in figure 30. The system comprises five main blocks: the piezoelectric energy harvester, the power converter, the control unit, the energy buffer, and the application unit. The piezoelectric energy harvester converts ambient mechanical energy into electrical power and the power converter extracts power from the PEH and transfers as much power as possible to the energy buffer or application unit.

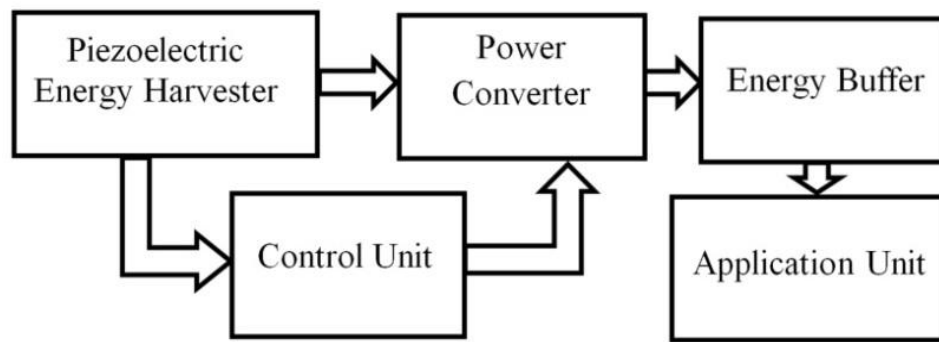


**Figure 30:** The block diagram of a micro-scale energy harvesting system.

The control unit plays a crucial role in reducing the system power loss and maximizing the overall system efficiency. The control block of an energy harvester system should be as simple as possible; otherwise the control circuit will consume a major part of the harvested energy.

### **6.2.1 Piezoelectric energy harvester**

In order to optimize the device structure, the relationship between the device parameters and device performance should be known. To this end an analytical model of the generator is important not only for estimating the amount of power possible from a given vibration source, but also for making explicit relationships that can give some indication for improvement of device performance [82]. Piezoelectric elements can be modeled by representing both the mechanical and electrical portions of the piezoelectric system as circuit elements, as shown in figure 31. The current ( $i$ ) represents the current generated as a result of the mechanical stress evaluated at zero electric field. Applying the zero electric field condition to constitutive equations and substituting strain for stress yields [82]:

$$D = d_{31} c_p S \quad (1)$$

where  $d_{31}$  is the piezoelectric coefficient,  $c_p$  is the elastic constant and  $S$  is the induced strain. However, depending on the crystal structure of the piezoelectric material, other piezoelectric coefficients may be important [83, 84]. Noting that electrical displacement is the charge density across a dielectric element, electrical displacement can be related to current for the bender device as given below [82]:

$$i = a w l_e d_{31} c_p \left( \frac{\partial S}{\partial t} \right) \quad (2)$$

where  $w$  is the width and  $l_e$  is the length of the piezoelectric element shown in figure 31. The impedance of a piezoelectric element having a rectangular shape can be given as follows [82, 85]:

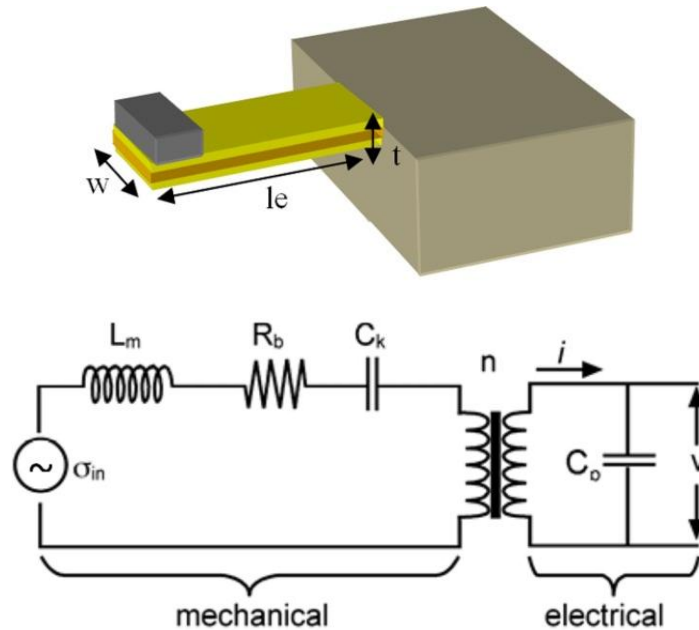


**Figure 31:** the schematic diagram of a cantilever based piezoelectric energy harvester and its equivalent circuit [82].



$$\begin{aligned}
Z_{in} &= \frac{1}{jC_0\omega} [1 - k_t^2 \frac{\tan(\alpha t)}{\alpha t}] \\
\alpha &= \frac{\omega}{v_s} \\
C_0 &= \frac{a^2 \epsilon w l_e}{2t}
\end{aligned} \tag{3}$$

where  $k_t$  is the electromechanical coupling factor,  $\alpha$  is the wave velocity in the Z direction,  $t$  is the thickness of the piezoelectric element,  $a$  is constant between 1 and 2 depending on the device configuration,  $\epsilon$  is the permittivity of the piezoelectric element,  $v_s$  the wave velocity in the propagation direction and  $\omega$  is the vibration frequency [82, 85]. Therefore the piezoelectric energy harvester can be represented as the circuit shown in figure 31 [82]. Since an ideal PEH has infinite input impedance, an ideal PEH can be achieved by minimizing the dimensions of the piezoelectric element. However, considering the relationship between the generated current and the device dimensions, minimizing the piezoelectric element will also result in a very low current as shown above. Hence, there is a trade-off between the generated current and input impedance of a PEH.

### **6.2.2 Power converter**

There are several methods to achieve AC-DC voltage conversion. Each of these methods has its specific benefits and disadvantages, such as voltage conversion ratio range, the maximal output power, power conversion efficiency, number of components, and power density [81, 86 and 87]. As discussed, due to the low output power of PEHs, conventional approaches, where the incoming AC voltage is rectified with a diode and diode configured transistors, are not suitable for piezoelectric energy harvesting systems.

Here, two major types of efficient power converters frequently used for self-powered energy-efficient devices are explored.

#### **6.2.2.1 Charge-pump AC-DC converters**

Unlike an inductor-based converter, a switched capacitor (SC) converter does not rely on magnetic energy storage, which makes it an ideal candidate for integrated implementations. However, SCs suffer from a finite number of conversion ratios [88] which limit their applications. One major type of conventional SC voltage converters is shown in figure 32. In this scheme, a non-overlap clock generator is employed to drive the switch matrix with a clock frequency generated by a control unit. During each half period the system waits until the PEH reaches its maximum voltage, then the switch  $S_1$  is closed to discharge the internal capacitor of the PEH into capacitors  $C_1$  and  $C_2$  and then the energy is transferred from  $C_1$  and  $C_2$  to  $C_L$  by closing the switch  $S_2$  while the switch  $S_1$  is open. The ideal condition for energy transfer is when the internal capacitor of the PEH completely discharges into  $C_1$  and  $C_2$  during each half cycle, otherwise the remaining charge will be dissipated during the next half period as shown in figure 33. The percentage of power dissipation can be controlled by changing the capacity of  $C_1$  and  $C_2$  as shown in figure 33.

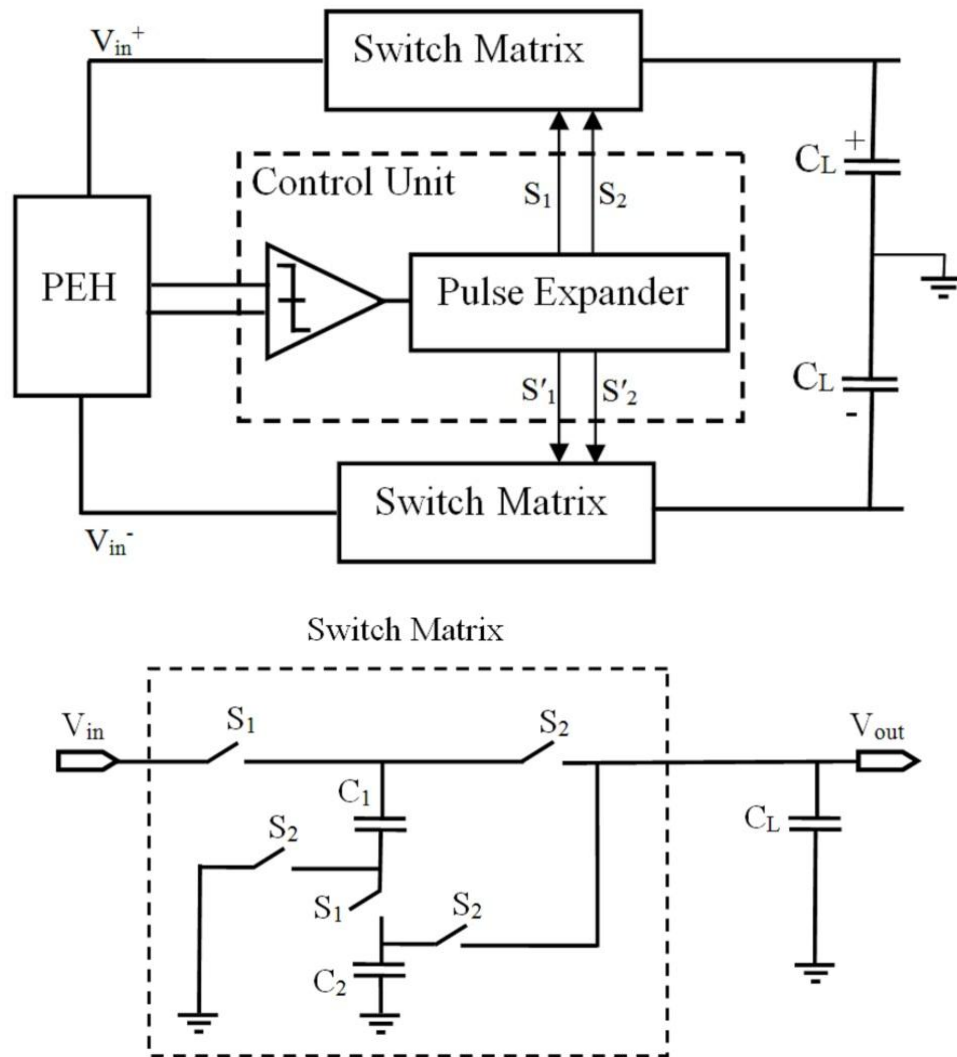


**Figure 32:** The schematic diagram of conventional SC voltage converter.

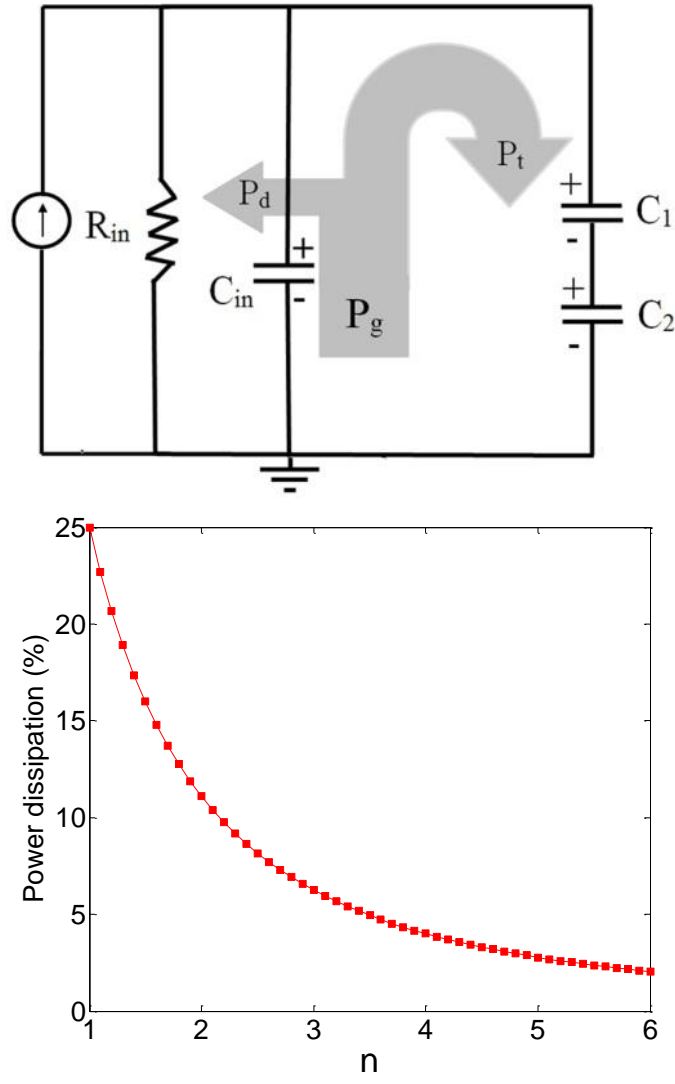


**Figure 33:** Power dissipation in PEH.

$$\frac{P_d}{P_g} = \left[ \frac{1}{(1+n)^2} \right] \times 100 \quad (4)$$

$$n = \frac{c_1 c_2}{c_{in} (c_1 + c_2)}$$

Considering the relationship between the output voltage and  $n$ , there is a trade-off between the power dissipation in the PEH and output voltage so that increasing  $n$  results in a lower output voltage. In the case of small-scale systems and micro-systems (e.g., MEMS devices), some considerations may occur with respect to the implementation of the control systems. In particular, the magnetic components, such as the inductor, may be seen as a limitation in terms of integration and miniaturization of the device. In this domain it seems that changing the inductor with a capacitor for better integration could be one ideal option. However, as discussed above the dielectric nature of piezoelectric elements make such an approach unsuitable for micro-scale energy harvesting systems [89].

#### **6.2.2.2 Boost converters**

Considering the dielectric nature of piezoelectric elements, boost converters seem to be the best candidate for the power converter unit in piezoelectric energy harvesting systems. Recently different circuit topologies using boost converters have been proposed [80, 90]. Here, a new circuit topology employing the boost converter scheme as power converter is proposed.

##### *A. Proposed Circuit Topologies*

The block diagram of the proposed interface circuit is shown in figure 34. As seen a zero crossing peak detector, together with a time delay block is used to control the transfer of energy across the vibration cycle from the energy harvester into the storage unit. The prototype of the proposed interface circuit, control signals and its theoretical currents are illustrated in figure 35. The energy flow in the proposed interface circuit is similar to the

mechanism described in [80] with a major difference in the control block and energy storage unit, which comes from the difference in the circuit topology. The proposed circuit topology employs a simple control unit which should be as simple as possible, otherwise a major part of the harvested energy will be dissipated in the control unit.

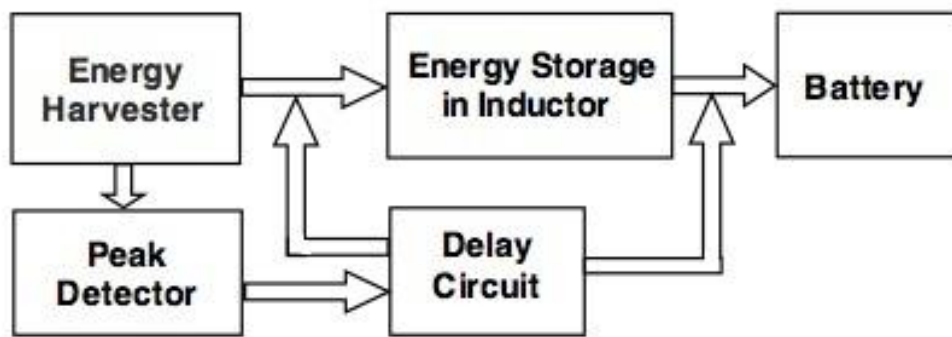


**Figure 34:** The block diagram of the proposed interface circuit.

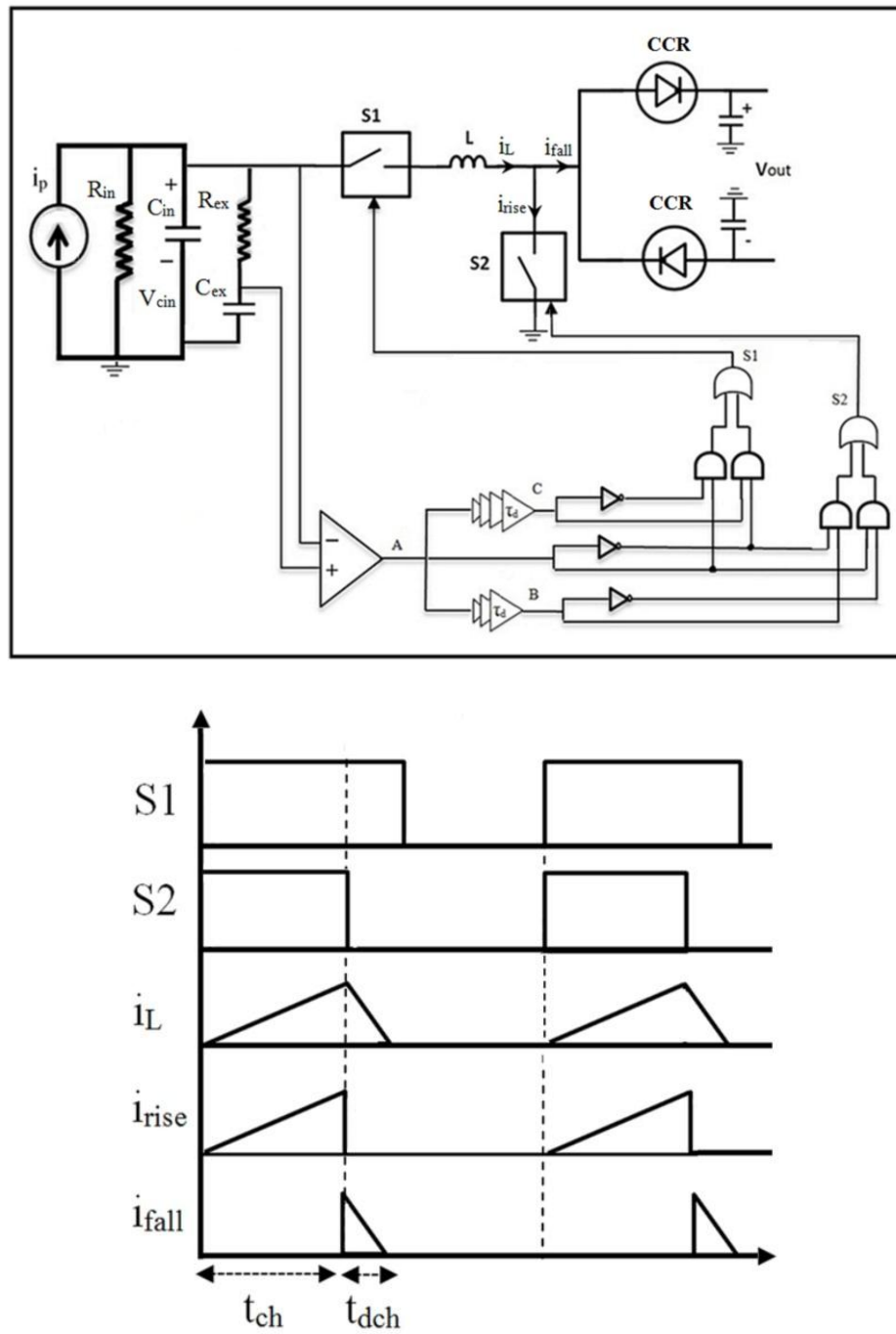


**Figure 35:** The prototype diagram of proposed interface circuit and control and timing signals generated by control block and the theoretical currents of proposed interface circuits.

### *B. Energy Flow*

During the vibration cycles the system waits until the  $V_{C_{in}}$  reaches its maximum value, when the output of peak detector circuits (A), together with delay versions of signal A (B and C) are used to generate the control signals  $S_1$  and  $S_2$ . As shown in figure 36, the proposed circuit topology needs the same switch states in positive and negative half-period contrary to the piezoelectric energy harvester-charger IC given in [80]. The switches  $S_1$  and  $S_2$  will be ON to energize the harvesting inductor from  $C_{in}$  in energizing time ( $t_{ch}$ ). Then when the current in the inductor peaks, the switch  $S_2$  is OFF and CMOS-Controlled Rectifiers (CCR) are turned ON to discharge L into the battery in time  $t = t_{dch}$ . The equivalent circuit of the proposed interface circuit at charging and discharging modes can be represented as shown in figure 36, where the switches are represented by a small resistance ( $R_s$ ) during operation.



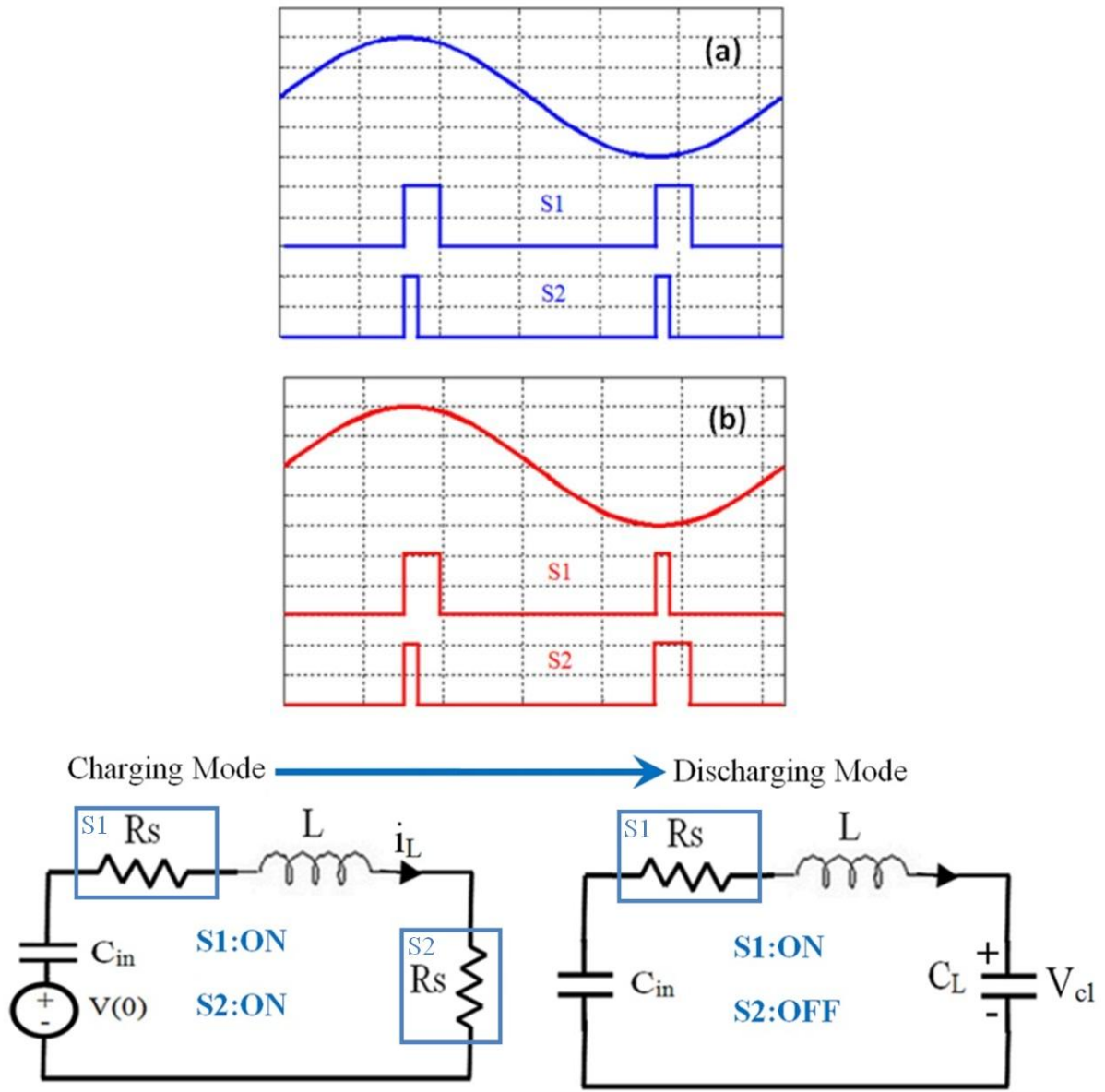


**Figure 36:** The switch states in positive and negative half-period (a) in the proposed circuit topology and (b) in the Piezoelectric Energy Harvester-Charger IC proposed in Ref. [80] and the equivalent circuits in charging and discharging modes of proposed circuit topology.

The current flowing through the inductor in charging mode can be expressed as seen below:

$$i_L(t) = I_0 e^{\left(\frac{-R}{L}t\right)} \sin(\omega_a t)$$

$$I_0 = \frac{V_c(0)}{L\omega_a} \quad (5)$$

$$\omega_a = \sqrt{\left(\frac{1}{C_{in}L} - \frac{R^2}{L^2}\right)}$$

And the output voltage ( $V_{cl}$ ) at the discharging mode can be given as follows:

$$V_{cl}(t) = V_0 e^{\left(\frac{-R}{2L}t\right)} \sin(\omega_b t) \quad (6)$$

$$V_0 = \frac{I_0}{C_L \omega_b}$$

$$C_e = \frac{C_l C_{in}}{C_l + C_{in}}$$

$$\omega_b = \sqrt{\left(\frac{1}{LC_e} - \frac{R^2}{4L^2}\right)}$$

Therefore, charging time ( $t_{ch}$ ) and discharging time ( $t=t_{dch}$ ) can be given as follows:

$$t_{ch} = \frac{T_a}{4} = \frac{\pi}{2\omega_a} \quad (7)$$

$$t_{dch} = \frac{T_b}{4} = \frac{\pi}{2\omega_b} \quad (8)$$

### 6.2.3 Control unit

#### A. Peak-Detector Circuit

In the proposed circuit topology, when  $V_{Cin}$  reaches its maximum value, switches  $S_1$  and  $S_2$  should be ON to start discharging  $C_{in}$  into  $L$ . In other words, the switches need to be turned ON when  $i_p$  crosses zero. The zero crossing point can be detected by the proposed

continuous time comparator shown in figure 37. The comparator is modeled based on the circuit described in [91] and in order to minimize the power consumption the circuit is designed to operate in sub-threshold region with power consumption around 160 nW. Since the input of the comparator is 90 degrees phase-shifted from  $V_{cin}$  [80], the zero crossing point is where  $C_{in}$  reaches its maximum voltage.

### *B. Delay Circuit*

To generate the control signals  $S_1$  and  $S_2$ , the delay versions of the peak detector circuit output are required, which can be generated by using the designed delay circuit shown in figure 8.

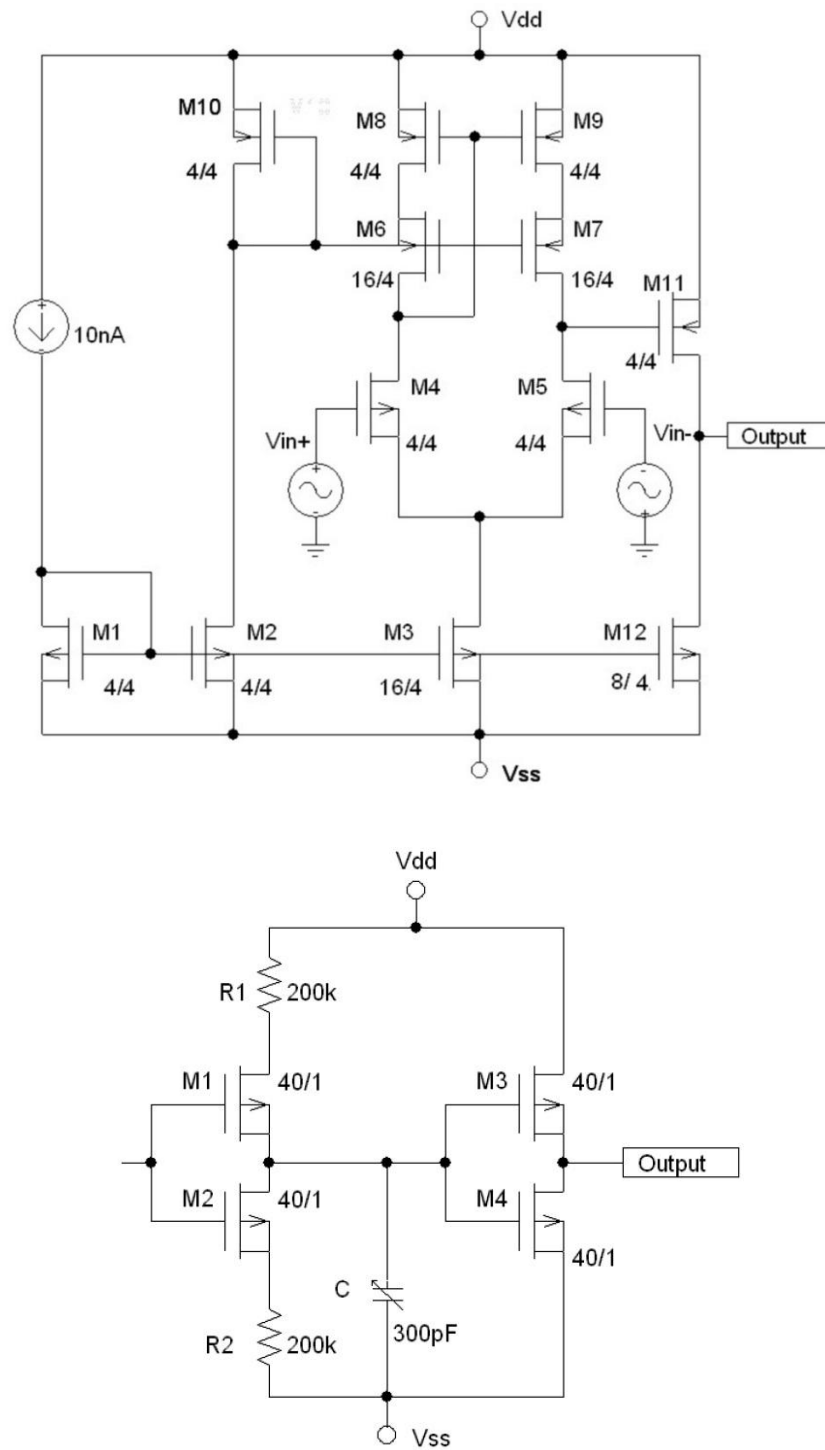


**Figure 37:** The transistor level schematic of the designed continuous time comparator circuit operating in sub-threshold region ( $v_{dd} = 1$  and  $v_{ss} = -1$ ) and the designed time delay circuit.

### *C. CMOS-Controlled Rectifiers (CCR)*

To reduce the diode voltage conduction loss in the interface circuits used in energy harvesting systems, the diodes can be replaced by active rectifiers. A schematic diagram of an active rectifier is presented in figure 38. As shown a power transistor (NMOS or PMOS) is used as a switch control of the conduction in the forward path. The rectifier conducts when the input to the rectifier is higher than the converter output. An ideal active rectifier must work similarly to an ideal diode, with almost perfect reverse current blocking and nearly zero dropped voltage in the forward direction. Hence the quick response and low energy dissipation are the main properties of an ideal active rectifier [90]. Different circuit topologies such as sub-threshold differential comparators [92], input power comparators [87] and CMOS-control rectifiers [90] have been proposed to operate as the controlled rectifier block in energy harvesting systems. However, due to the common-mode-voltage in common-source-differential input and a strong trade-off between response time and quiescent-current consumption [80, 90], the classical design with common-source-differential input and current-tail bias are not suitable for use as active rectifiers. To overcome the common problem with the classical design the CMOS-control rectifier introduced by Man and Mok [90] can be used as an active rectifier.

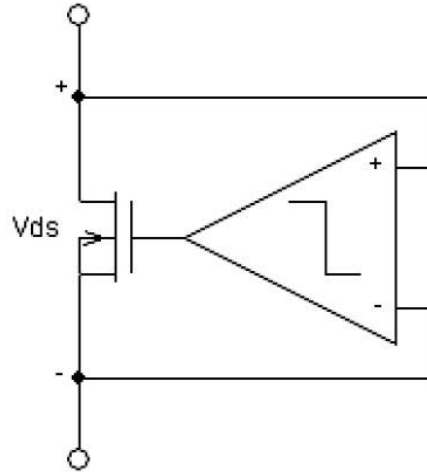


**Figure 38:** The schematic diagram of an active rectifier.

### 6.3 Power transfer loss model

The main contributors to the power loss inside the interface circuitry are conduction power loss, switching power loss and biasing power loss [93].

#### A. Conduction Power Loss

Every MOS transistor has non-negligible resistance when it is switched on, which can be modeled by the following:

$$R_{on} = \frac{1}{\mu c_{ox} \left(\frac{W}{L}\right) (V_{GS} - V_{TH} - \frac{1}{2} V_{DS})} \quad (9)$$

where  $V_{TH}$  is the threshold voltage, and  $V_{GS}$  and  $V_{DS}$  are the gate and drain voltage, respectively. And  $W$  is the power transistor size. Then the conduction power loss of a power transistor can be estimated as:

$$P_{on} = \frac{I_{on}^2}{\mu c_{ox} \left(\frac{W}{L}\right) (V_{GS} - V_{TH} - \frac{1}{2} V_{DS})} \quad (10)$$

### B. Switching Power Loss

Switching power loss is a result of charging and discharging of the gate capacitance of power transistors and their driving buffers during switching. Assume that the gate capacitance per unit area is  $C_{OX}$ . The switching power loss of a power transistor can be expressed as [93]:

$$P_{SWT} = c_{ox}(WL)V_{dd}^2 f_{CLK} \quad (11)$$

where in the proposed circuit topology the clock frequency ( $f_{CLK}$ ) is two times the vibration frequency.

### C. Biasing Power Loss

Biasing power loss is due to static biasing, which is required to power the analog amplifier and current mirror branches and is given by:

$$P_{BIAS} = I_{BIAS} V_{dd} \quad (12)$$

Considering all of the above components of power loss, the total power transfer loss in an interface circuitry can be given as:

$$P_{LOSS} = P_{CON} + P_{SWT} + P_{BIAS} \quad (13)$$

The various power loss components are calculated and shown in figure 39.

## 6.4 Optimal power transistor size

As discussed above,  $P_{LOSS}$  is a function of the power transistor size and the switching frequency. Estimating the switching frequency, which is determined by the resonant frequency of PEHs, the optimal power transistor size can

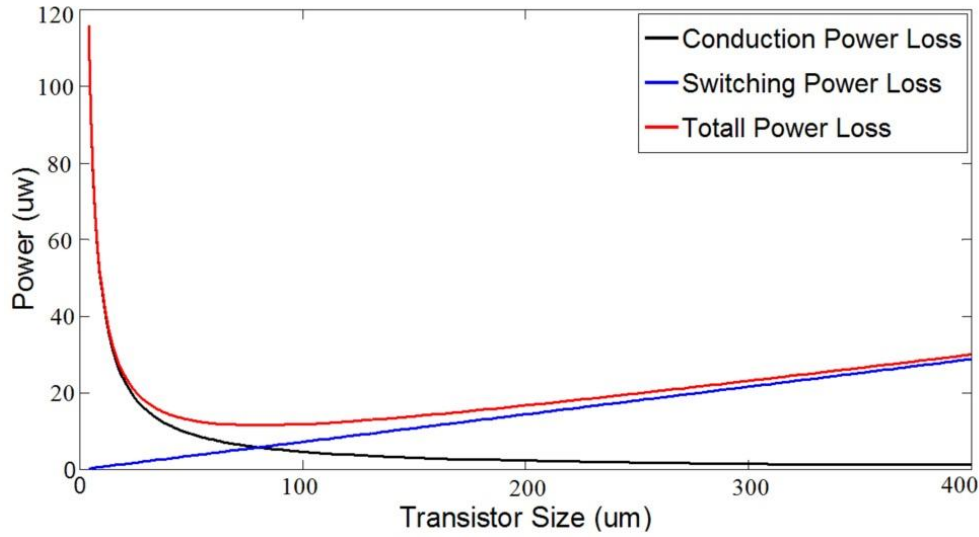


**Figure 39:** Power loss of a power transistor versus the power transistor size.

be determined by solving the derivative of equation 13 with respect to  $W$ . The total power transfer loss using the optimal power transistor size is expressed as [93]:

$$P_{LOSS - OptSize} = P_{BIAS} + I_{ON} V_{dd} L \sqrt{\frac{10 f_{CLK}}{\mu(V_{GS} - V_{TH} - \frac{1}{2} V_{DS})}} \quad (14)$$

## 6.5 Component value considerations

Since the optimal energy transfer in the proposed interface circuit is strongly dependent on the value of harvesting inductor ( $L$ ), determination of the inductor value is one of the most critical design parts. Considering the maximum ratio of storage energy in the inductor to the power dissipated by switches in conduction mode and considering the charging and discharging times, the minimum and maximum limits of the inductor value can be determined as shown:



$$\frac{E_L}{E_R} = \frac{\frac{1}{2}LI_0^2}{RI_{rms}^2} \approx L \quad (15)$$

$$t_{dch} = \frac{\pi}{2\omega_b} = \frac{\pi}{2\sqrt{(\frac{1}{C_e L} - \frac{R_s^2}{4L^2})}} \quad (16)$$

Therefore:

$$L > \frac{C_e R_s^2}{4} \quad (17)$$

and since the  $t_{dch} < t_{ch}$  the following condition also should be met:

$$t_{dch} \leq \frac{\pi}{2\omega} \quad (18)$$

where  $\omega$  is the vibration frequency. Considering the above condition a maximum and minimum for the inductor value can be given as:

$$L_{min} = \frac{1}{2\omega^2} \left[ \frac{1}{C_e} - \sqrt{\frac{1}{C_e^2} - R_s^2 \omega^2} \right] \quad (19)$$

$$L_{max} = \frac{1}{2\omega^2} \left[ \frac{1}{C_e} + \sqrt{\frac{1}{C_e^2} - R_s^2 \omega^2} \right] \quad (20)$$

There is also another important consideration in terms of integration and miniaturization of the device, which limits the maximum inductor value and it may also determine the maximum inductor value.

## 7. CONCLUSIONS AND FUTURE WORK

### 7.1 Conclusions

We grew ultra-long high-quality ZnO NWs using the VLS method. Although VLS is a standard technique, this was the first time it was grown at UIC. First the VLS setup was built and NWs were grown on the n-type, 100 plane silicon wafer at a temperature around 900-910 °C. For the first time, we demonstrated that decorating the ZnO NWs with sputtered metallic nano-particles in presence of high energy Ar atoms result in a strong enhancement of NBE peak on the PL spectra of ZnO NWs. Our experimental results demonstrated that this enhancement is much stronger and more stable than other introduced methods such as polymer coating and hydrogen treatment techniques.

The first part of this work focused on the investigation of surface defect passivation in ZnO NWs and in particular the effect of sputtered metallic nanoparticles on the PL spectra of as grown ZnO NWs has been studied. The room temperature and low temperature PL spectra of as grown ZnO NWs and those coated with metallic NPs by different deposition methods were investigated. It was shown that the PL spectra of ZnO NWs coated with sputtered metallic NPs demonstrate a strong enhancement of NBE peak and a relative reduction of visible peak. Effects of type of contact formed between metallic NPs and ZnO NWs and unintentional hydrogen incorporation have been investigated. The observed experimental results revealed that decorating the ZnO NWs with metal NPs in presence of high energy Ar atoms can decrease the non-radiative relaxation pathways and lead to a strong enhancement of NBE emission and a relative reduction of visible peak. A model was proposed which strongly satisfied the observed experimental results.

In addition to the PL study of as grown and decorated ZnO NWs, in the first part of this study, we have also investigated the PL intensities of the CdSe/ZnS core-shell QDs and as grown ZnO NWs deposited on GaAs, silicon, glass and ITO-coated glass and simulated our experimental data. For the first time we found that PL intensity of both QDs and NWs is dependent on the substrate and scattering field from the substrates can modify the PL intensity of deposited materials on the substrate. Our analysis indicates that the PL intensity variation on different substrates is not a function of material type and the band-gap discontinuities formed between the substrates and the deposited materials. The simulation demonstrates that the substrates having the maximum scattered field has the strongest PL intensity.

In the second part of this study, the piezoelectric materials and piezoelectric energy harvesting devices were the focus of our study. First, ZnO NWs, as the first demonstrated piezoelectric nano-generators, were studied and for the first time we have developed a model which conciliates some strongly divergent opinions behind operation of the semiconductor piezoelectric nano-generators. So far, no model has been developed which includes the presence of free carriers exist in the crystal structure of piezoelectric semiconductor materials used for piezoelectric energy harvesting.

The proposed model strongly satisfies the reported experimental results while the effect of free carriers in the crystal structure of piezoelectric material was also considered. In this treatment, the piezoelectric semiconductor was modeled with two separate regions: non-depleted region and depleted region. By solving the Poisson equation in the depleted region, the electrostatic potential and depletion region width obtained. A numerical

analysis was performed by considering the piezoelectric induced charge density, in terms of equivalent density of charges. The numerical analyses show that the immobile piezoelectric charges cause a change on the surface depletion thickness and the electric potential distribution in the surface depletion region of nanowire. The changes are more obvious in case of nanowires with smaller radii.

We have also investigated another type of piezoelectric materials which have negligible free carriers in its crystal structure investigated. In this domain, first the growth of electrospun nano-fibers of PVDF-TrFE has been explained and then the effect of applied stress frequency on the electrical response of piezoelectric nano-fibers has been investigated. The maximum power can be extracted from PVDF nano-fibers was calculated. It was shown that increasing the vibration frequency from 2.7 Hz to 6.5 Hz resulted in the increase of the pulse width from 5 ms to 35 ms. Considering the mechanical creep and relaxation of PVDF a model was proposed which satisfied the observed experimental results. Since the piezoelectric energy harvester devices have a low output power the low power interface circuits between the energy harvester and storage unit is a key component of any self-powered device. From this domain, an efficient low power interface circuit suitable for piezoelectric micro-scale energy harvesting systems was proposed and various design challenges, tradeoffs and considerations from circuit, architecture and system perspectives for an optimal energy transfer and storage have been discussed. It was shown that the switched capacitor converters are not suitable for piezoelectric energy harvesting systems, whereas using a boost converter as the power converter can enhance the net energy gain. Moreover, the effect of different component

values on the performance of the system has been investigated and the optimal component values have been determined.

## **7.2 Future works**

Since ZnO NWs have a weak NBE emission the enhancement of NBE is a key factor in the development of novel optoelectronic devices such as nano-lasers where a strong enhancement in the UV region of ZnO NWs will result in a device with a lower lasing threshold power. Hence, investigation of the electrical properties of decorated ZnO NWs with metallic nano-particles is suggested as future work of this study. Future work in doing pump probe optical experiments would allow further investigations into the decay mechanisms of the carriers and provide further answers to the questions towards developing ZnO NW lasers.

In investigating of the effect of different substrates on the PL intensity of deposited materials the drop-casting method was used to deposit the materials (NWs and QDs) on the different substrates. Due to the influence of aggregation on the PL spectra, which is strongly depending on the size of particles, future work can include an investigation of the effect of different deposition methods such as sputtering and molecular beam epitaxy (MBE) on the PL spectra of deposited materials.

In our proposed model, which explains the operation of nano-scale piezoelectric energy harvesters, ZnO NWs were treated as perfect crystal structures with a constant density of free carriers. Further investigation will be appropriate to add the effect of native defects and non-uniform free carrier density in the proposed model.

The utilization of the ZnO NWs as nano-generators requires metal contacts for extracting the generated voltage and it should be done through a sophisticated fabrication process. Hence, investigation of the P-N heterostructures based on a polymer such as P3HT and ZnO NWs can be one alternative approach. These heterostructure devices also have this advantage to be made on the flexible substrates. Therefore the complexity of bending the ZnO NWs will also reduced.

## CITED LITERATURE

1. H. J. Fan, P. Werner and M. Zacharias: Semiconductor Nanowires, From Self-Organization to Patterned Growth. *J. Small.* 2, No. 6, 700 – 717: 2006.
2. S. A. Fortuna and X. Li: Metal-catalyzed semiconductor nanowires: a review on the control of growth directions. *Semicond. Sci. Technol.* 25 024005: 2010.
3. J. Shi and X. Wang: Functional semiconductor nanowires via vapor deposition. *J. Vac. Sci. Technol. B* 29, 060801: 2011.
4. Z. L. Wang: Zinc oxide nanostructures: growth, properties and applications. *J. Phys: Condens. Matter* 16, R829–R858: 2004.
5. O. Ulusoy: ZnO Devices and Applications: A Review of Current Status and Future Prospects. *Proceedings of the IEEE* (Volume:98, Issue: 7 ), pp. 1255 – 1268: 2010.
6. Chu S, Wang G and Zhou W: Electrically pumped waveguide lasing from ZnO Nanowires. *Nature Nanotechnology* 6, 506: 2011.
7. C. Y. Chen, M. W. Chen, J. J. Ke, C. A. Lin, J. R. D. Retamal and J. H. He: Surface effects on optical and electrical properties of ZnO nanostructures. *Pure Appl. Chem.*, Vol. 82, No. 11, pp. 2055-2073: 2010.
8. <http://en.wikipedia.org/wiki/Piezoelectricity>
9. Z. L. Wang and J. Song: Piezoelectric Nanogenerators Based on Zinc Oxide Nanowire Arrays. *Vol 312 SCIENCE*, pp. 242-246: 2006.
10. A. P. Abiyasa, S. F. Yu, S. P. Lau, Eunice S. P. Leong, and H. Y. Yang: Enhancement of ultraviolet lasing from Ag-coated highly disordered ZnO films by surface-plasmon resonance. *Appl. Phys. Lett.* Vol. 90, pp.231106: 2007.
11. H. Zhu, C.X. Shan, B.H Li, Z. Z. Zhang, D.Z. Shen and K.L. Choy: Low-threshold electrically pumped ultraviolet laser diode. *J. Mater. Chem.* Vol.21, pp. 2848-2851: 2011.
12. T. Chen, G. Z. Xing, H.Y. Chen and T. Wu: Tailoring the photoluminescence of ZnO nanowires using Au nanoparticles. *IOP J. Nanotechnology.* Vol.19, pp. 435711-435716: 2008.
13. K. W. Liu, R. Chen, G. Z. Xing, T. Wu, and H. D. Sun: Photoluminescence characteristics of high quality ZnO nanowires and its enhancement by polymer covering. *Appl. Phys. Lett.* Vol.96, pp.023111: 2010.

### CITED LITERATURE (CONTINUED)

14. J. P. Richters, T. Voss, L. Wischmeier, I. Ruckmann, and J. Gutowski: Influence of polymer coating on the low-temperature photoluminescence properties of ZnO nanowires. *Appl. Phys. Lett.* VOL. 92, pp. 011103: 2008.
15. Y. Li, R. Uchino, T. Tokizono, A. Paulsen, M. Zhong, M. Shuzo, I. Yamada, and J. Delaunay: Effect of hydrogen plasma treatment on the luminescence and photoconductive properties of ZnO nanowires. *Mater. Res. Soc. Symp. Proc.* Vol.1206: 2010.
16. Y. J. Fang, J. Sha, Z. L. Wang, Y. T. Wan, W. W. Xia, and Y. W. Wang: Behind the change of the photoluminescence property of metal-coated ZnO nanowire arrays. *Appl. Phys. Lett.* Vol.98, pp.033103: 2011.
17. Wei Tang, Dongliang Huang, Lili Wu, Chaozhong Zhao, Lingling Xu, Hong Gao, Xitian Zhang and Weibo Wan.: Surface plasmon enhanced ultraviolet emission and observation of random lasing from self-assembly Zn/ZnO composite Nanowires. *CrystEngComm*, Vol.13: pp.2336: 2011.
18. A. Dev, J. P. Richters, J. Sartor, H. Kalt, J. Gutowski, and T. Voss: Enhancement of the near-band-edge photoluminescence of ZnO nanowires: Important role of hydrogen incorporation versus plasmon Resonances. *Appl. Phys. Lett.* Vol. 98, pp.131111: 2011.
19. P. Yang: The chemistry and physics of semiconductor nanowires. *MRS Bulletin*, Vol. 30: pp.85-91, 2005.
20. A. Kar: Defect Passivation in Nanowires and Demonstration of Nanowire Devices for Use in Sensing Applications”, PhD Thesis, Dep. Electrical and Computer Engineering, University of Illinois at Chicago, Chicago IL, 2012.
21. L. Wischmeier, T. Voss, I. Ruckmann and J. Gutowski: Correlations between surface-excitonic emission bands in ZnO nanowires. *IOP J. Nanotechnology*, Vol. 19, pp. 135705 (5pp): 2008.
22. C. Bekeny, T. Voss, B. Hilker, and J. Gutowski: Influence of ZnO seed crystals and annealing on the optical quality of low-temperature grown ZnO nanorods. *Appl. Phys. Lett* Vol.102, pp.044908: 2007.
23. H.C. Hsu, C.S. Cheng, C.C. Chang, S. Yang, C.S. Chang and W.F. Hsieh: Orientation-enhanced growth and optical properties of ZnO nanowires grown on porous silicon substrates. *IOP J. Nanotechnology*, Vol. 16, pp. 297–301: 2005.



### CITED LITERATURE (CONTINUED)

24. Z.M. Liao, H.Z. Zhang, Y.B. Zhou, J. Xu, J.M. Zhang, D.P. Yu: Surface effects on photoluminescence of single ZnO nanowires. *Science direct, J. Physics Letters A*, Vol. 372, pp. 4505-4509: 2008.
25. J. Richters, A. Dev, S. Müller, R. Niepelt, C. Borschel, C. Ronning, and T. Voss: Influence of metallic coatings on the photoluminescence properties of ZnO nanowires. *Phys. Status Solidi RRL* 3, No. 5, pp. 166-168: 2009.
26. M. Li, G. Xing, L. Foong Nien Ah Qune, G. Xing, T. Wu, C. Hon Alfred Huan, X. Zhang and T. C. Sum: Tailoring the charge carrier dynamic in ZnO nanowires: the role of surface hole/electron traps. *Phys. Chem. Chem. Phys.*, Vol. 14, pp.3075-3082: 2012.
27. W. Z. Liu, H. Y. Xu, J. G. Ma, C. Y. Liu, Y. X. Liu, and Y. C. Liu: Effect of oxygen-related surface adsorption on the efficiency and stability of ZnO nanorod array ultraviolet light-emitting diodes. *Appl. Phys. Lett.*, Vol. 100, pp. 203101: 2012.
28. C. Soci, A. Zhang, B. Xiang, S. A. Dayeh, D. P. R. Aplin, J. Park, X. Y. Bao, Y. H. Lo and D. Wang: ZnO Nanowire UV Photodetectors with High Internal Gain. *Nano Lett.*, Vol. 7: 2007.
29. Y. Li, F. D. Valle, M. Simonnet, I. Yamada, and J. J. Delaunay: Competitive surface effects of oxygen and water on UV photoresponse of ZnO nanowires. *Appl. Phys. Lett.*, Vol. 94, pp. 023110: 2009.
30. B. Ha, H. Ham and C. J. Lee: Photoluminescence of ZnO nanowires dependent on O<sub>2</sub> and Ar annealing. *Since Direct J. Physics and Chemistry of Solids*, Vol. 69, pp. 2453–2456: 2008.
31. J. H. He, C. S. Lao, L. J. Chen, D. Davidovic, and Z. L. Wang: Large-Scale Ni-Doped ZnO Nanowire Arrays and Electrical and Optical Properties. *J. AM. Chem. Soc.*, Vol. 127, pp.16376-16377: 2005.
32. X.Liu, X. Wu, H. Cao, and R. P. H. Chang: Growth mechanism and properties of ZnO nanorod synthesized by plasma-enhanced chemical vapor deposition. *J. Appl. Phys.*, Vol. 95, pp.3141-3147: 2004.
33. Y. J. Fang, J. Sha, Z. L. Wang, Y. T. Wan, W. W. Xia, and Y. W. Wang: Behind the change of the photoluminescence property of metal-coated ZnO nanowire arrays. *J. Appl. Phys. Lett.* Vol. 98, pp. 033103: 2011.

### CITED LITERATURE (CONTINUED)

34. D.J. Milliron, I.G. Hill, C. Shen, A. Kahn, J. Schwartz: Surface oxidation activates indium tin oxide for hole injection. *J. Appl. Phys. Lett.* Vol. 87, 572: 2000.
35. R. L. Hoffman, B. J. Norris and J. F. Wager: ZnO-based transparent thin-film transistors. *J. Appl. Phys. Lett.* Vol. 82, 723: 2003.
36. B.J. Norris, J. Anderson, J. F. Wager and D. A. Keszler, *J. Phys.D: Spin-coated zinc oxide transparent transistors.* *J. Appl. Phys.* Vol. 36, 105: 2003.
37. A. Khandelwal, Master of Science Thesis, University of Notre Dame, Indiana: 2005.
38. M. Molnar, Y. Fu1, P. Friberg, Y. Chen: Optical characterization of colloidal CdSe quantum dots in endothelial progenitor cells. *J. Nanobiotechnology* 8: 2010.
39. X. Lu1t, S. R. Huang, M. Diaz, R. L. Opila and A. Barnett, Proceeding of the PVSC 35th IEEE conference, Hawaii, USA, Jun 20-25: 2010.
40. T. B. Jones, M. Hochberg, and A. Scherer, *IEEE journal in Quantum Electronics* 14, 1335: 2008.
41. H. J. Xiang, J. Yang, J. G. Hou, and Q. Zhu: Piezoelectricity in ZnO nanowires: A first-principles study. *J. Appl. Phys Let*, 89, 223111: 2006.
42. K. Smaali, A. El Hdiy, M. Molinari, and M. Troyon: Band-Gap Determination of the Native Oxide Capping Quantum Dots by Use of Different Kinds of Conductive AFM Probes: Example of InAs/GaAs Quantum Dots. *J. IEEE Transaction on Electron devices*, 57, 14155: 2010.
43. J. Robertson: High dielectric constant oxides. *J. Appl. Phys.* 28, 265: 2004.
44. Z. L. Wang and J. Song: Piezoelectric Nanogenerators Based on Zinc Oxide Nanowire Arrays. *J. Science* 312, 242: 2006.
45. U. S. Inan, A. S. Inan, *Electromagnetic waves* (Prentice Hall, New Jersey, pp.173-180: 2000.
46. C Adrianni,S Chang: Metal-Coated Zinc Oxide Nanocavities. *IEEE Journal of quantum electronics* 47, 245: 2011.
47. M. Quinten and J. Stier: Absorption of scattered light in colloidal systems of aggregated particles. *Colloid Polym Sci.* 273, 233: 1995.

### CITED LITERATURE (CONTINUED)

48. Chu S, Wang G and Zhou W: Electrically pumped waveguide lasing from ZnO Nanowires. *Nature Nanotechnology* 6 506: 2011.
49. Zhu G, Yang R, Wang S and Wang Z L: Flexible High-Output Nanogenerator Based on Lateral ZnO Nanowire Array. *Nano Lett.* 10 3151: 2010.
50. Yeh P, Li Z and Wang Z: Schottky-Gated Probe-Free ZnO Nanowire Biosensor *Adv. Mater.* 21 4975: 2009.
51. Hickernell F S: the Piezoelectric Semiconductor and Acoustoelectronic Device Development in the Sixties. *IEEE transactions on ultrasonics, ferroelectrics, and frequency control* 52 737-745: 2005.
52. Wang Z L and Song J: Piezoelectric Nanogenerators Based on Zinc Oxide Nanowire Arrays. *Science* 312 242: 2006.
53. Beach R A and McGill T C: Piezoelectric fields in nitride devices *J. Vac. Sci. Technol. B* 17(4) 1753-1756: 1999.
54. Alexe M, Senz S, Schubert M A, Hesse D and Gosele U: Energy Harvesting Using Nanowires. *Adv. Mater.* 20 4021–4026: 2008.
55. M. Puraahmad, M. Strosio and Mitra Dutta, “A theoretical study on the effect of piezoelectric charges on the surface potential and surface depletion region of ZnO nanowires”, *IOP Semiconductor and Since Technology*, 28 015019: 2013.
56. Sen B, Strosio M and Dutta M: Piezoelectricity in wurtzite polar semiconductor nanowires. A theoretical study *J. Applied physics* 110 024506: 2011.
57. Withers R S: Electron Devices on piezoelectric semiconductors. A device model *IEEE transaction on sonic and ultrasonics* 31 117-123: 1984.
58. Liao Z M, Lv Z K, Zhou Y B, Xu J, Zhang J M and Yu D P: The effect of adsorbates on the space-charge-limited current in single ZnO nanowires. *IOP J. Nanotechnology* 19 335204: 2008.
59. Araneo R , Lovat G , Burghignoli P and Falconi C: piezo-semiconductive quasi-1D nanodevices with or without anti-symmetry. *J. Adv. Mater.* 24 4719–4724: 2012.
60. Romano G, Mantini G, Carlo A D, D’Amico A, Falconi C and Wang Z L: Piezoelectric potential in vertically aligned nanowires for high output nanogenerators *IOP J. Nanotechnology* 22 465401: 2011.

### CITED LITERATURE (CONTINUED)

61. Sen B, Stroscio M and Dutta M: Piezoelectricity in zincblende polar semiconductor nanowires: A theoretical study J. Applied physics 111 054514: 2012.
62. Liao Z M, Zhang H Z, Zhou Y B, Xu J, Zhang J M and Yu D P: Surface effects on photoluminescence of single ZnO nanowires J. Physics Letters A 372 4505–4509: 2008.
63. V. Schmidt, S. Senz and U. Gosele: Influence of the Si/SiO<sub>2</sub> interface on the charge carrier density of Si nanowires Appl. Phys. A 86 187: 2007.
64. Munakata C, Nishimatsu S: Analysis of ac surface photovoltages in a depletion oxidized p-type silicon wafer Jpn. J. Appl. Phys. 25 807: 1986.
65. Sze S M: Physics of Semiconductor Devices (Wiley, New York): 1981.
67. Z. L. Wang: Energy Harvesting for Self-Powered Nanosystems. J. Nano Research, Vol. 1, pp. 1- 8: 2008.
68. S. Saadon, O. Sidek, “Ambient Vibration-based MEMS Piezoelectric Energy Harvester for Green Energy Source,” IEEE Conference proceeding ICMSAO: 2011.
69. Sumon Dey, Mohsen Puraahmad, Suman Sinha-Ray, Alexander L. Yarin, Mitra Dutta, “Investigation of PVDF-TrFE Nanofibers for Energy Harvesting”, Proceeding of 2012 IEEE conference on nanotechnology material and devices conference (NMDC): 2012.
70. J. Chang, M. Dommer, C. Chang, L. Lin, “Piezoelectric nanofibers for energy scavenging applications,” J. Science Direct Nano Energy, vol. 1, pp. 356–371: 2012.
71. E. E. Aktakka, R. L. Peterson, K. Najafi: ‘A Self-Supplied Inertial Piezoelectric Energy Harvester with Power-Management IC’, IEEE proceeding of ISSCC, pp. 120-121: 2011.
72. G. Zhu, R. Yang, S. Wang, and Z. Lin Wang, “Flexible High-Output Nanogenerator Based on Lateral ZnO Nanowire Array”, J. Nano Lett. Vol. 10, pp. 3151–3155: 2010,
73. D. Vatansever, R.L. Hadimani, T. Shah and E. Siores “Investigation of Energy Harvesting from Renewable Sources with PVDF and PZT” J. Smart Materials and Structures, vol. 20, pp. 055019: 2011.
74. Mohsen Puraahmad, Michael A Stroscio and Mitra Dutta, “A theoretical study on the effect of piezoelectric charges on the surface potential and surface depletion region of ZnO nanowires”, IOP Semicond. Sci. Technol. Vol. 28, no. 1, pp. 015019 (6pp): 2013.

### CITED LITERATURE (CONTINUED)

75. Sen B, Strosio M and Dutta M “Piezoelectricity in wurtzite polar semiconductor nanowires: a theoretical study”, J. Appl. Phys. Vol. 110, pp. 024506: 2011.
76. Mohsen Purahmad, Michael A. Strosio, and Mitra Dutta, “A Numerical Analysis on the Effect of Piezoelectric Charges on the Surface Depletion Layer of ZnO Nanowires”, 15th International workshop on computational electronics (IWCE): 2012.
77. K. E. Hamia, A. Ribbea, S. Isodab, K. Matsushigea, “Structural analysis of the P (VDF/TrFE) copolymer film”. Since direct J. Chemical Engineering Science, vol. 58, pp. 397-400: 2003.
78. J.F. Mano, V. Sencadas, A. Mello Costa, S. Lanceros-Mendez, “Dynamic mechanical analysis and creep behaviour of PVDF films”, Elsevier Materials Science and Engineering A, vol. 370, pp.336–340: 2004.
79. Aleksandra M. Vinogradov, V. Hugo Schmidt, George F. Tuthill, Gary W. Bohannon, “Damping and electromechanical energy losses in the piezoelectric polymer PVDF”, Elsevier Mechanics of Materials, vol. 36, pp.1007–1016: 2004.
80. D. Kwon and G. A. Rincon-Mora: ‘A 2-um BiCMOS rectifier free AC–DC piezoelectric energy harvester-charger IC’ IEEE Trans. On Biomedical circuits and systems, 4, (6), pp. 400-409: 2010.
81. Y. K. Ramadass and A. P. Chandrakasan, “efficient piezoelectric energy harvesting interface circuit using a bias-flip rectifier and shared inductor”, IEEE solid state circuit, 45, (1), pp. 189-204: 2010.
82. S. Roundy and P. KWright: ‘A piezoelectric vibration based generator for wireless electronics’, Smart Mater. Struct, 13, pp.1131–1142: 2004.
83. B. Sen, M. Strosio, and M. Dutta, “Piezoelectricity in wurtzite polar semiconductor nanowires: A theoretical study”, J. Appl. Phys.,(110), pp. 024506 : 2011.
84. B. Sen, M. Strosio, and M. Dutta, “Piezoelectricity in zincblende polar semiconductor nanowires: A theoretical study”, J. Appl. Phys.(111), pp. 054514: 2012.
85. M. Brissaud: ‘Three-Dimensional Modeling of Piezoelectric Materials’, IEEE Transactions on Ultrasonics, Ferroelectrics and Frequency Control, 57, (9), pp. 2051-2065: 2010.

### CITED LITERATURE (CONTINUED)

86. K. Eguchi, T. Inoue, H. Zhu, and F. Ueno: 'A Charge-Pump Type AC-DC Converter for Remote Power Feeding to a RFID Tag', *Ecti transaction on electrical emg., electronics, and communications*, 5, (2), pp. 37-42: 2007.
87. Y. Rao and D. P. Arnold: 'an input-powered active AC/DC converter with zero standby power for energy harvesting applications', *proceeding of IEEE Energy Conversion Congress and Exposition (ECCE)*, Sep. pp. 4441- 4446: 2010.
88. M. D. Seeman: 'A Design Methodology for Switched-Capacitor DC-DC Converters', PhD Thesis, Electrical Engineering and Computer Sciences University of California at Berkeley: 2009.
89. D. Guyomar and M. Lallart: 'Recent Progress in Piezoelectric Conversion and Energy Harvesting Using Nonlinear Electronic Interfaces and Issues in Small Scale Implementation', *Micromachines*, 2, pp.274-294: 2011.
90. T. Y. Man and P. K. T. Mok: 'A 0.9-V Input Discontinuous-Conduction-Mode Boost Converter with CMOS-Control Rectifier," *IEEE J. Solid-State Circuits*, 43, (9), pp.2036-2046: 2008.
91. T. Le, J. Han, A. von Jouanne, K. Mayaram, and T. Fiez: 'Piezoelectric micro-power generation interface circuits', *IEEE J. Solid-State Circuits*, 41, (6), pp. 1411–1420: 2006.
92. A. Rahimi, O. Zorlu, A. Muhtraoglu and H. Kulah: 'fully self-powered electromagnetic energy harvesting system with highly efficient dual rail output', *IEEE Sensor Journal*, 12, (6), pp. 2287-2298: 2012.
93. C. Lu, S. P. Park, V. Raghunathan and K. Roy: 'Analysis and Design of Ultra Low Power Thermoelectric Energy Harvesting Systems', *proceeding ISLPED'10*, pp. 183-188: 2010.

## VITA

NAME	MOHSEN PURAHMAD
EDUCATION	PhD, University of Illinois at Chicago, 2013  MSc, K. N. Toosi University of Technology, Tehran, 2009  BSc, K. N. Toosi University of Technology, Tehran, 2006  Research Assistant in Electrical and Computer Engineering Department, 2009-2013
EXPERIENCE	Teaching Assistant in Electrical and Computer Engineering Department, 2009-2013
PUBLICATIONS	M. Puraahmad, M. A. Stroschio, and M. Dutta, “A theoretical study on the effect of piezoelectric charges on the surface potential and surface depletion region of ZnO nanowires”, Semiconductor Science and Technology IOP science vol. 28, 015019 (6pp), Dec. 2012.  S. Rahbarpour, M. Puraahmad, “Silver-rutile Schottky diode fabricated on oxidised titanium foil”, IOP Conference Series: Materials Science and Engineering, Vol. 17, 012016 (6pp), 2011.  M. Puraahmad, M. A. Stroschio, and M. Dutta, “Modeling the effect of nanowire size on the piezoelectric Nanogenerators output”, Accepted in 16th International Workshop on Computational Electronics (IWCE), Japan, July 2013.  Sumon Dey, Mohsen Puraahmad, Suman Sinha-Ray, Alexander L. Yarin, Mitra Dutta, “ Investigation of PVDF-TrFE Nanofibers for Energy Harvesting”, Conference Proc. IEEE Nanotechnology Material and Devices Conference (IEEE NMDC), 2012.  Mohsen Puraahmad, Michael A. Stroschio and Mitra Dutta, “A Numerical Analysis on the Effect of Piezoelectric Charges on the Surface Depletion Layer of ZnO Nanowires”, Conference Proc. 15th International Workshop on Computational Electronics (IWCE), 2012.

### VITA (CONTINUED)

S. Farid, M. Purahmad, M. A. Strosio and M. Dutta “Computational analysis of the emission of ZnO nanowires and coreshell CdSe/ZnS quantum dots deposited on different substrates”, Conference Proc. 15th International Workshop on Computational Electronics (IWCE), 2012.

Mohsen Purahmad, Michael A. Strosio, Fellow, Mitra Dutta, “Photoluminescence Characterization of ZnO Nanowires Decorated with Metallic Nanoparticles”, Conference Proc. IEEE Nanotechnology Material and Devices Conference (IEEE NMDC), 2012.

K. G. Punchihewa, E. Zaker, R. Kuljic, A. Rangaraj, M. Liu, M. Purahmad, H. Saboonchi, et al. “Improvement of the Sensitivity and Operating Range of MEMS-based Resistive-type Vacuum Gauges”, Conference Proc. Vacuum Nanoelectronics Conference (IVNC), 24th International, 2011.

M. Purahmad and I. R. Gatabi, “Design of an Organic Pixel Addressing Circuit for Active-Matrix OLED Displays”, Conference Proc. ASME MicroNano 2008 Conference, Kowloon, Hong Kong. 2008.

F. Hossein-Babaei, M. Purahmad, “wide dynamic range hydrogen sensing using silver-rutile Schottky diode”, Conference Proc. ICST2008, 2008.

M. Purahmad, H. Busta and et al., “A MEMS-based resistive vacuum gauge with voltage readout”, Accepted in Vacuum Nanoelectronics Conference (IVNC), 26th International, 2013.